Experimental and Computational Investigation of a Dual-Throat Fluidic Thrust-Vectoring Nozzle

by

Naveen Penmetsa

B.S., University of Colorado at Boulder, 2012

A thesis submitted to the

Faculty of the Graduate School of the

University of Colorado in partial fulfillment

of the requirements for the degree of

Master of Science

Department of Aerospace Engineering Sciences

2016

This thesis entitled:
Experimental and Computational Investigation of a Dual-Throat Fluidic Thrust-Vectoring Nozzle
written by Naveen Penmetsa
has been approved for the Department of Aerospace Engineering Sciences

_____

Prof. Ryan Starkey

_____

Prof. John Farnsworth

Date _____

The final copy of this thesis has been examined by the signatories, and we find that both the content and the form meet acceptable presentation standards of scholarly work in the above mentioned discipline.

Penmetsa, Naveen (M.S., Aerospace Engineering)

Experimental and Computational Investigation of a Dual-Throat Fluidic Thrust-Vectoring Nozzle

Thesis directed by Prof. Ryan Starkey

The dual-throat fluidic thrust-vectoring nozzle concept is of particular interest because of its ability to provide large vector angles with minimal losses in thrust. This work investigates the performance of a dual-throat fluidic thrust vectoring nozzle over a range of three secondary injection geometries: two (V1, V2) spanwise oriented rectangular slots of different thicknesses and (V3) a single spanwise oriented array of circular holes. Baseline testing at a nozzle pressure ratio (NPR) of 2 showed that the presence of the injection geometry alone had a noticeable impact in vectoring the primary flow. Specifically, the smaller slot, larger slot, and hole geometries deflected the primary flow by $\delta_a \approx 2^\circ$, 0.5°, and -4°, respectively. When secondary injection was introduced the smaller slot displayed better vector performance across the entire range of secondary injection mass flow rates as compared to the larger slot configuration. The circular hole geometry was less effective at low secondary injection flow rates, but came close to surpassing the performance of both slot geometries at 5% secondary injection. Increasing the NPR to 4 for all three cases greatly reduced the influence of the secondary injection geometry on the baseline nozzle performance. Specifically, the smaller slot geometry displayed a drop in thrust vectoring angle from $\delta_a = 12^\circ$ to 8° when NPR was increased from 2 to 4. Finally, using the experimental and computational data collected during this study, a method was developed to predict vector angle from the wall static-pressure distributions internal to the nozzle. This was accomplished through integrating the pressure profiles, applying a correction factor derived from computational results, and calculating the total thrust based upon the core mass flow rate and exit pressure. The predicted thrust-vector angle matched the angles measured from the schlieren photographs to within measurement uncertainty across the range of injection mass flow rates tested.

Contents

Chapter

Tables

Table

Figures

Figure

Chapter 1

Introduction

In traditional and modern rocket systems, thrust vectoring is used as a primary method for stability and control in flight. Even for atmospherically bound vehicles, thrust vectoring is an effective way of reducing the profile of aerodynamic control surfaces and increasing the maneuverability of the vehicle. The latter is the motivation for the use of mechanical thrust vectoring in the Lockheed Martin F/A-22. This system leverages the thrust generated by the main turbofan engines and mechanically vectors the direction of the exhaust flow. For a two-engine case such as the F/A-22, the mechanical thrust vectoring can supplement the forces generated by the ailerons and elevators to improve pitch and roll rates.

Though this method of thrust vectoring is able to provide large forces normal to the direction of flight, it has a number of disadvantages. Most prominent is the weight of the nozzle system. In order to rapidly actuate a nozzle, hydraulic actuation is often necessary. The associated maintenance costs that accompany a complex hydraulic system amplify this handicap. An additional drawback to a mechanically vectored system is the radar cross section impact, a result of exposed actuating surfaces used to move the nozzle.

As an alternative to mechanical vectoring, fixed geometry fluidic thrust-vectoring has been identified as a possible method of eliminating the weight and stealth disadvantages. This concept was introduced as far back as the 1960s with a publication by Thomson et al. [1]. Instead of using a traditional engine gimbal to vector the nozzle, liquid Freon was injected to generate an oblique shock in the supersonic section of the expanding nozzle. This oblique shock induced a change

in angle of the core flow as well as providing asymmetric pressure loading on the nozzle. Since then, new and modified methods have been invented with applications for air-breathing vehicles. The most prominent of these fluidic thrust vectoring techniques are counter-flow control nozzles, shock-vector control nozzles, and throat-shifting dual-throat nozzles. These methods are seen as possible alternatives to mechanical vectoring. The following sections describe each of the techniques in detail.

1.1 Fluidic Thrust-Vectoring Concepts

1.1.1 Counter-Flow

The counter-flow fluidic thrust vectoring technique is a method of nozzle flow control in which secondary flow is induced within an annular region between the primary flow and an outer collar. To induce vectoring of the primary flow, suction is applied on one side of the annular region, as depicted in Figure 1.1, drawing fluid along the collar wall in the opposite direction of the core flow. Asymmetric mass entrainment along the walls causes asymmetric pressure distribution and results in core flow deflection.

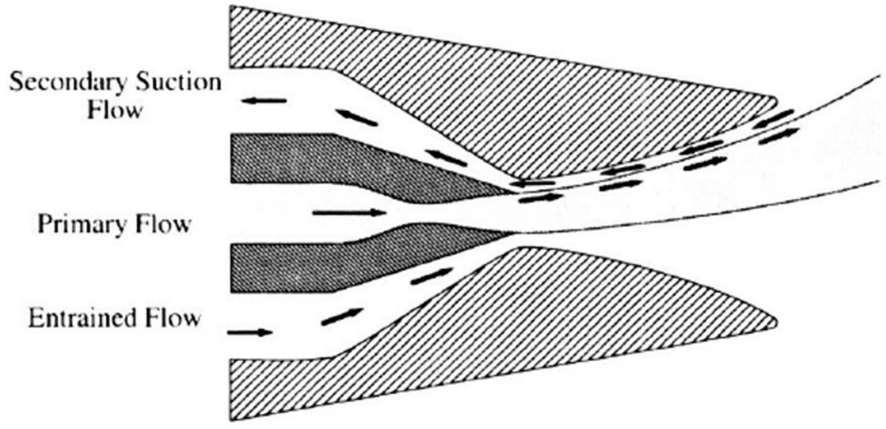

Figure 1.1: Two-dimensional schematic displaying the counter-flow method for fluidic thrust vectoring. [2]

The effect of the counterflow technique is similar to the Coanda effect and has been studied extensively in the literature [3] [4] [5] [6]. Results from these studies have shown the ability for this method to generate relatively large vector angles of 25° at a secondary mass flow rate of 6% of core flow [6]. However, unpredictability in the resulting vector angle as well as hysteresis in the attachment and separation processes of the primary flow have presented complications in the application of this design.

1.1.2 Shock-Vector

Shock-vector control has also been a widely studied technique used for fluidic thrust vectoring due to the simplicity in its application. Specifically, a secondary jet is injected into a supersonic primary flow in the diverging portion of the nozzle generating an oblique shock which is used to turn the core flow, as depicted in Figure 1.2.

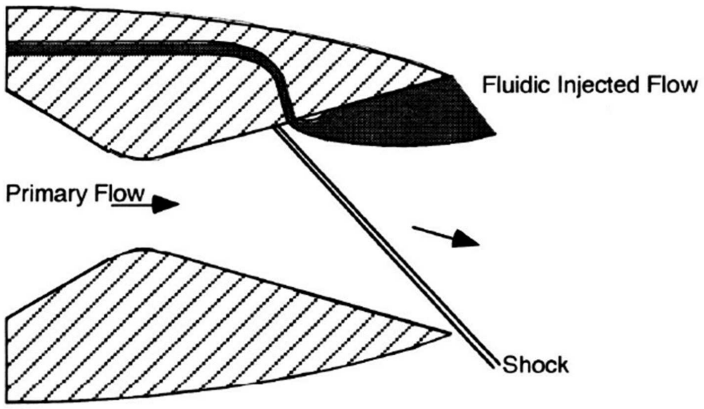

Figure 1.2: Two-dimensional schematic displaying the shock-vector method for fluidic thrust vectoring. [2]

This technique has been shown in the literature to produce large vector angles of 19° at 4% mass injection (relative to the core flow) [2]. Furthermore, the thrust-vectoring angle was shown to be linear with the secondary injection flow rate as long as the generated oblique shock did not impinge upon the opposing wall [7]. However a major disadvantage is that the oblique shock also imposes

a significant total pressure loss within the primary flow. System thrust ratios as low as 0.86 have been seen [2] and are a limitation of this method.

1.1.3 Throat-Shifting (Dual-Throat Nozzle)

The last major fluidic thrust vectoring method is the throat-shifting method which is typically applied in a dual-throat nozzle (DTN) configuration. In this method, secondary flow is injected at the upstream throat of a converging-diverging-converging nozzle in order to bias the relative position of the primary flow closer to either the upper or lower wall as depicted in Figure 1.3. This secondary injection forces the flow to separate and recirculate between the upstream and downstream throats which bends the primary flow through the nozzle.

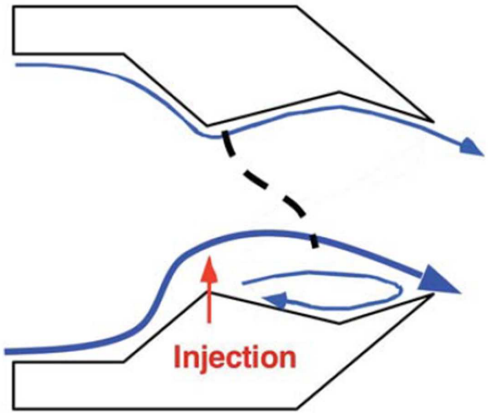

Figure 1.3: Two-dimensional schematic displaying the throat-shifting method for fluidic thrust vectoring in a dual-throat nozzle. [8]

In the DTN configuration the secondary flow is injected just ahead of the upstream throat into the subsonic primary flow. This significantly reduces the total pressure losses as compared to the shock-vector control method. Additionally, prior computational and experimental studies of the DTN configuration have shown it to have moderately high vector efficiency compared to the other two methods while also providing a more predictable response. An additional benefit of the DTN configuration, which is not available in the other techniques, is the ability to control the

aerodynamic throat area using secondary injection on both of the opposing walls at the upstream throat. Specifically, by fluidically varying the aerodynamic throat area, the nozzle performance can be optimized for particular engine throttle and free-stream conditions. To date, research into the DTN technique has largely been conducted at NASA Langley [8] [9] [10] [11] with work focused on parametric studies of variables associated with the thrust-vector performance. Other studies have also been performed in the academic and international setting as well. One such study was performed by Bellandi et al. [12] who investigated a method to optimize nozzle geometry as well as performed an experimental study using a hydraulic analogy. Another study was performed by Gu et al.[13] and investigated the transient secondary injection process. The potential for exploring additional aspects of the DTN technique's comparatively larger parameter space as well as it having the best compromise of thrust-vector performance and system thrust ratio was the reason it was chosen as the focus of the current research investigation.

1.2 Method of Interest

1.2.1 Definition of the DTN Configuration

Of the three methods discussed, the throat-shifting method in the DTN configuration is seen as the most promising candidate for fluidic thrust vectoring due to its relatively high vector efficiency and its potential to be fully integrated into a nozzle system. Therefore the goal of this work was to add to the existing data on the DTN configuration through a combined experimental and computational research effort.

The most significant research on DTN fluidic thrust vectoring configuration was performed by NASA in the mid-2000s in which both computational and experimental studies were conducted [8] [9] [10] [11]. These studies investigated a number of geometric parameters including cavity length, cavity angles, and secondary injection angle and evaluated the influence on thrust vector efficiency, discharge coefficient, and system thrust ratio. The parameters examined include the variables illustrated in Figure 1.4.

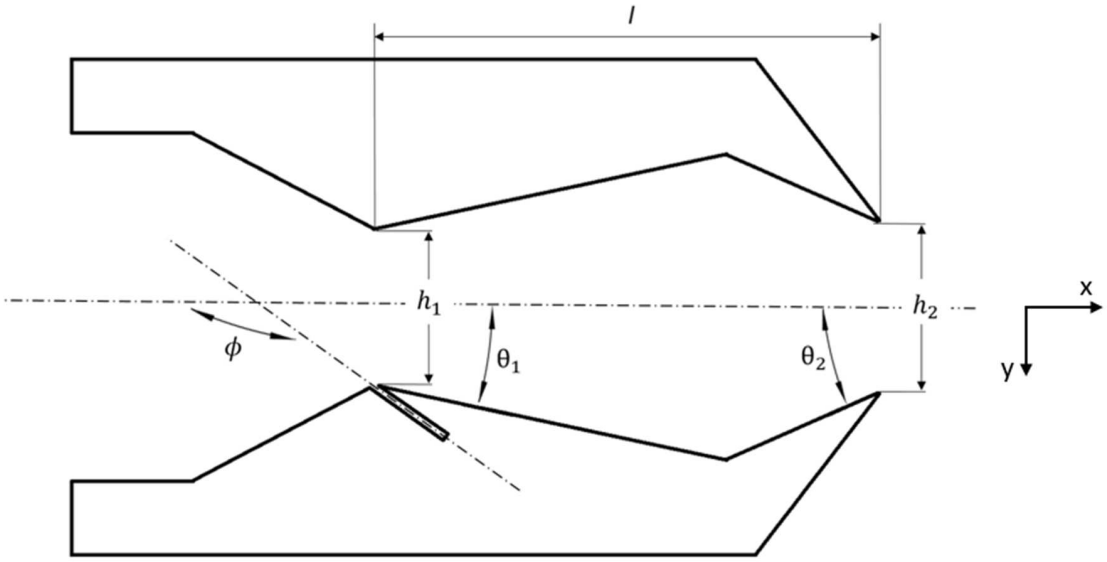

Figure 1.4: Schematic defining the two-dimensional geometry of the dual-throat nozzle (DTN) configuration.

The fundamental shape of the nozzle is defined from five basic parameters: cavity length l, upstream throat height h_1, downstream throat height h_2, nozzle diverging angle θ_1, and nozzle converging angle θ_2. Additionally, the shape of the secondary injection geometry is defined as shown in Figure 1.5.

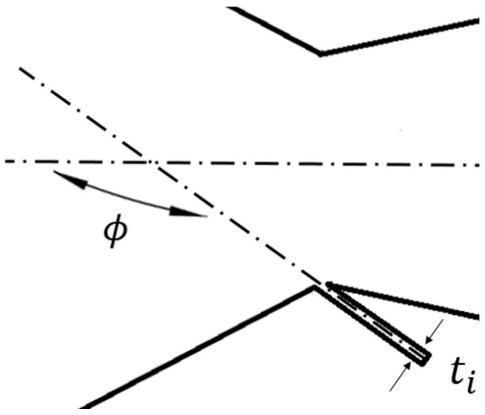

Figure 1.5: A detailed schematic highlighting the two dimensional geometry of the secondary injection within the DTN configuration.

The injection geometry is characterized by both its angle in relation to the core flow, ϕ, as well as the thickness of the injection slot, t_i, in a strict two-dimensional sense. However, cases exist in which the secondary injection geometry is configured as an array of holes instead of a single two-dimensional slot. For this case, secondary injection geometry is described by its area, hole diameter, and distance between holes.

In the study conducted by Deere [8], these parameters were evaluated over a range of flow conditions to determine each of their impacts on the DTN performance. This study included computational simulations with PAB3D, and CFD code, as well as experimental measurements obtained from the NASA Jet Exist Test Facility pictured in Figure 1.6.

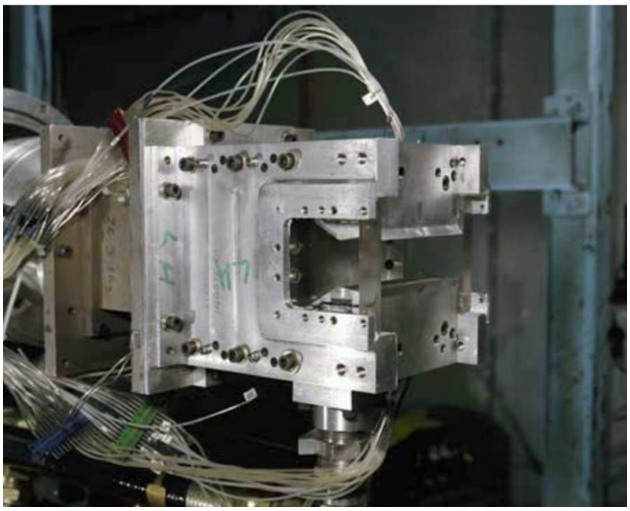

Figure 1.6: NASA Langley Research Center Jet Exit Test Facility utilized by Deere. [8]

The data from these tests showed a clear correlation between several notable parameters and the thrust-vector efficiency. As an example, Figure 1.7 shows results from Flamm et al. [10] which displays the influence of the secondary injection angle on the resulting thrust-vectoring angle as a function of the injection percentage. This work shows that there exists an optimal secondary injection angle near 150^o where the thrust-vectoring angle is maximized for equivalent injection percentages.

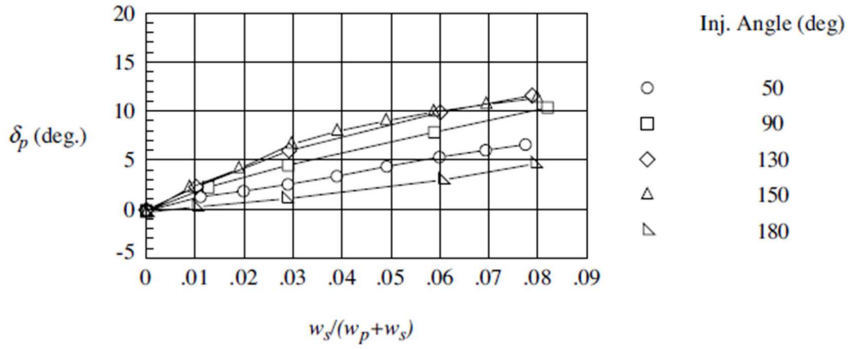

Figure 1.7: Thrust-vector angle as function of injection percentage $\frac{w_s}{w_p+w_s}$ and injection angle ϕ [10].

Another key parameter that was investigated was the shape of the injection port, or injection type as defined by Flamm et al. [10]. Its influence is presented in Figure 1.8 where single arrays of circular holes at two different diameters are compared with a single two-dimensional slot spanning the nozzle width. The integrated exit areas for these injection shapes were $0.0864\,in^2$, $0.1909\,in^2$, and $0.0864\,in^2$ for the small holes, large holes, and slot, respectively. Observing trends in the data, the slot can be see to outperform the hole geometry with an equivalent area up to about $\eta = 3\%$ injection ($w_s/(w_p + w_s) = 0.3$). Additionally, the small holes outperform the large holes across the whole range of injection percentages. These results, from Flamm et al. [10] significantly influenced the design and testing of the DTN configuration pursued in the current research which will be thoroughly discussed in the proceeding sections.

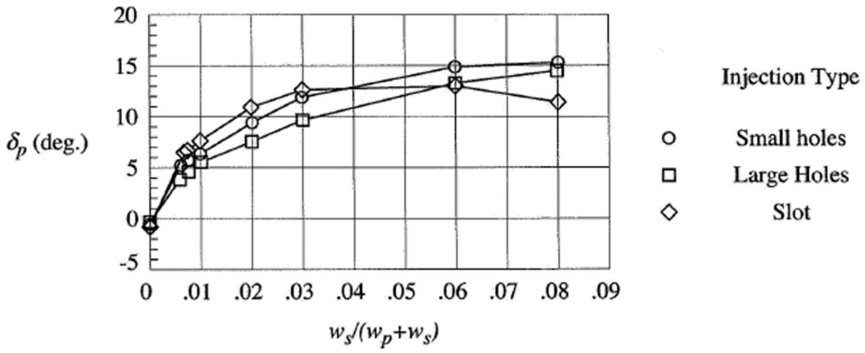

Figure 1.8: Thrust-vectoring angle as a function of injection percentage η, and injection shape [10].

Chapter 2

Current Study

2.1 Geometry

In an attempt to consistently build upon the results from the previous work, the geometry used for this study was heavily based on the geometry used by Flamm et al. [10]. However, due to limitations in the test hardware, the mass flow rates achieved during the Langley study were not achievable with the available apparatus. The mass flow rate is largely driven by the throat height and width, which were 1.15 in (29.2 mm) and 4 in (101.6 mm), respectively, in Flamm et al. [10]. An acceptable nozzle cross sectional area was calculated using the isentropic mass flow parameter equation shown in Equation 2.1, based on mass flow limitations of the CU Boulder compressible flow wind tunnel of $\dot{m} = 0.15$ kg/s.

$$\dot{m} = \frac{A\ p_t}{\sqrt{T_t}} \sqrt{\frac{\gamma}{R}} M\ (1 + \frac{\gamma - 1}{2} M^2)^{\frac{-\gamma-1}{2(\gamma-1))}} \tag{2.1}$$

This gave a maximum area allowable for this system of 0.3 in^2 (194.1 mm^2) based upon a maximum nozzle pressure ratio (NPR) of 4 at atmospheric conditions in Boulder, CO. A predetermined test section width of 0.5 in (12.7 mm) was chosen, sized in order to minimize test section boundary layer effects, and resulted in a maximum throat height of 0.547 in (13.9 mm). This value was rounded down to 0.5 in (12.7 mm) for geometric simplicity, while also providing a factor of safety in the design calculations. All of the remaining nozzle dimensions were scaled by a factor of 2.3, the ratio of the throat heights between the Flamm et al. study and current study, as displayed in Figure 2.1.

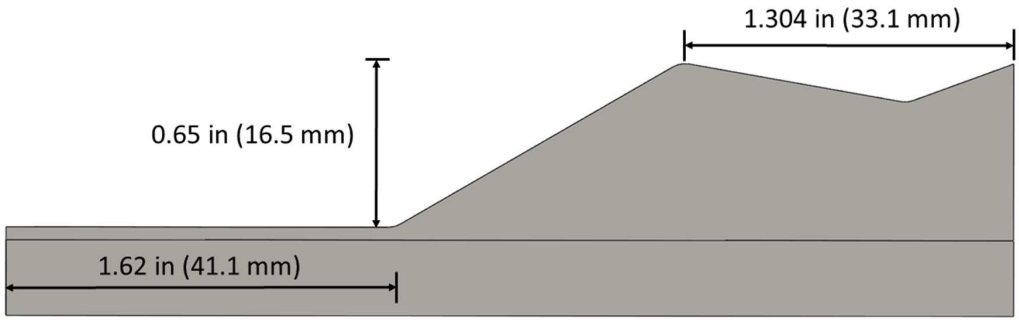

Figure 2.1: Cross-section of nozzle test insert dimensions.

Additionally, due to limited availability of information regarding specific details associated with the nozzle design in Flamm et al. [10], several estimates of the secondary geometry components in the DTN were made based on available images. Image analysis of pictures yielded a ramp angle up to the upstream throat of 30 degrees, while features like the fillet radius of the throat were more difficult to deduce. These features were ultimately decided based on the radius required to ensure a smooth surface within the expected manufacturing tolerances. Figure 2.2 defines the additional geometry used for each test case.

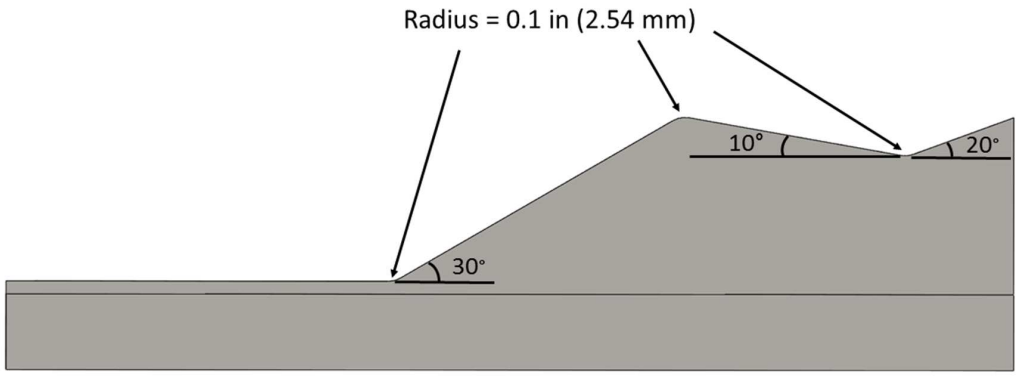

Figure 2.2: Cross-section of nozzle test insert fillet radius' and angles.

Throughout this study, tests were conducted on three different test geometries in which the secondary injection geometry was the only geometric variable. The secondary injection geometry

employed expanded upon the investigation in Flamm et al. [10] by testing injection slots of two different thicknesses as well as one case where the two-dimensional slot was replaced by an array of circular holes. The total area of the secondary injection, was largely driven by limitations in the mass flow controller which delivered gas for secondary injection. Injection pressure was limited to 140 psi (965 kPa) which meant that in order to provide an adequate percentage of core flow, the injection geometry area was increased. This resulted in the following injection geometry properties shown in Table 2.1. Figure 2.3 (a)-(c) shows the secondary injection geometry for each of these cases.

Table 2.1: Nozzle test insert secondary injection dimensions.

Property	V1 (Slot)	V2 (Slot)	V3 (Holes)
Thickness/Diameter	0.01 in (0.25 mm)	0.015 in (0.38 mm)	0.033 in (0.84 mm)
Area	0.0039 in^2 (2.5 mm^2)	0.0068 in^2 (4.4 mm^2)	0.0039 in^2 (2.5 mm^2)
No. of Slots/Holes	1	1	9
Injection Angle ϕ	150°	150°	150°

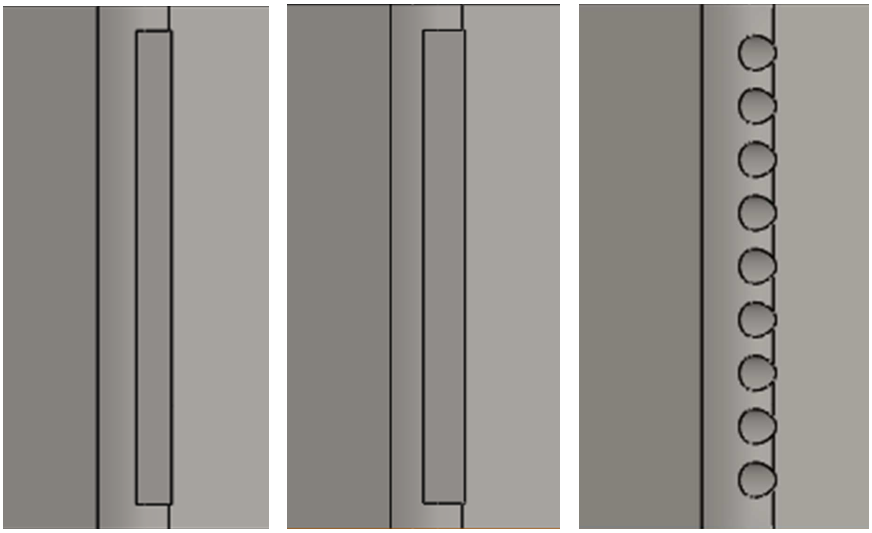

(a) V1 (b) V2 (c) V3

Figure 2.3: Top view of nozzle insert secondary injection geometries.

2.2 Test Medium

The gas medium used in the experimental and computation studies was nitrogen and was chosen primarily because the local supply cost was found to be half that of air, which was rated for breathing purposes. Additionally, no effect on performance was predicted since the properties of nitrogen at room temperature are very similar to that of air, as shown in Table 2.2.

Table 2.2: Relevant properties of Air and Nitrogen

Property	Air	Nitrogen
Density	$1.293\ \frac{kg}{m^3}$	$1.2506\ \frac{kg}{m^3}$
Dynamic Viscosity	$1.73 \cdot 10^{-5}\ Pa-s$	$1.66 \cdot 10^{-5}\ Pa-s$
Ratio of Specific Heats	1.4	1.4

In order to quantify any variation in the results based on the use of nitrogen as opposed to air, tests using both gases were conducted with identical experimental setups. The configuration used nozzle test insert V2 with a NPR of 4. Figure 2.4 shows the results from three tests using air and nitrogen. It can be seen that the deflection angle matches within the measurement uncertainty for each case, although air also seems to show a slight positive bias for all three secondary injection percentages tested. Nevertheless, the results were deemed to be close enough to justify the use of nitrogen.

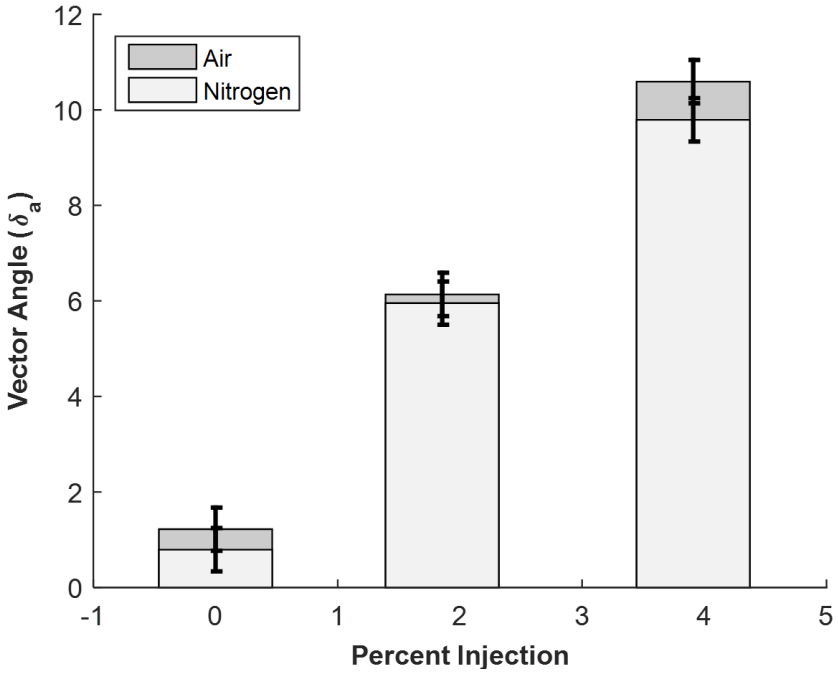

Figure 2.4: Comparison of flow vector angle using Air versus Nitrogen.

2.3 Flow Conditions

To quantify the performance of the DTN across different flow conditions, experimental and computational results were targeted for NPRs of 2 and 4. The direct relationship between NPR and Reynolds number was expected to influence the flow separation characteristics within the nozzle due to changes in the ratio of inertial to viscous forces within the flow. Throughout the course of experimental testing, data was collected for a NPR of 2 with variability between tests of about 2% in the NPR. However, for tests in which a NPR of 4 was targeted, an offset between the expected system maximum mass flow rate and the actual delivered mass flow rate resulted in an average NPR of 3.7, a discrepancy of 7.5% from the nominal value. Although this bias was not desirable, the results still provide insight into the effect that Reynolds number has on DTN performance. To simplify presentation, all tests in which a NPR of 4 was targeted will be referenced as such, even though the actual value was biased lower.

2.4 Computational Setup

In order to better understand the trends observed in the experimental data, a computational fluid (CFD) study was conducted. The data from the computational study was used to enhance the spatial resolution past what was achievable within for the experiment, while also increasing the confidence in the experimental results. Limited resources ultimately directed the focus of this computational study on trends in the deflection angle as a function of injection mass flow rate instead of precise solutions of pressures and velocities within the flow field.

2.4.1 Solvers and Meshers

The solver chosen to conduct this study is the commercially available code StarCCM+. This code was chosen largely due to its availability as a free resource for student research. The unstructured code is able to solve a range of problems from low Reynolds number incompressible flows to hypersonic flows with the ability to use Reynolds Averaged Navier Stokes (RANS), Large Eddy Simulation (LES), and Detached Eddy Simulation (DES) modeling. Specifically for RANS, turbulence closure was available through Spalart-Allmaras, K-Epsilon, K-Omega, or Reynolds Stress. Meshing was performed using an integrated meshing tool in StarCCM+ which was capable of generating unstructured polyhedral, quadrilateral, and triangular meshes. Additional prism layers could be generated in order to better resolve the boundary layer.

2.4.2 Models Used

Two-dimensional RANS with a K-Epsilon two layer turbulence closure model was chosen to conduct the computation study largely due to limitations in computational resources. In RANS, the Navier-Stokes equations are decomposed into mean and fluctuating components. This decomposition generates an additional term called the Reynolds stress tensor. Closure with this additional term can be achieved with a K-Epsilon model, which calculates turbulent viscosity and turbulent kinetic energy to model the Reynolds stress tensor. The two layer K-Epsilon model differs from

the standard model in that the computation is separated into two separate layers, one near the wall and one away from the wall. In the layer near the wall, the turbulent viscosity is specified as function of distance from the wall. These near wall values then blend with the values in the layer away from the wall and the turbulent kinetic energy is solved for in the entire flow.

2.4.3 Geometry

The geometry developed for the computational study is very similar to the geometry used for the experiment. However, unlike the experiment, a two two-dimensional computational study was undertaken in order to decrease the computational resource requirements. Figure 2.5 shows an example of the nozzle geometry used.

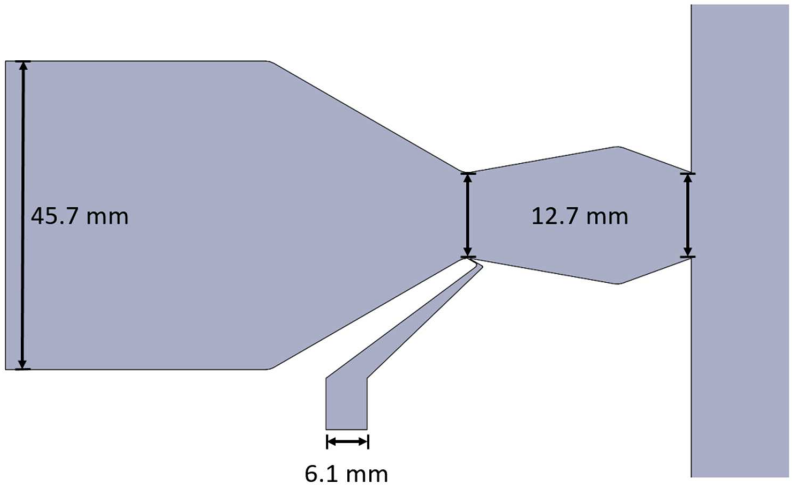

Figure 2.5: Relevant computational dimensions of nozzle.

To ensure similarity between the computational results and the experimental results, identical nozzle geometries were used, however, the freestream exhaust region was limited in size to ensure timely convergence in the computational simulations. To limit the effect of the upper and lower exhaust boundaries, each was symmetrically extended to 20 times the throat height of the nozzle. However, it was found that extending the right boundary further than 15 times the throat area from the nozzle exit resulted in large numerical oscillations and poor convergence. Since extending

this boundary further was found to have little impact on vector angle and the flow properties in the exhaust jet were not relevant to this study, the right boundary was fixed at 15 times the throat height. Figure 2.6 shows the extent of the freestream exhaust region of the geometry.

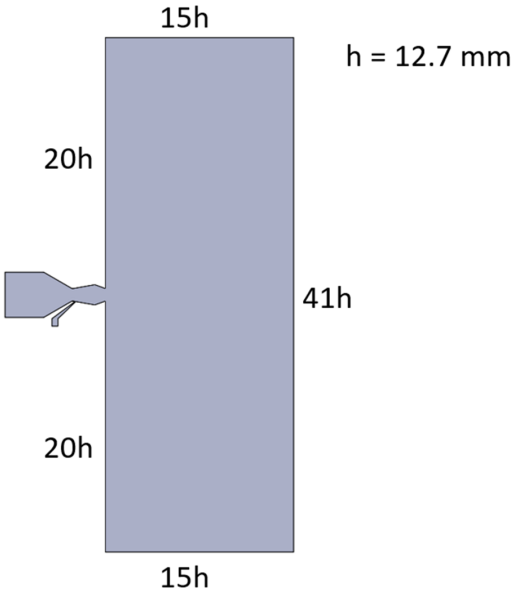

Figure 2.6: Relevant computational dimensions of exhaust domain.

2.4.4 Boundary Conditions

The boundary conditions for each test case were defined in order to match the experimental conditions as accurately as possible. To prescribe a NPR, a stagnation inlet boundary condition is used for the primary inlet and a total pressure of the flow is defined. Secondary injection is also prescribed using the same boundary condition in which total pressure is prescribed based on the flow rate desired. The rest of the boundaries are defined to be no-slip walls. Figure 2.7 shows an illustration of the boundary conditions.

Exhaust boundary conditions were also prescribed to accurately mirror the experimental setup. The three downstream boundaries were defined with a pressure outlet boundary condition which specifies a static pressure at the boundary. However, the two boundaries directly above

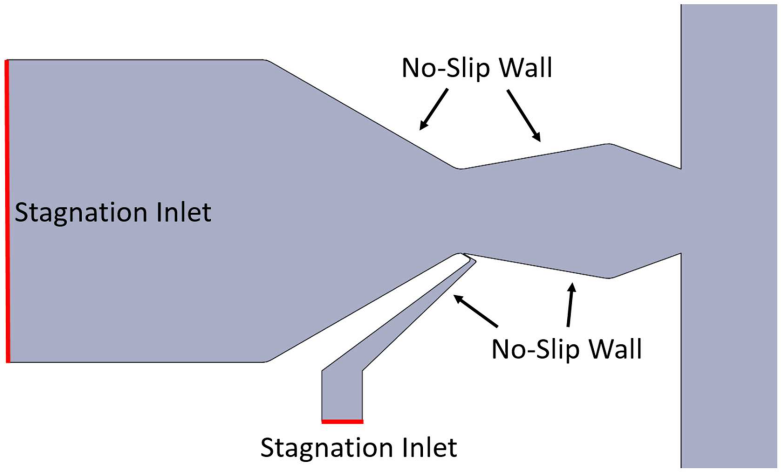

Figure 2.7: Nozzle boundary conditions.

and below the nozzle exit were set as no-slip walls in order to mimic the experimental setup. An illustration of the exhaust boundary conditions are shown in Figure 2.8.

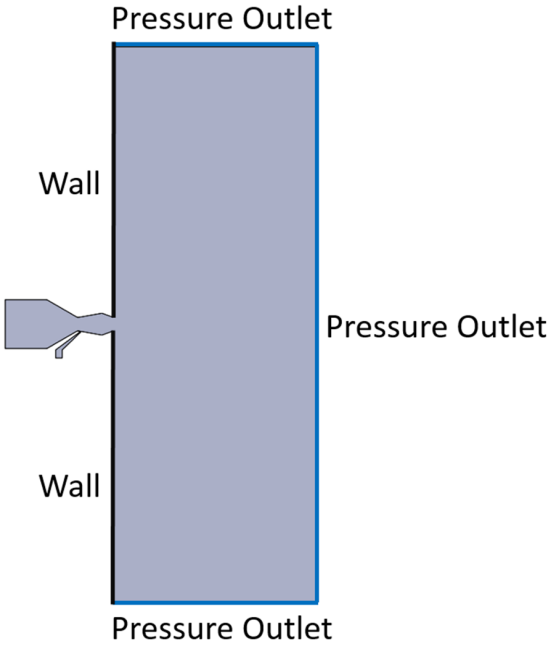

Figure 2.8: Exhaust boundary conditions.

2.4.5 Meshing

The grid was generated using the built in StarCCM+ grid generator which has three types of grids available: polygonal, quadrilateral, and triangular. The polygonal grid was chosen after a number of trial runs showed it to provide the most accurate solution of the available options. The size of the polygonal grids were modified based on where the most important flow structures were expected. This meant that the highest grid density was focused around the site of secondary injection as well as along the nozzle walls. Figure 2.9 shows a view of the main nozzle geometry after grid generation and Table 2.3 shows the grid dimensions for each of the regions.

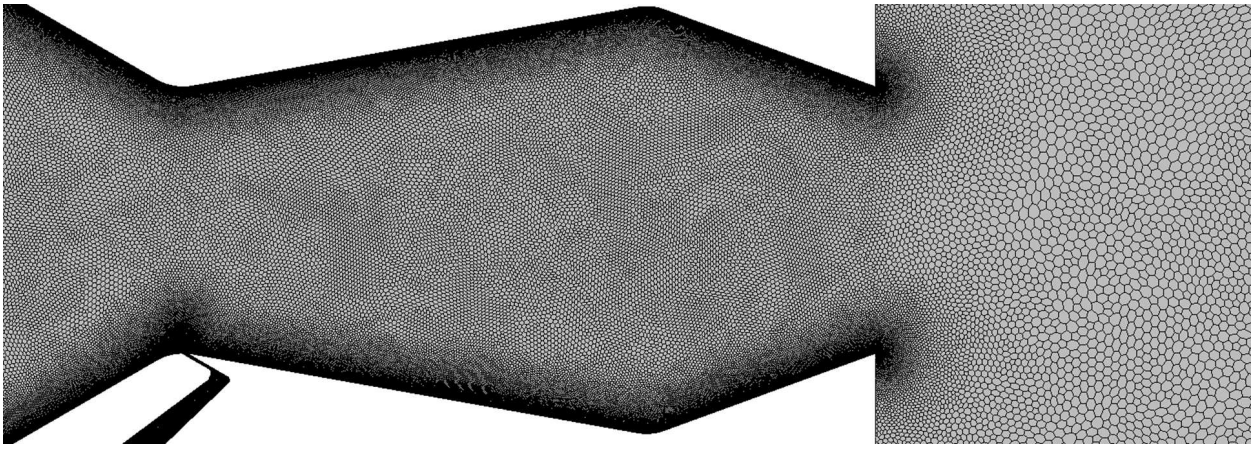

Figure 2.9: Nozzle mesh density example.

Table 2.3: Grid Dimensions

Nozzle Core	Nozzle Wall	Injection	Exhaust	Freestream
0.0079 in	0.00079 in	0.0016 in	0.02 in	0.063 in
(0.2 mm)	(0.02 mm)	(0.04 mm)	(0.5 mm)	(1.6 mm)

In addition to the higher density grid at the nozzle near wall region, an additional prism layer was generated. This prism layer was created in order to better resolve the boundary layer and generate a dimensionless wall distance y+ on the order of 1 to 30. This near wall region is shown in Figure 2.10.

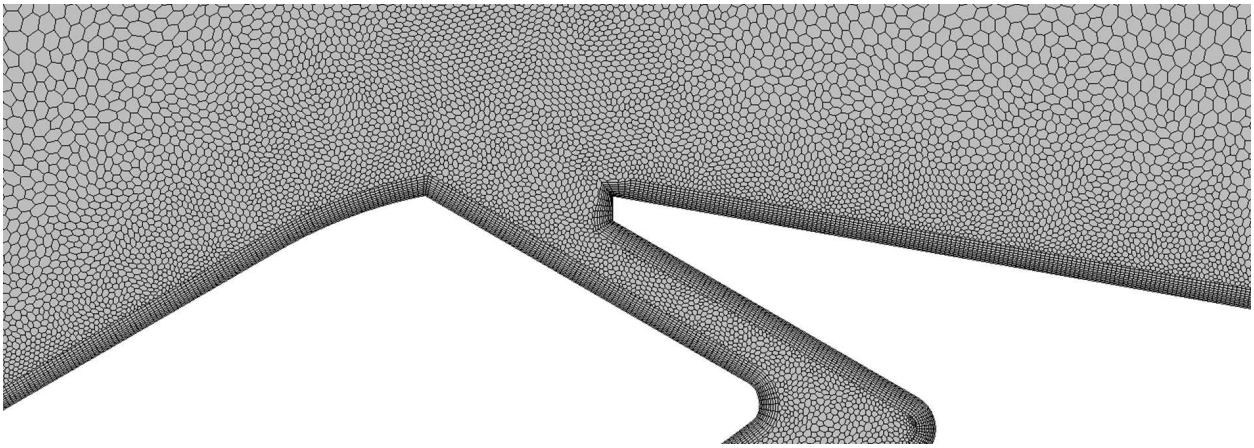

Figure 2.10: Nozzle prism layer mesh example.

The grid dimensions were determined through an iterative method where the convergence performance of a number of trial runs with different grid densities was evaluated. Particular attention was paid to ensuring that the near wall regions and the throat had a high density of points so that sharp gradients and boundary layer separation were captured. On the other hand, the density of the grid in the exhaust region at the exit of the nozzle and the freestream region further downstream of the nozzle exit were found to have little impact on both the nozzle wall pressures and the thrust-vector angle of the primary flow. This allowed for a less dense mesh to be generated in this region. To ensure the grid density chosen was appropriate, a grid convergence study was conducted. The grid density at each location in the geometry was changed proportionally and the resulting integrated wall pressure profile and vector angle were retrieved. Figure 2.11 (a) and (b)show the integrated upper and lower wall pressure and thrust-vector as a function of total grid density respectively.

The plots show convergence for both of the properties at a value of about 400,000 cells. To provide a safety margin, the total number of cells was ultimately increased to approximately 560,000 cells with the grid dimensions shown in Table 2.3. Additionally, to ensure similarity between simulations, the same settings were used for each nozzle secondary injection geometry. This meant

that although the total number of grid points between test cases changed slightly, the grid density remained unchanged.

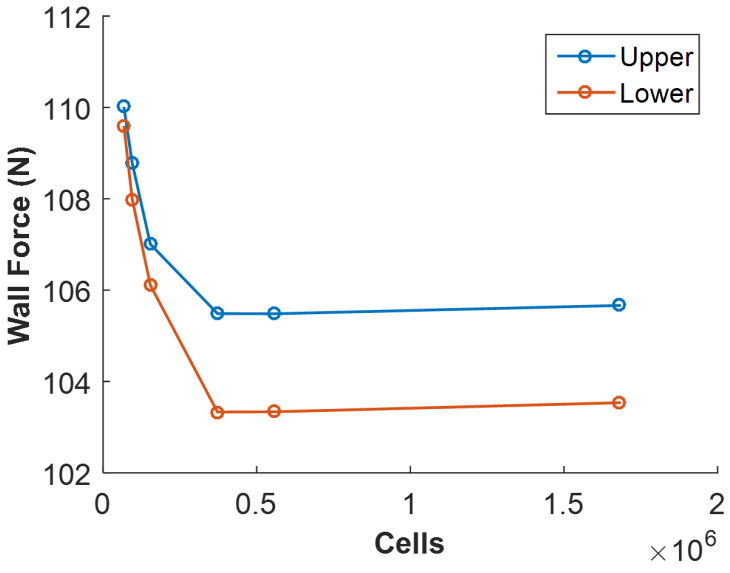

(a) Force Convergence

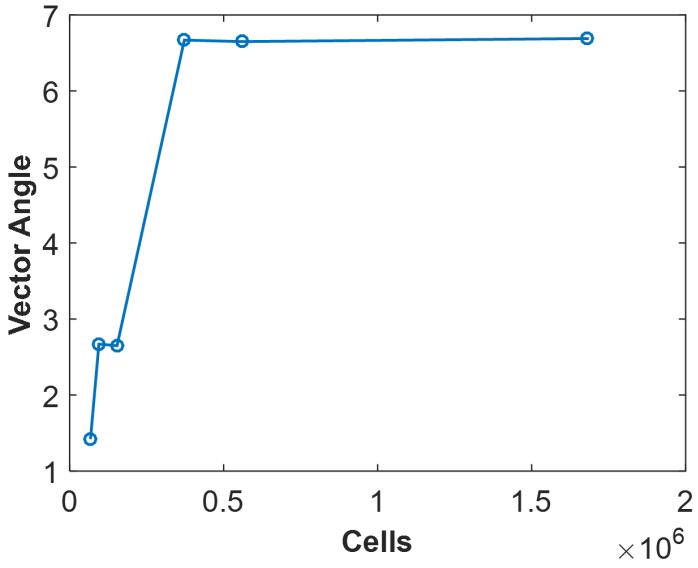

(b) Thrust-Vector Angle Convergence

Figure 2.11: Grid convergence for thrust-vector angle and net vertical force.

2.5 Experimental Setup

To best mimic the two dimensional results from the computational study as well as to provide qualitative schlieren images, a quasi-two-dimensional experimental test apparatus was designed and tested. Quasi-two-dimensionality is achieved by extruding the two dimensional computational geometry in the z (third, out of plane) direction. The facility used to conduct the experiments is a high speed compressible flow wind tunnel built at CU Boulder. The system was modified from an existing blowdown wind tunnel, which was built as the capstone design project, SWIFT. However, due to a number of limitations in the current system, several major modifications were made. The following sections detail the final configuration of the system after these modifications.

2.5.1 Pneumatic System

The pneumatic system consists of seven main components which store and deliver compressed gas to the test section. It is worth noting that the pneumatic system is further divided into two sub-systems associated with the primary flow and the secondary injection flow. The layout of these components are shown through the plumbing schematic in Figure 2.12.

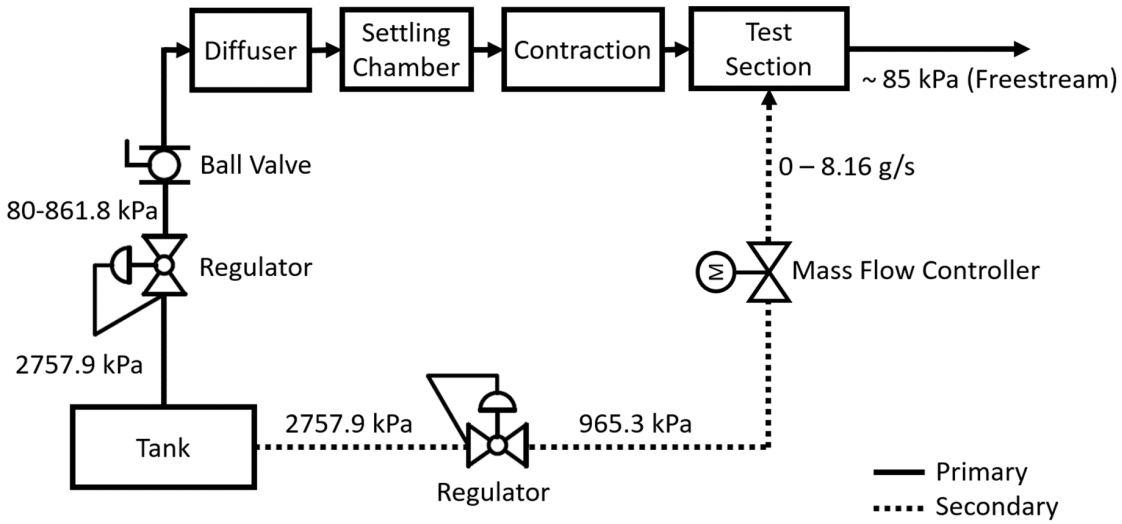

Figure 2.12: Pneumatic system schematic.

These two systems are completely independent with the exception of the compressed gas tank and have different methods of maintaining flow conditions.

2.5.1.1 Primary Pneumatic Sub-System

In the primary sub-system, the flow originates from the single pressurized storage tank at a maximum pressure of 400 psi (2757.9 kPa). The pressure is then regulated down to $11.6 - 125$ psi (80 $-$ 861.8 kPa) depending on the test case being run. A ball valve positioned after the regulator is used to initiate or stop flow from the regulator. Flow is then introduced into a conical diffuser and cylindrical settling chamber to dampen any flow imperfections introduced by the regulator. A contraction after the cylindrical settling chamber transitions the flow from a circular to a rectangular cross-section and introduces it to the quasi-2D test section. Mass flow rate through the primary system is dependent entirely on the pressure set by the regulator and the minimum throat area in the test section (the upstream throat in the DTN geometry).

2.5.1.2 Secondary Pneumatic Sub-System

The secondary flow is provided by the same pressurized storage tank used for the primary flow, but is regulated down to a fixed pressure of 140 psi (965.3 kPa) by an independent regulator. Flow at this pressure is then delivered to an Alicat Scientific MCR-500SLPM-D/5M mass flow controller which regulates the flow rate based upon a locally commanded mass flow rate. The flow is then delivered directly to the test section through the secondary injection path designed into the test-section nozzle blocks.

2.5.1.3 Tank

The tank chosen for this system was largely driven by size and cost constraints. The tank is required to fit within a portable cart which is capable of fitting though a standard 32 in (0.813 m) door frame. While this limited tank dimensions, cost limited the pressure rating of the tank since assemblies that had a MAWP of greater than 800 psi (5516 kPa) were cost prohibitive. The

tank ultimately used is a 30 *gallon* (0.114 m^3) assembly from Manchester Tank with a MAWP of 600 *psi* (4137 kPa). The tank is equipped with three ports, one of which is used for pressurizing the tank, and another for feeding the pneumatic system. Figure 2.13 shows a three-dimensional rendering of the type of tank used.

Figure 2.13: Three-dimensional rendering of the 30 *gallon* Manchester tank used in the wind tunnel.

2.5.1.4 Primary Flow Regulator and Ball Valve

The control valves used in the primary flow system were both manually operated valves, a decision once again largely driven by cost. The role of the regulator was to maintain the total pressure being delivered to the test section, thus maintaining a test section NPR. The regulator used is a Marsh Bellofram Type 78 pressure regulator. This regulator was chosen based on its ability to provide flow rates of up to 0.15 $\frac{kg}{s}$ for a NPR of 4. Since the inlet MAWP of the regulator is 400 *psi* (2758 kPa), 200 *psi* (1378.9 kPa) below the MAWP of the storage tank, the available test time decreased by over 33%. Though not ideal, the reduced performance still was capable of providing at least 5 seconds of test time at a NPR of 4. The manual ball valve was positioned immediately downstream of the regulator to provide a failsafe in case of a full-open failure of the regulator in addition to reducing the primary flow total pressure transient during startup.

2.5.1.5 Diffuser

A diffuser is incorporated in the design of the pneumatic system primarily to provide conditioned, uniform flow to the test section. Additionally, the large change in area associated with the diffuser allows for an accurate calculation of the mass flow rate using the venturi effect. Figure 2.14 shows a cross section of the entire diffuser and test section.

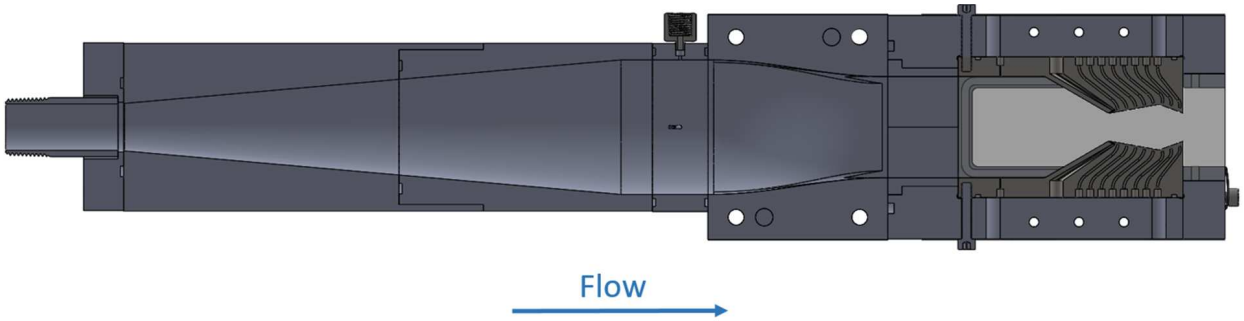

Figure 2.14: Diffuser and test section cross-section.

The diffuser is sized based on three parameters, the area ratio, the initial diameter, and the total length. The maximum length of the diffuser was estimated by maximizing its length, while ensuring that the test section remained within the dimensions of the tabletop. The diffuser inlet diameter was fixed as well based on the diameter of the flexhose feeding the diffuser. The area ratio of the diffuser was determined to maintain a flow velocity in the settling chamber between 3 m/s and 30 m/s, as recommended by Pope and Goin [14]. These limits ensure uniformity and prevent convection currents from developing. Assuming a settling chamber velocity of 10 m/s, the diffuser area ratio between the diffuser inlet and outlet was calculated to be approximately 9, which results in a diffuser divergence angle of approximately 10°. This divergence angle was deemed to be acceptable since it is close to the minimum loss coefficient achievable for this area ratio as seen in Figure 2.15. Based on the geometry extracted from the prior analysis, the diffuser dimensions generated are shown in Figure 2.16.

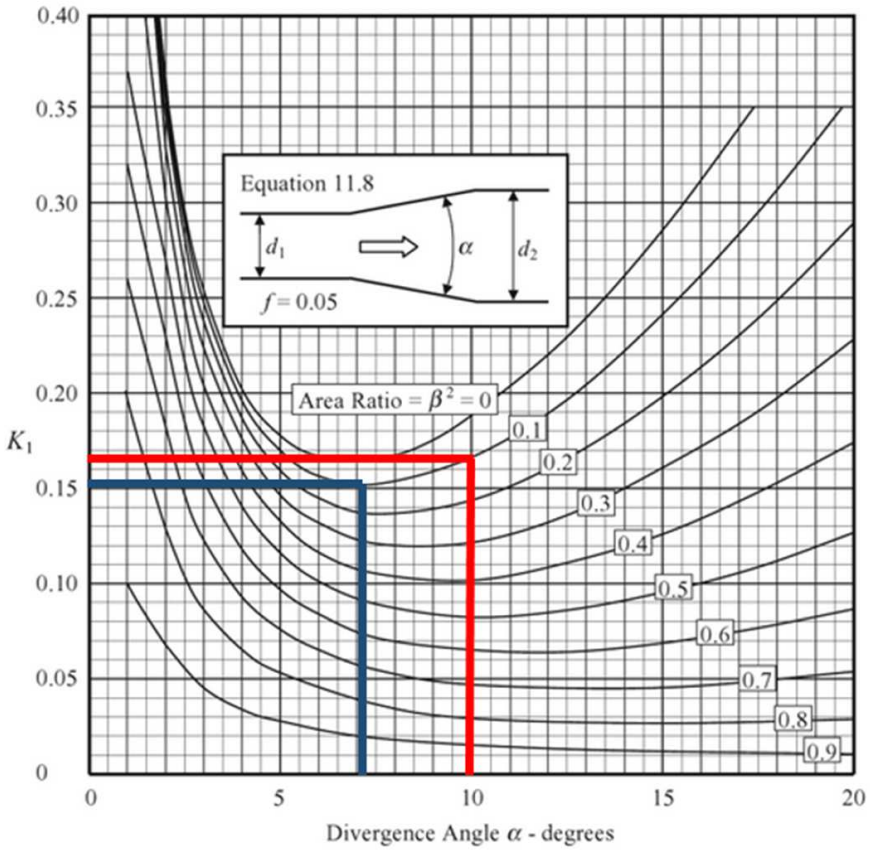

Figure 2.15: Diffuser pressure loss performance. (Rennels and Hudson [15])

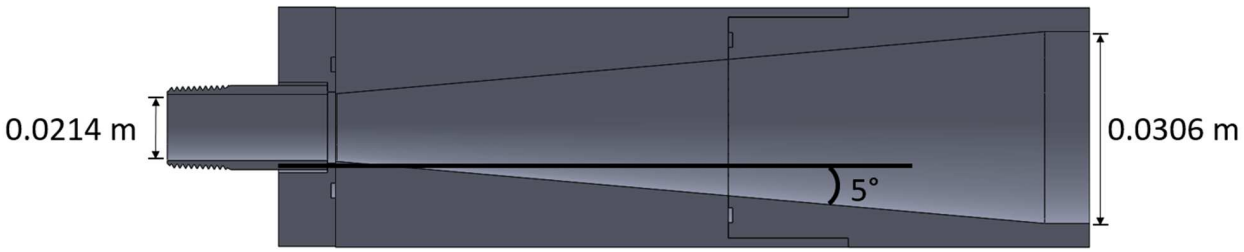

Figure 2.16: Diffuser dimensions.

The diffuser was fabricated in three separate pieces in order to simplify manufacturing. The first piece is a short section to which a hose fitting is welded. The second and third sections are the diverging portions of the diffuser which were separated to allow for the use of a shorter boring

bar. The next piece after the diffuser is a short 0.0254 m long straight section used as both a settling chamber and for instrumentation. Specifically, measurements of the total pressure, total temperature, and static pressure were all performed in this section. Figure 2.17 shows the layout of the instrumentation/settling chamber.

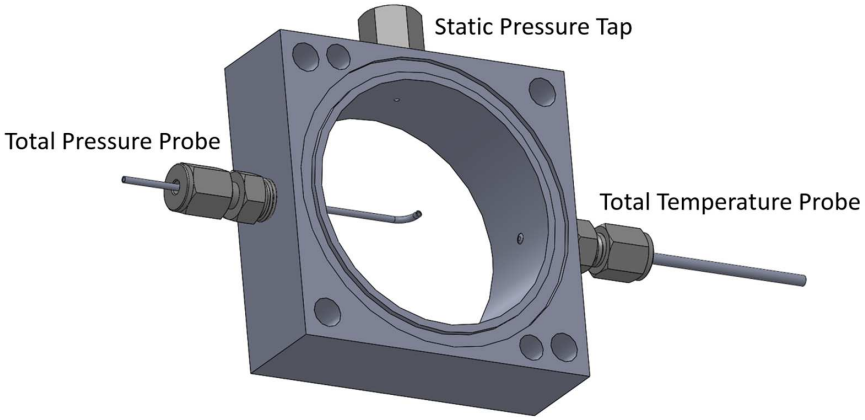

Figure 2.17: Instrumentation and settling chamber.

The last section before the test section is a converging circular to rectangular contraction meant to smoothly transition the flow to the rectangular cross section of the test section. The contraction blends smoothly from a 2.39 in (60.7 mm) diameter circle to a 1.8 in (45.72 mm) by 0.5 in (12.7 mm) rectangular cross section. This means that in both dimensions the profile is converging ensuring there is a negative pressure gradient and no boundary layer separation. In addition, this allows the contraction distance to be shortened greatly using the lofted cut feature in Solidworks. A key requirement when using this feature was that the profiles at the entrance and exit are normal to the direction of the flow ensuring parallel flow entering and exiting the contraction. Figures 2.18 (a)-(c) show the upstream, downstream, and a cross-section views respectively.

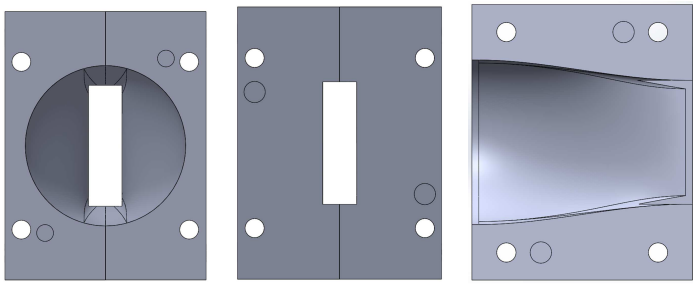

(a) Upstream (b) Downstream (c) Cross-section

Figure 2.18: Rendered views of the circular to rectangular contraction section.

2.5.1.6 Test Section

The test section was designed in a modular fashion to secure the nozzle test inserts and provide an unobstructed view for the dual-field schlieren system. The test section is assembled by first inserting the two nozzle test inserts into upper and lower test section surfaces as shown in Figure 2.19 (b). After the inserts are placed in the test section, two 0.5 in (1.27 mm) thick cast acrylic windows are placed between the nozzle inserts to secure them. Additionally, panels are secured to both sides to prevent lateral movement of the windows. The final configuration is shown in Figure 2.19 (c).

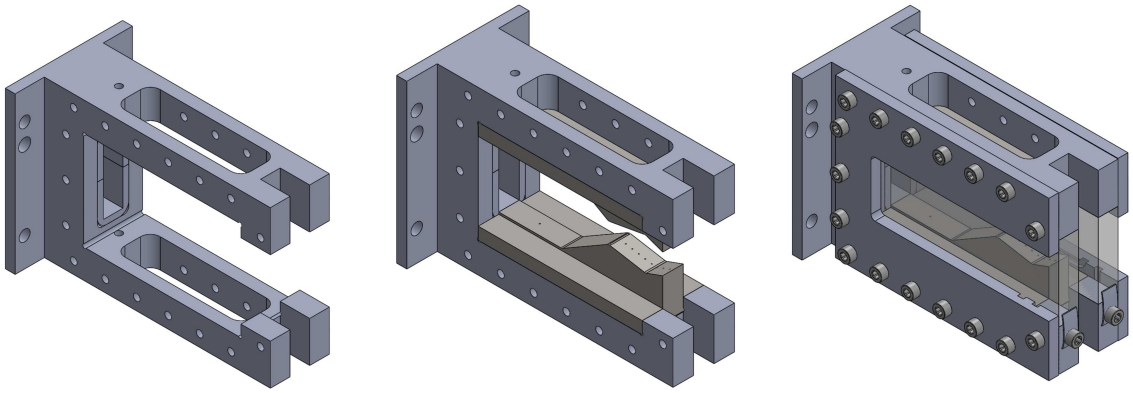

(a) Empty Configuration (b) Test Insert Installed (c) Fully Assembled

Figure 2.19: Test insert installation progression in test section.

2.5.1.7 Nozzle Test Inserts

The nozzle test inserts are interchangeable test pieces that allow for a variety of geometries to be tested. Two separate inserts are required for each test and allow for the lower and upper profiles to be changed independently. Flow properties are collected through the use of pressure taps along the nozzle walls. Internal channels are included in the nozzle blocks to transmit the pressure from each tap to the pressure transducers. Due to the complex geometries required for these pressure taps, the nozzle test inserts were constructed using additive manufacturing. The designs were outsourced to the 3D printing service company Shapeways for manufacturing using their Frosted Ultra Detail printing specification. This specification uses a multijet additive manufacturing process which deposits molten acrylic polymer onto a build platform in successive layers. During this process wax is used as support material and each layer is cured with UV light. After construction, the support wax is melted out. Because wax was used to fill the pressure taps during manufacturing, the pressure taps had a minimum diameter requirement to ensure the wax could drain. Pressure tap diameters that were too small resulted in plugged channels. Due to volumetric and manufacturing limitations, the number of wall pressure taps was limited to 8 between the upstream and downstream throats in the DTN geometry. The diameter of each pressure tap was prescribed to be 0.0025 in (0.0635 mm) and was a lower limit based on the manufacturing tolerances of the additive manufacturing process. Figure 2.20 shows an example of the cross-section of a test insert while Figure 2.21 and Table 2.4 show the layout of the pressure taps.

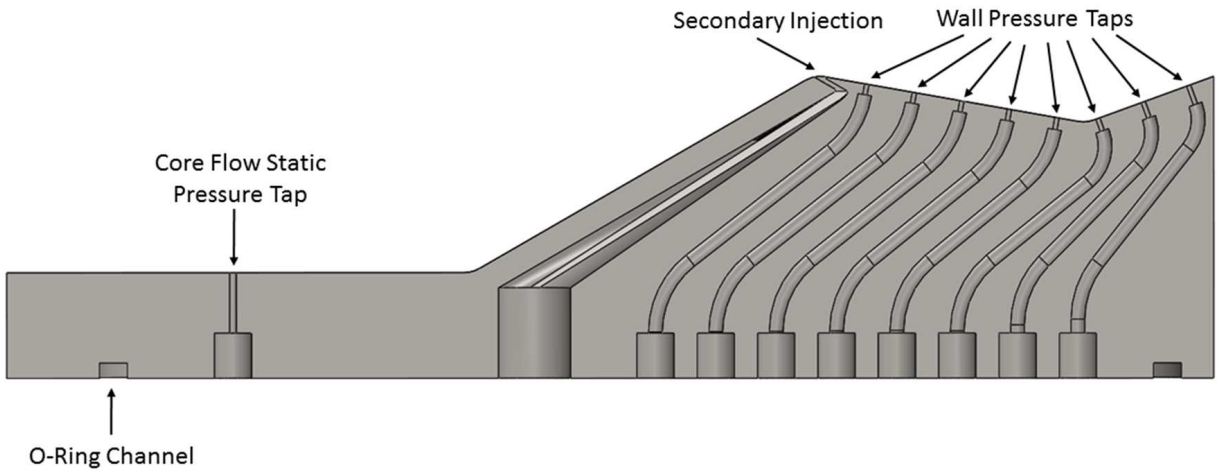

Figure 2.20: Nozzle test insert cross-section.

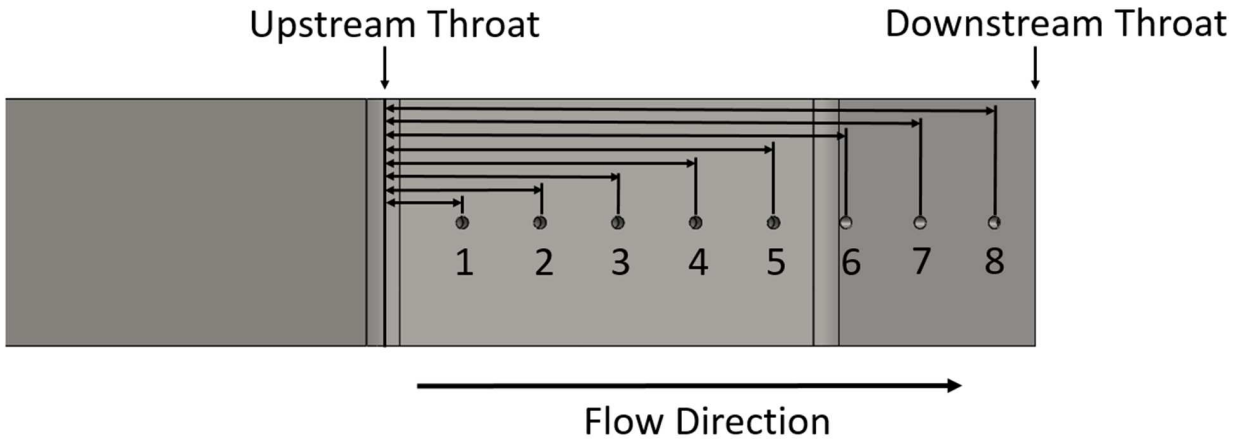

Figure 2.21: Nozzle test insert pressure tap locations.

Table 2.4: Pressure Tap Locations

Tap No.	x *Distance* (mm)
1	3.653
2	7.655
3	11.657
4	15.660
5	19.662
6	23.387
7	27.206
8	21.025

2.5.2 Electrical and Data Acquisition Setup

The electrical system consists of the data acquisition system and power supplies to power the mass flow controller and LED light for the schlieren system. The sensors used in the data acquisition system comprised of a K-type thermocouple, 20 absolute pressure transducers, and a differential pressure transducer. Figure 2.22 shows a schematic of the electrical system with the specifications for the transducers shown in Table 2.5 and specifications of the National Instruments data acquisition modules shown in Table 2.6.

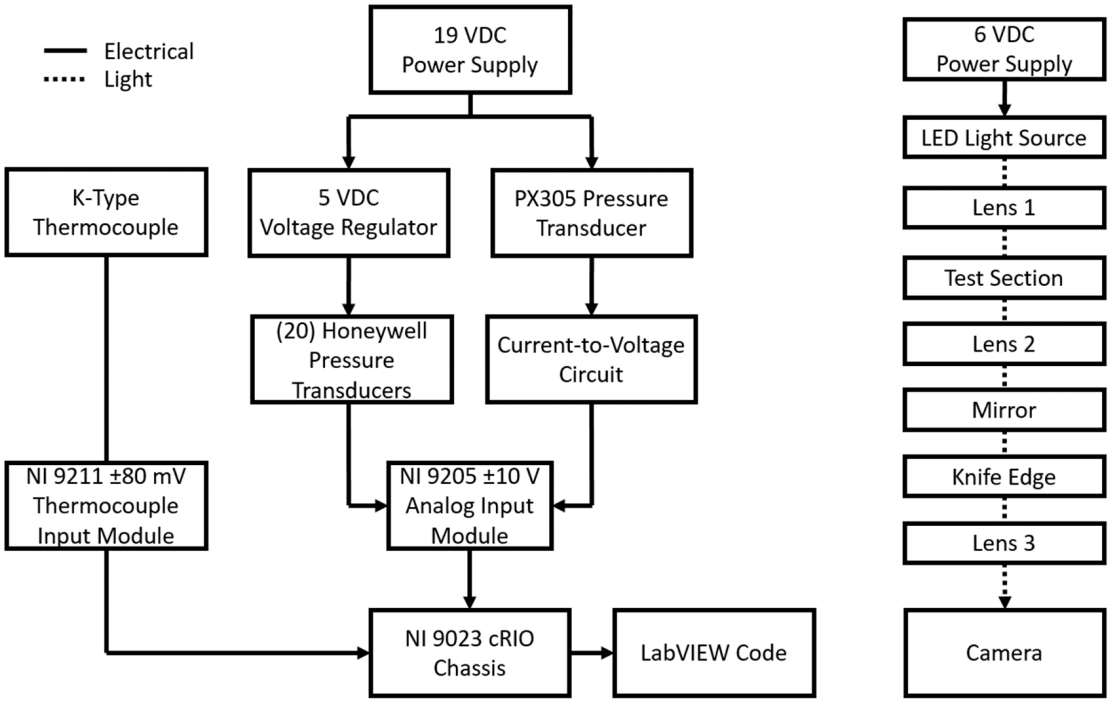

Figure 2.22: Electrical schematic.

Table 2.5: Transducer Specifications

Sensor	Range	Accuracy
K-Type Thermocouple	200 - 1250 $°C$	$\pm$ 2.2 $°C$
Honeywell SSCDANN100PAAB5	0 $-$ 100 psi (0 $-$ 689 kPa)	$\pm$ 0.25% FS
Honeywell SSCDRRN001PDAA5	$\pm$ 1 psi (6.89 kPa)	$\pm$ 0.25% FS
Omega PX305	0 $-$ 1000 psi (0 $-$ 6890 kPa)	$\pm$ 0.25% FS

Table 2.6: National Instruments Module Specifications

Module	Channels	Resolution	Range	Max Sampling Rate
9205 Analog Input	32	16 bit	$\pm$ 10 VDC	250,000 $\frac{S}{s}$
9211 Thermocouple Input	4	24 bit	$\pm$ 80 $mVDC$	14 $\frac{S}{s}$

The system is configured to power all of the transducers with a single 19 VDC power supply. However, while the Omega PX305 pressure transducer (used to measure tank pressure) receives all 19 VDC, the power supply voltage is regulated to 5 VDC for the Honeywell SSCDANN100PAAB5 pressure transducers (used for test section pressure measurements). All of the pressure transducer signals are measured using a National Instruments 9205 Analog Voltage In analog-to-digital conversion module. The thermocouple data was measured using a National Instruments NI 9211 analog-to-digital converter which includes cold junction compensation to account for additional Seebeck voltages. Each of these modules are installed in a National Instruments 9023 cRIO chassis to which the LabVIEW data acquisition code communicates.

2.5.2.1 Schlieren System

A dual-field lens type schlieren system was assembled and aligned to visualize the density gradients within the nozzle and visually measure the thrust-vector angle of the primary flow. Figure 2.23 presents a basic schematic of the schlieren system layout.

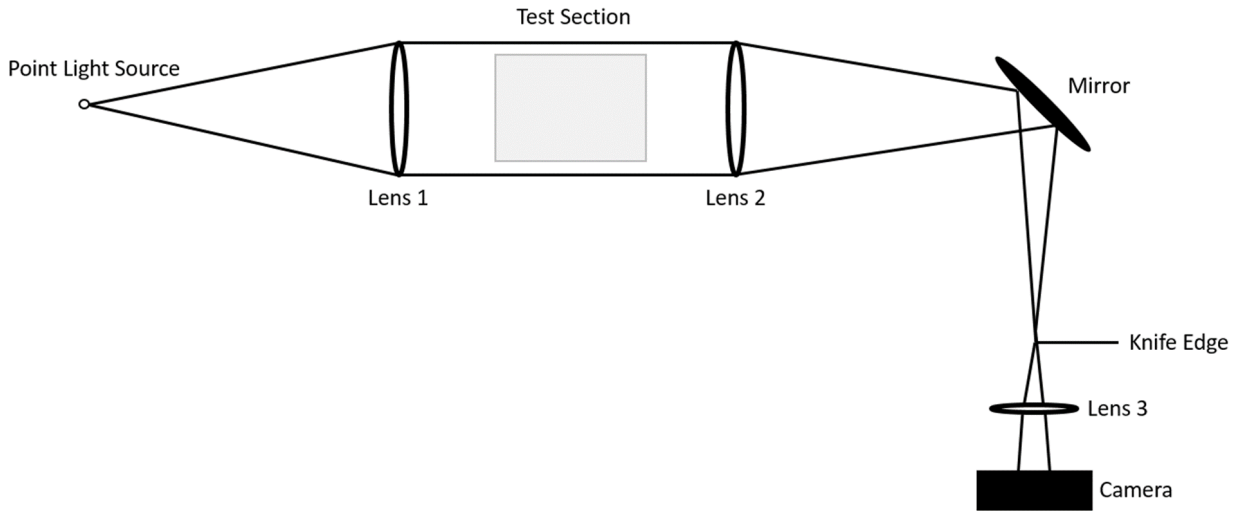

Figure 2.23: Schematic detailing the basic layout of the dual-field lens type schlieren system.

In this schlieren configuration, a lens is used to collimate the light from the light source and the second lens focuses the light to a focal point. Diffraction of the light due to density gradients changes the path of light and a knife edge blocks light passing through either positive or negative density gradients, depending on the knife edge orientation. The light source is a high power 3 watt single LED with an approximately 0.01 in (0.254 mm) diameter aperture. Manufacturing limitations and LED power constraints restricted any further reduction in the aperture diameter. Lenses 1 and 2 are uncoated achromatic doublet lenses that limit chromatic aberration across wavelengths. Lens 3, which is used to focus and magnify the image onto the camera image plane, is an uncoated plano-convex lens. In order to ensure the schlieren system could fit on the footprint of the test cart, a mirror was used to extend the effective length of the schlieren system. A 3 in (76.2 mm) diameter mirror is employed to ensure the image is not cropped. The lens specifications are listed in Table 2.7 and Table 2.8 lists the specifications of the mirror.

Table 2.7: Schlieren lens specifications

Lens No.	Diameter	Focal Length	Surface Quality	Centering Tolerance
1	76.2 mm	200 mm	60-40 (scratch-dig)	3-5 (arc-min)
2	76.2 mm	400 mm	60-40 (scratch-dig)	3-5 (arc-min)
3	25.4 mm	75 mm	40-20 (scratch-dig)	< 3 (arc-min)

Table 2.8: Schlieren mirror specifications

Diameter	Surface Flatness	Substrate	Coating	Wavelength	Coating Spec
76.2 mm	$\frac{\lambda}{10}$	Fused Silica	Enhanced Alum	$450 - 650$ nm	$> 95\%$

The knife edge used to obstruct the focal point is a safety razor blade mounted on a traverse which allows for fine adjustment of the knife edge in either a vertical or horizontal configuration. To determine the orientation in which the vector angle is most discernible, tests were performed with the knife edge in the vertical and horizontal configuration. Figure 2.24(a) shows the flow field with a vertical knife edge orientation while Figure 2.24(b) displays the same test case with the knife edge in the horizontal orientation. A comparison between the images indicates that the vector angle is more easily discernible using the horizontal orientation. This was expected since the exhaust flow shear layers, which parallel the exhaust flow, have high density gradients orthogonal to the direction of flow. Because the gradients were more easily identified with the horizontal knife edge, this approach was used for the rest of the study.

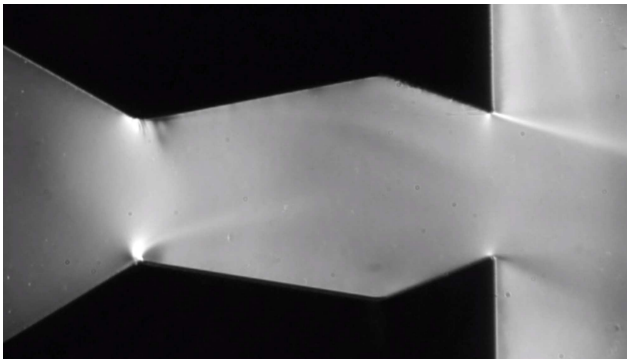

(a) Vertical

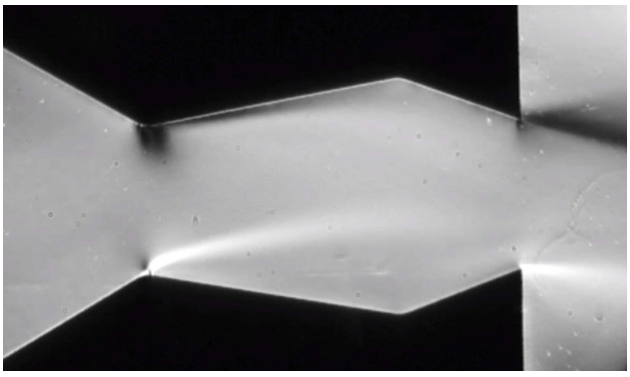

(b) Horizontal

Figure 2.24: Comparison of Schlieren Knife Edge Orientation

The camera used for recording of the schlieren images was a Sony Alpha NEX-C3. The specifications and settings used during testing are shown in Table 2.9.

Table 2.9: Camera specifications

Resolution.	Frame Rate	Sensor Type	Sensor Dim	ISO
0.92 MP	30 Hz	APS HD, CMOS	15.6 x 23.5 (mm)	200

2.6 Experimental Procedure

The SWIFT system was typically operated by one person and took on average 5 minutes to run per test case. After powering the data acquisition system, a typical test was initiated by first filling the main tank with nitrogen gas up to a target pressure of 400 psi (2758 kPa). This was performed using a set of 2200 psi (15168 kPa) K type gas cylinders and a pressure regulator. Tank pressure is monitored using the tank mounted pressure transducer and the LabVIEW data acquisition software/hardware. Once 400 psi (2758 kPa) is reached, the supply valves are closed. Due to cooling of the main tank, however, the pressure drops and the supply valves can be reopened after about 5 minutes to raise the pressure back to 400 psi (2758 kPa). To initiate a test, the core flow regulator is first adjusted to approximately 5 psi (34.5 kPa) over the desired set point. This bias is required in order to offset the drop in set point that is seen once a demand is supplied to the regulator. The secondary injection flow, if applicable, is then initiated first in order to allow the mass flow controller to reach steady state. This is done by adjusting the injection system regulator to approximately 140 psi (827 kPa) and setting the mass flow controller to the desired mass flow rate. After the secondary flow has reached steady state, the core flow ball valve is opened quickly, with a transient time of approximately 0.25 seconds. The diffuser total pressure is then monitored in real time while manual adjustments are made to regulator to maintain total pressure within bounds. After approximately 3 seconds of steady state operation, the core flow ball valve is closed and the secondary flow regulator is decreased to ambient pressure. After completion of a single

3 second test, the tank pressure is typically only reduced by about 100 psi (689 kPa). However, since the Marsh Bellofram Type 78 regulator is better able to maintain its total pressure setpoint at high inlet pressures, the main tank is refilled to 400 psi (2758 kPa) after each test.

2.7 Key Measurements

The data collected by the instrumentation on the SWIFT system allowed for a relatively extensive analysis of the flow conditions. The following quantities of interest were derived either directly or indirectly from the data collected in the wind tunnel.

1. Wall pressure ratio
2. Injection Percentage
3. Nozzle Pressure Ratio (NPR)
4. Thrust-Vector Angle
5. Thrust Vector Efficiency

2.7.1 Wall Pressure Ratio

The wall pressure ratio is a derived quantity which is defined to be the ratio between the wall static pressure and the total pressure. This quantity is used to compare wall pressure profiles in order to compensate for changes in the NPR ratio. This quantity is shown in Equation 2.2.

$$Wall\ Pressure\ Ratio = \frac{P}{P_T} \tag{2.2}$$

The quantities used in Equation 2.2 are both values directly measured in the flow field and require the calculation of no additional derived quantities.

2.7.2 Injection Percentage

Injection percentage is another important parameter that allows for a relationship between injection mass flow rate and thrust angle to be determined. More specifically, injection percentage is a quantity that relates the amount of secondary injection mass flow rate to the overall system mass flow rate. Equation 2.3 defines this quantity.

$$IP = \frac{\dot{m}_i}{\dot{m}_i \ + \ \dot{m}_p} \tag{2.3}$$

2.7.3 Primary Mass Flow Rate

In the calculation of injection percentage, however, only injection mass flow rate is a direct measurement which is obtained through the output of a calibrated mass flow meter. Primary mass flow rate is a derived quantity obtained through the use of a venturi static pressure differential. Using a combination of Bernoulli's principle, conservation of mass, and the ideal gas law, the mass flow rate can be calculated. The following section details this derivation.

$$\dot{m}_p = \rho \cdot A_1 \cdot V_1 = \rho \cdot A_2 \cdot V_2 \tag{2.4}$$

$$\frac{1}{2}\rho V_1^2 + P_1 = \frac{1}{2}\rho V_2^2 + P_2 \tag{2.5}$$

Equation 2.4 is first solved for V_1 as shown in Equation 2.6.

$$V_1 = \frac{V_2 A_2}{A_1} \tag{2.6}$$

Equation 2.6 is then plugged into Equation 2.5 as shown in Equation 2.7.

$$\frac{1}{2}\rho V_2^2 (\frac{A_2}{A_1})^2 + P_1 = \frac{1}{2}\rho V_2^2 + P_2 \tag{2.7}$$

After simplification, Equation 2.8 is derived to calculate the velocity V_2 in terms of the pressure differential, area differential, and gas static density.

$$V_2 = \sqrt{\frac{2(P_1 - P2)}{\rho(1 - (\frac{A_2}{A_1})^2}} \tag{2.8}$$

The mass flow rate can then be calculated using Equation 2.4 where the static density is calculated using the ideal gas law shown in Equation 2.9.

$$\rho = \frac{P}{RT} \tag{2.9}$$

2.7.4 Nozzle Pressure Ratio

Nozzle Pressure Ratio (NPR) is a parameter used to describe the ratio between the ambient environmental pressure and the flow total pressure. The main assumption when calculating the NPR is that there is no total pressure loss between the instrumentation section of the diffuser and the nozzle test insert. Ambient pressure for this quantity is determined by measuring the vented total/static pressure within the test section prior to a test. Equation 2.10 shows the equation used for calculating NPR.

$$NPR = \frac{P_T}{P_{Amb}} \tag{2.10}$$

2.7.5 Thrust-Vector Angle

The system used for this testing was not instrumented with force gages so the vector angle was measured using schlieren photographs taken during each test. To measure this, the angle of the density gradient at the upper wall exit is averaged with the angle of the density gradient on the lower wall. This method aims to nullify any bias introduced due to an expansion of an underexpanded flow. Figure 2.25 illustrates the angles used to calculate the thrust-vector angle.

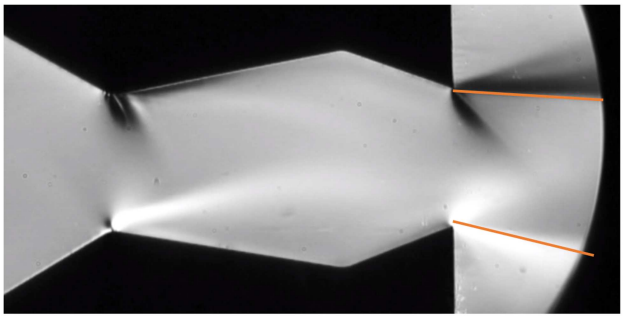

Figure 2.25: Method for measuring vector angle.

In order to corroborate the thrust-vector angle derived from the schlieren, a second method was also developed to derive the thrust-vector angle using the pressure profile. This derived angle approximates the total thrust being generated by the nozzle using the standard thrust equation and then calculates an angle based on the calculated net force in the vertical y direction. Equation 2.11 shows the calculation of total thrust.

$$Total\ Thrust = (\dot{m}_p + \dot{m}_i)V + (P_e - P_a mb)A_e \tag{2.11}$$

The net vertical y component of the thrust is calculated by integrating the pressure along the upper and lower nozzle wall as shown in Equation 2.12.

$$Thrust_y = z_w(\int_1^8 P_{upper}\ dx\ -\ \int_1^8 P_{lower}\ dx) \tag{2.12}$$

The thrust-vector angle is then calculated using Equation 2.13

$$\delta = sin^{-1}\frac{Thrust_y}{Total\ Thrust} \tag{2.13}$$

2.7.6 Vector Efficiency

The parameter vector efficiency is calculated using the ratio of the thrust-vector angle and injection percentage. This value characterizes how effective a nozzle is at vectoring the flow under various flow and geometric configurations. Equation 2.14 details the calculation of his parameter.

$$Vector\ Efficiency = \frac{\delta_a}{IP} \tag{2.14}$$

2.7.7 Measurement Uncertainty

In order to account for variability in the pressure, temperature, and derived quantities, an error analysis was conducted. While uncertainty in the direct measurements is simply a combination of the manufacturers stated error and statistical uncertainty, the uncertainty in the derived quantities is a function of the sensitivity of each of the values used to calculate it.

2.7.7.1 Direct Measurement Uncertainty

The method used to calculated uncertainty for direct measurements is shown below.

$$Uncertainty = \sqrt{b^2 + p^2} \tag{2.15}$$

$$b = \sqrt{\sum_{k=1}^{K} b_k^2} \tag{2.16}$$

$$p = \frac{2\sigma}{sqrtN} \tag{2.17}$$

Uncertainty is a combination of bias and precision limit. The bias limit, Equation 2.16, comes from sources such as transducer accuracy while precision limit, Equation 2.17, is based on variance of the mean for a measurement that is averaged from a number of samples.

2.7.7.2 Derived Measurement Uncertainty

Derived measurement uncertainty is based largely on the sensitivity of each term. The bias and precision limit for derived quantities is shown below.

$$b_y = \sqrt{\sum_{m=1}^{M} (\frac{\partial y}{\partial x_m} b_{x_m})^2} \tag{2.18}$$

$$p_y = \sqrt{\sum_{m=1}^{M} (\frac{\partial y}{\partial x_m} p_{x_m})^2} \tag{2.19}$$

Chapter 3

Results

3.1 Tunnel Characterization

Initial testing of the SWIFT system was conducted in order to characterize any inherent biases in the system as well as to determine the performance of the pneumatic system. This initial testing used symmetric test inserts with pressure taps located as defined in Table 2.4, but without any injection geometry. These baseline tests were conducted at a NPR of 2 and 4 with two tests being conducted at each pressure ratio. An illustration of the nozzle insert configuration is shown in Figure 3.1.

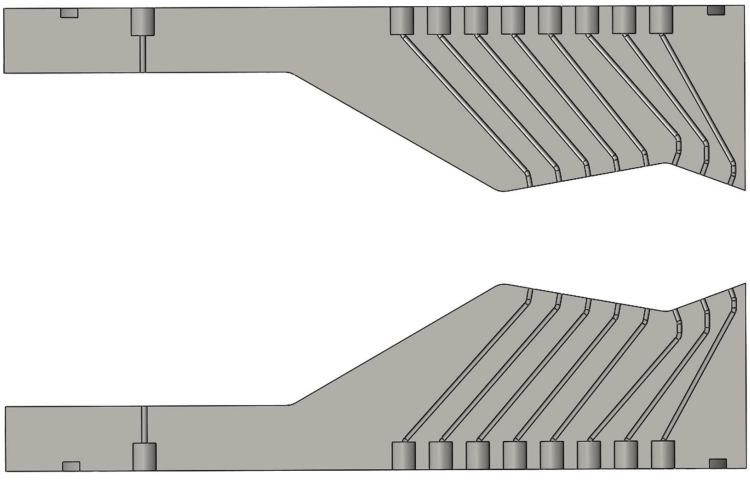

Figure 3.1: Configuration of test with plain inserts.

Data collected from each test consists of an average of the steady state data and tests for each configuration were run for at least three seconds after diffuser total pressure reached its steady state value. Natural variations in the flow conditions were found to exist because of the variability in the pressure regulator over the course of the test. However, these variations were relatively minor and average total pressures between tests matched closely. An example of the diffuser total pressure time series over the course of three different tests is shown in Figure 3.2.

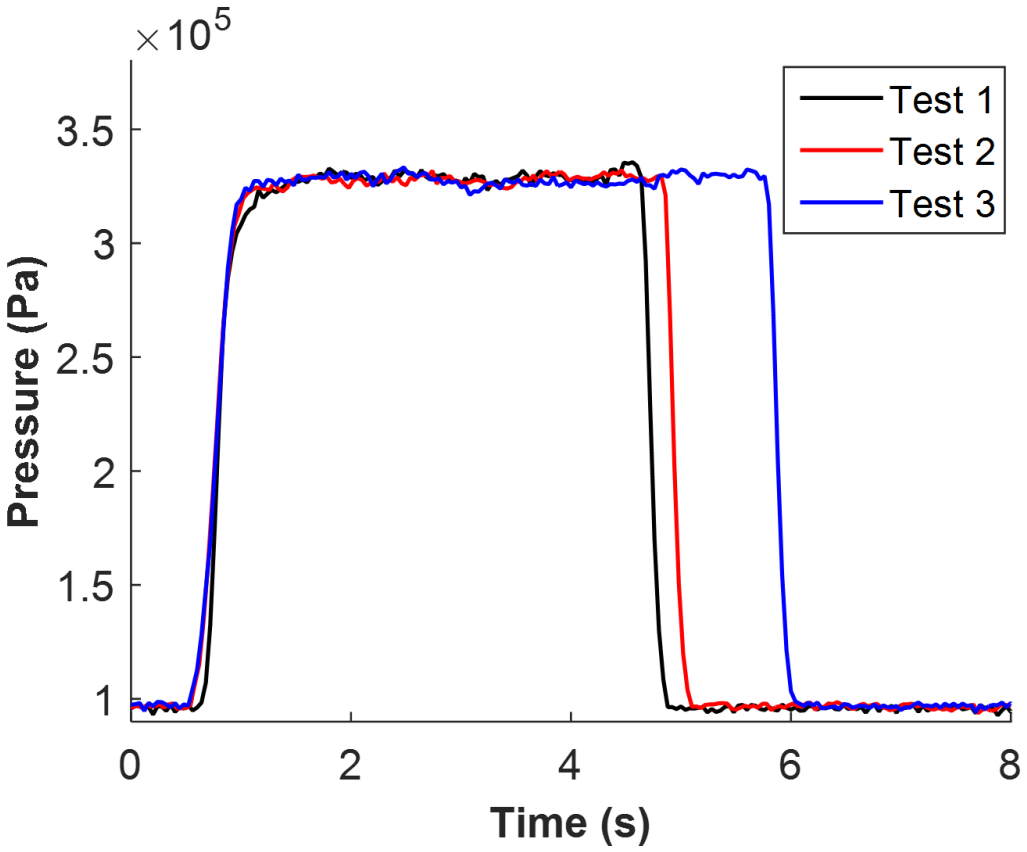

Figure 3.2: Typical total pressure time series.

The total pressure is in close agreement between each of the test cases, however the testing times varied widely between these cases since the primary flow ball valve was manually actuated. This has negligable impact on the data though since the tests reached steady state in less than 0.5 s.

A similar consistency was observed for primary mass flow rate, which is a quantity derived from the differential pressure between the settling chamber and test section, but varies primarily based on variations in the total pressure. Figure 3.3 shows a time history of core mass flow rate for the same three tests.

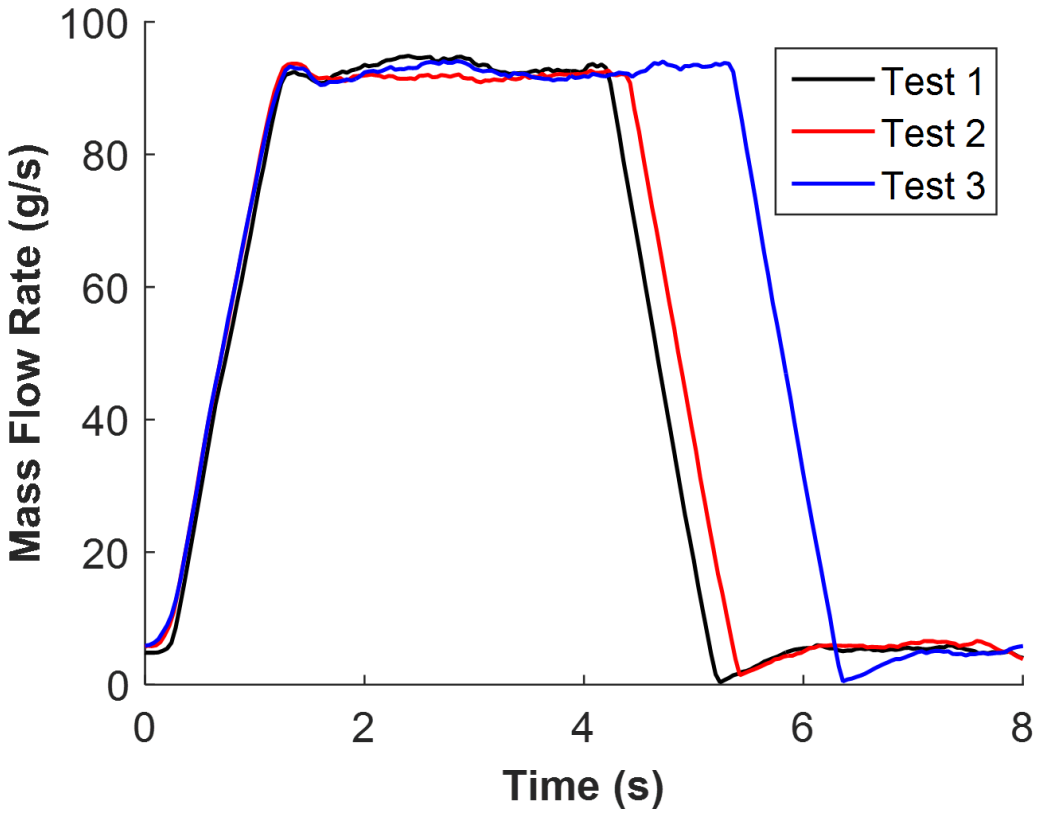

Figure 3.3: Typical mass flow rate time series.

The most notable qualitative difference between the total pressure and mass flow time series is the longer transient time at the start and end of each test. This is due to an intentional bias in the pressure tap volume between the diffuser static pressure tap and the pressure transducer. In order to avoid a pressure differential spike in the system as a result of a quick startup, an additional length of tubing was added between the higher pressure diffuser pressure tap and the differential pressure transducer which increased the volume thus dampening the time response. Because of

this, when the flow is terminated, the high pressure diffuser pressure tap takes longer to drain to atmospheric conditions and biases the differential pressure negatively. Variability at steady state, however, shows minor oscillations during the test with the maximum variability on the order of 1.5% of the mean.

One of the more important measurements is the wall pressure profile along the surface of the nozzle test inserts. An example of the wall static pressure time series for a test is shown in Figure 3.4.

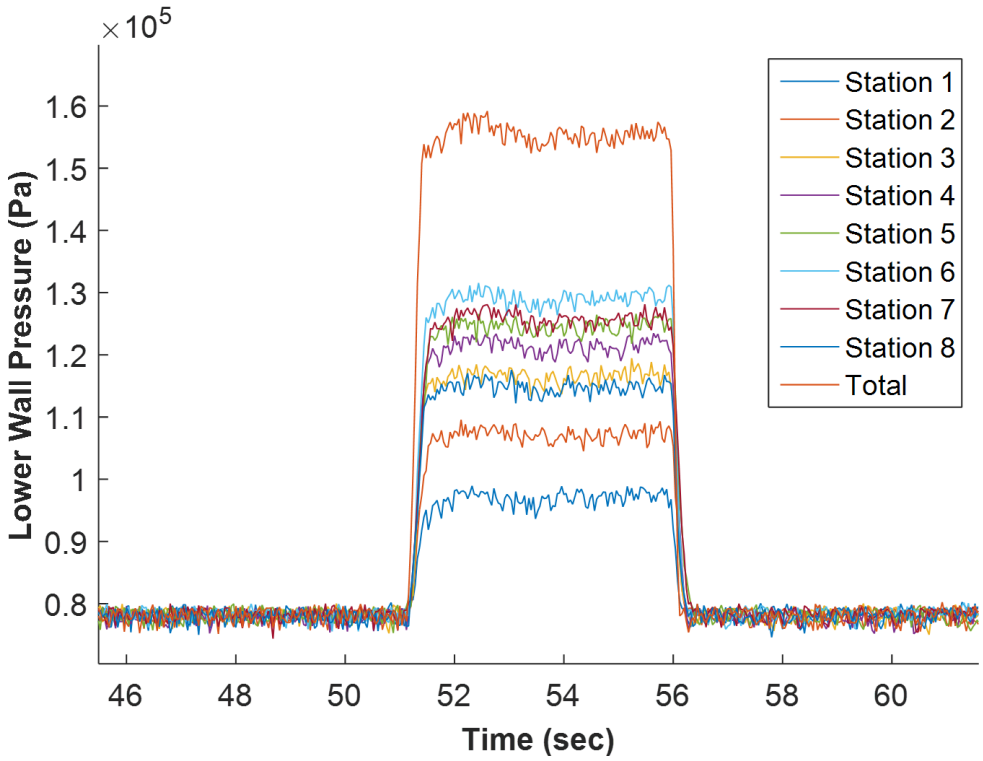

Figure 3.4: Typical pressure tap time series.

Each station corresponds to the stations defined in Table 2.4 with the total pressure added for reference. Variability in each of the pressures is apparent with a slight low frequency oscillation seen during the beginning of the test. These low amplitude oscillations are acceptable since all of the wall pressures are ultimately non-dimensionalized using the total pressure which follows the

same oscillatory trend.

To ensure uniform flow was entering the test section, the pressure profiles from the plain top and bottom inserts were analyzed. Figure 3.5 shows the average pressure profile of four tests for a NPR of 2.

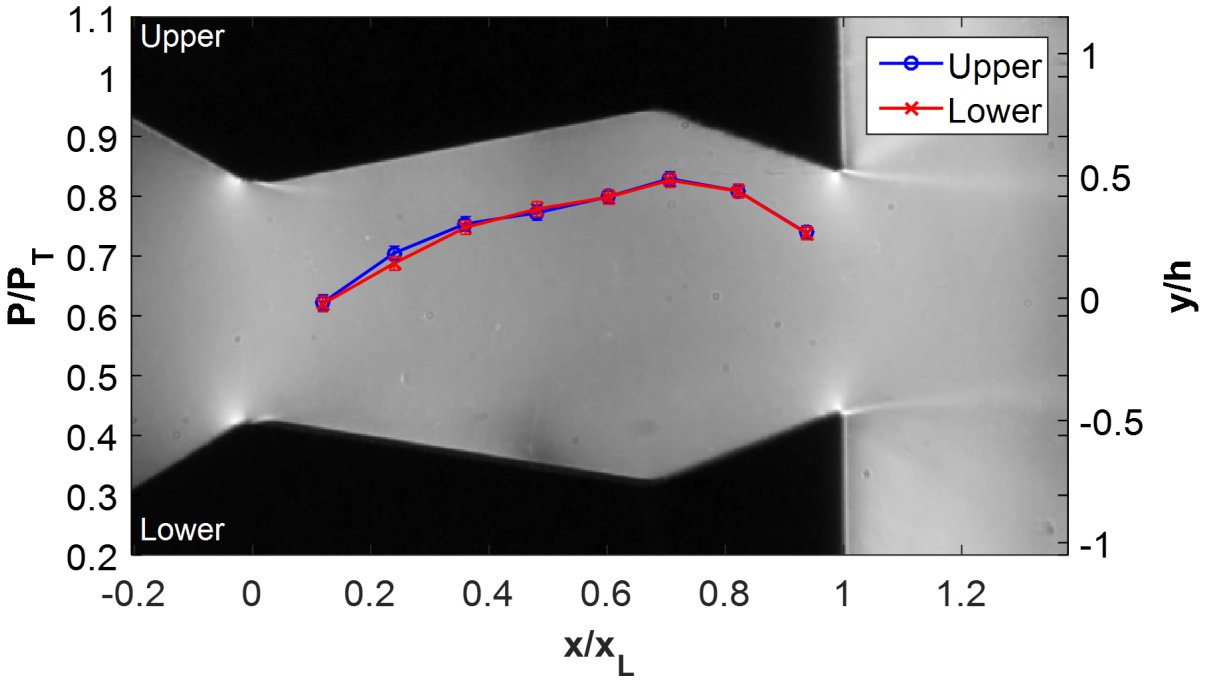

Figure 3.5: Plain wall pressure profiles at NPR = 2.

As expected, the pressure at each location along the nozzle is very similar for the symmetric nozzle configuration. The pressure at each point on the upper and lower walls is within the error bounds of each other which indicates that the flow into the test section is uniformly entering the nozzle geometry within the error of the data acquisition system. In addition to inlet flow symmetry, another concern was the lateral placement of each nozzle test insert. Any bias in the placement of one insert with respect to the other would be expected to show a bias in the pressure profile. The symmetry of the pressure profiles also verifies that there is no bias in the installation of the inserts. Figure 3.6 shows a similar symmetric result when conducted at a NPR of 4. The upper and lower

pressure profile are matched along the length of the nozzle indicating uniform test section flow and unbiased placement of the inserts.

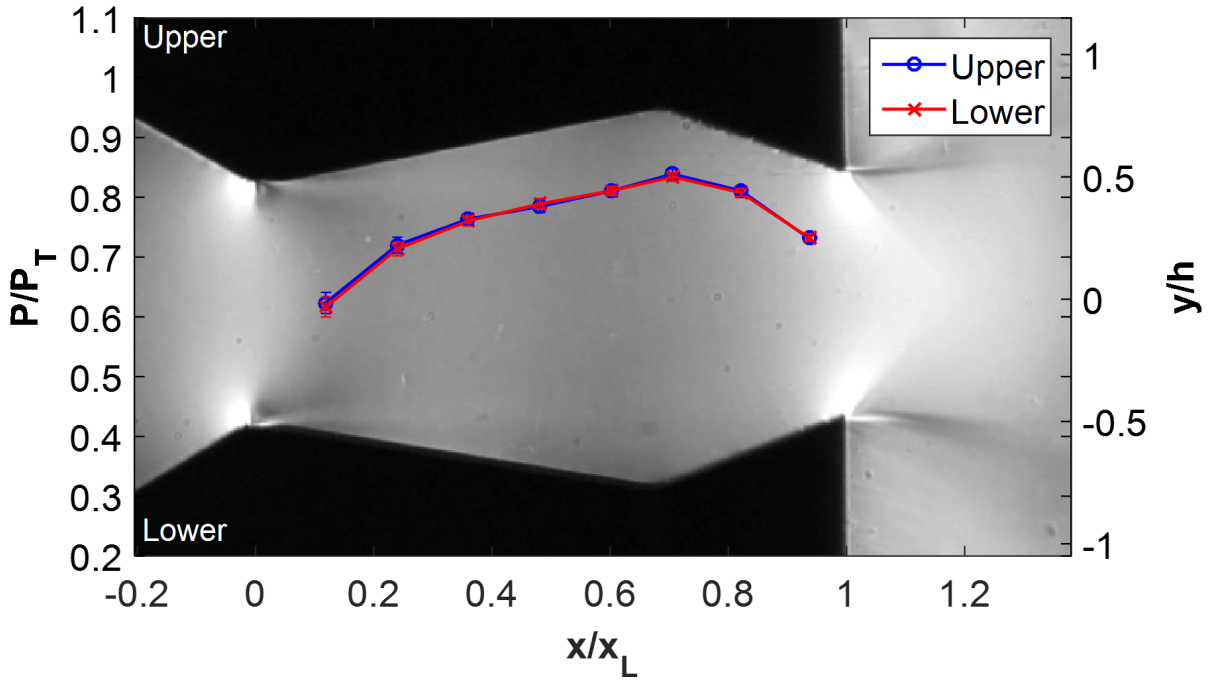

Figure 3.6: Plain wall pressure profiles at NPR = 4.

This result is also corroborated by schlieren which was taken during these tests. For these tests in particular, the schlieren system knife edge is oriented in the vertical direction in order to generate an image that would show symmetric grayscale pixel intensities about the horizontal axis. One such image, shown in Figure 3.7 (b), shows a symmetric expansion fan and exhaust shear layer indicating that the flow is unbiased. To quantify this, the average grayscale pixel intensity of the flow exiting the nozzle is plotted. This grayscale profile shows a symmetric intensity across the height of the nozzle exit and corroborates the pressure profile results. The profile along with the box used to generate this average is shown in Figure 3.7.

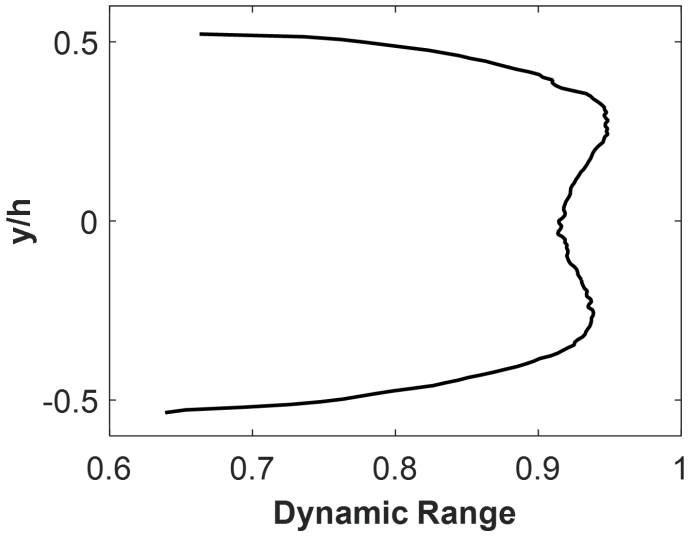

(a) Dynamic Range

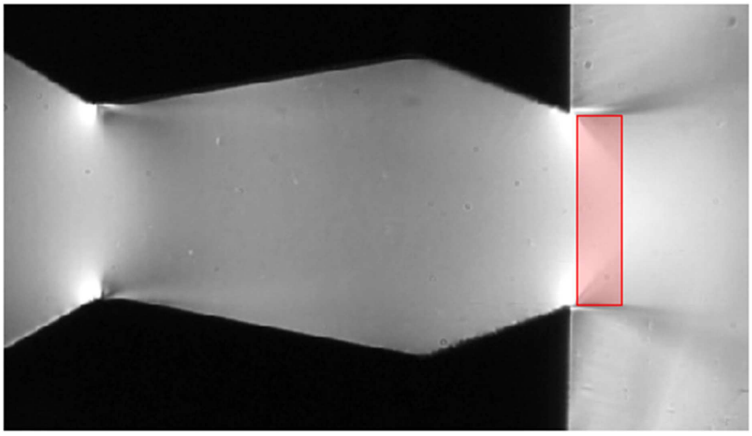

(b) Region Used for Symmetry Evaluation

Figure 3.7: Flow symmetry check using schlieren and camera dynamic range.

A similar CFD case was simulated examining the wall pressure profiles without secondary injection geometry in order to gauge how representative the simulations are of the experiment. The CFD and the experimental results show a relatively good agreement with the exception of the first two pressure tap locations. This large difference close to the first throat suggests that simulation predicts less flow separation at the throat than the experiment shows. The inability for the K-epsilon turbulence closure model to accurately model flow separation is a known weakness

due to its reliance on a wall function at the near-wall regions. Figure 3.8 shows the wall pressure profile of the experiment and CFD at a NPR of 2.

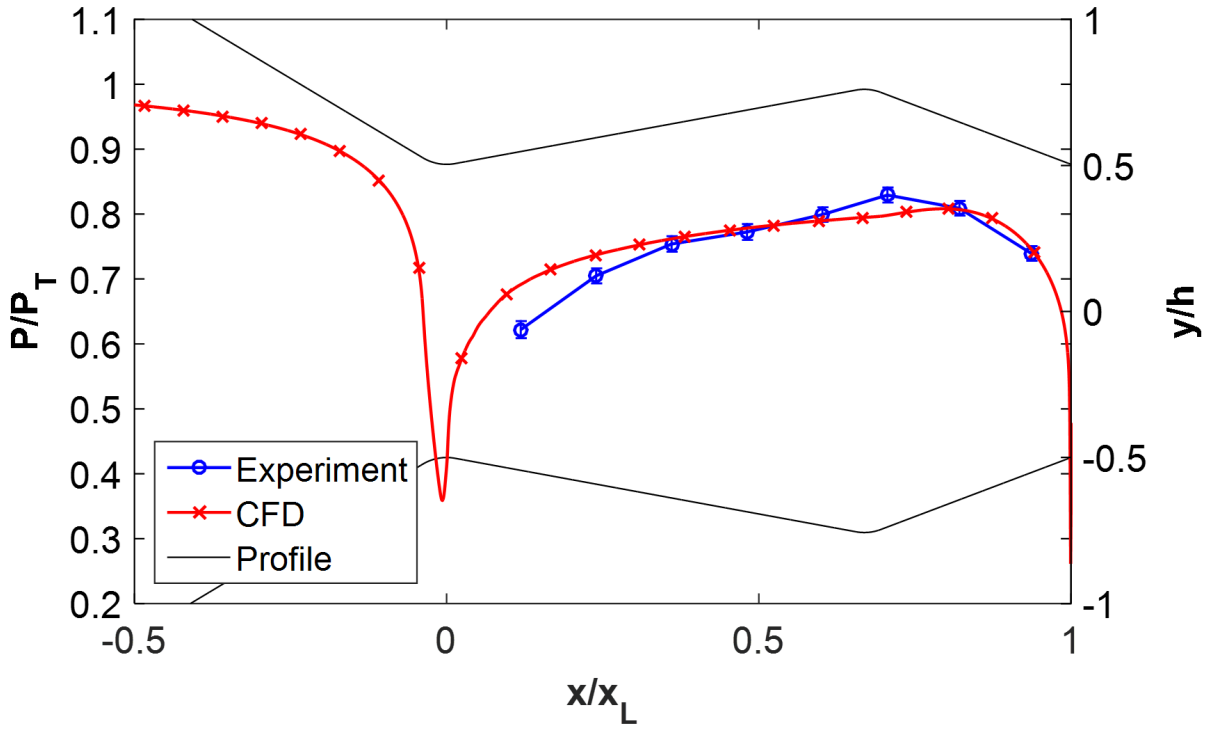

Figure 3.8: Comparison of CFD to experiment with plain inserts at NPR = 2.

3.2 Secondary Injection Characterization

With the baseline performance of the system quantified, tests with secondary injection geometry and mass injection were investigated. Conducting tests with this secondary injection added the additional parameter of secondary injection mass flow rate which was controlled using the mass flow controller. Figure 3.9 shows a standard time series of the secondary injection mass flow rate.

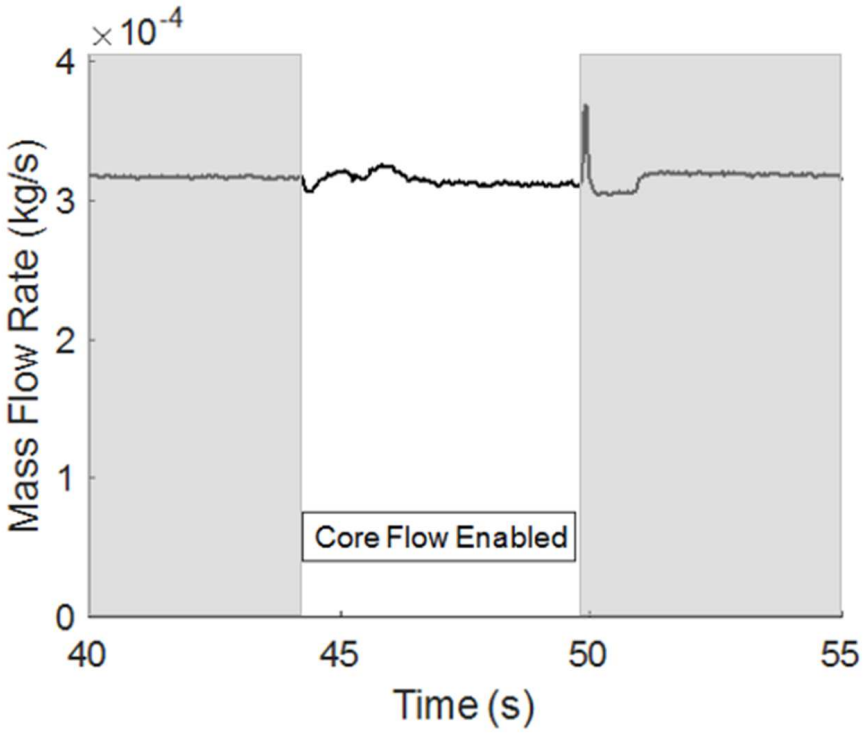

Figure 3.9: Secondary injection mass flow rate time series with unchoked injection.

The gray areas indicate the times which the core flow is off and the white area is the time during which the primary flow is on. In general, secondary injection mass flow rate is relatively stable without primary flow as seen between 40 and 44 seconds. When the primary flow is introduced, however, oscillations are generated due to the response of the controller in compensating for backpressure from the primary flow. Similarly, when primary flow is terminated, a large spike in the secondary mass flow rate is generated due to a sudden decrease in this backpressure. The largest oscillations at the beginning of the test are on the order of 3% of the average value and dampen out within three seconds of the start of the test. To reduce this feedback, the total pressure ratio of the secondary to primary flow can be increased to a point high enough such that the flow is choked at some point between the mass flow controller and the secondary injection port in the test-section. At higher mass flow rates, this choked flow condition is possible and Figure 3.10 shows an example of a secondary injection mass flow rate time series of this.

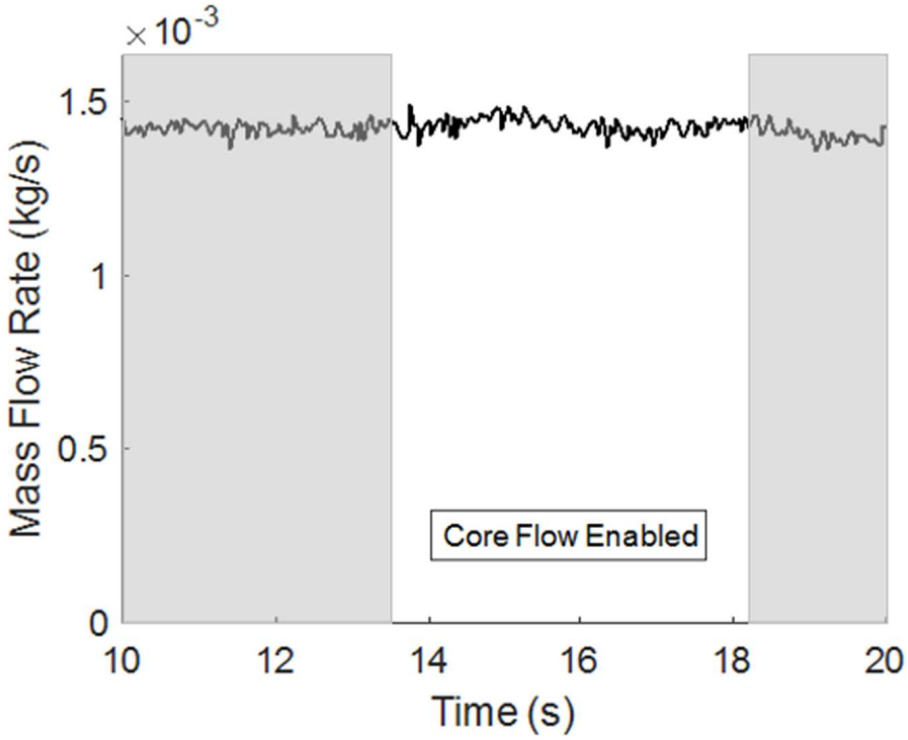

Figure 3.10: Secondary injection mass flow rate time series with choked injection.

It is clear that with this higher mass flow rate, the oscillations in the secondary injection mass flow rate are much lower. For this particular test, the injection total pressure was 4.5 times the primary flow total pressure, which ensured choked flow at the location of minimum effective area. However, since the flow profile within the secondary injection geometry is expected to have a Poiseuille-like velocity profile, there will be areas of local subsonic flow. These subsonic areas allow for communication between the core flow and the secondary flow and likely is the reason for the minor lower frequency fluctuations that are seen.

3.3 Secondary Injection Baseline Tests

For each injection configuration, baseline tests were conducted in order to determine the effect injection geometry had on the thrust-vector angle and pressure profiles without any secondary injection. Since each test had one insert with injection geometry, and one insert without, a bias was expected due to the geometric asymmetry at the upstream throat. This configuration is shown in Figure 3.11.

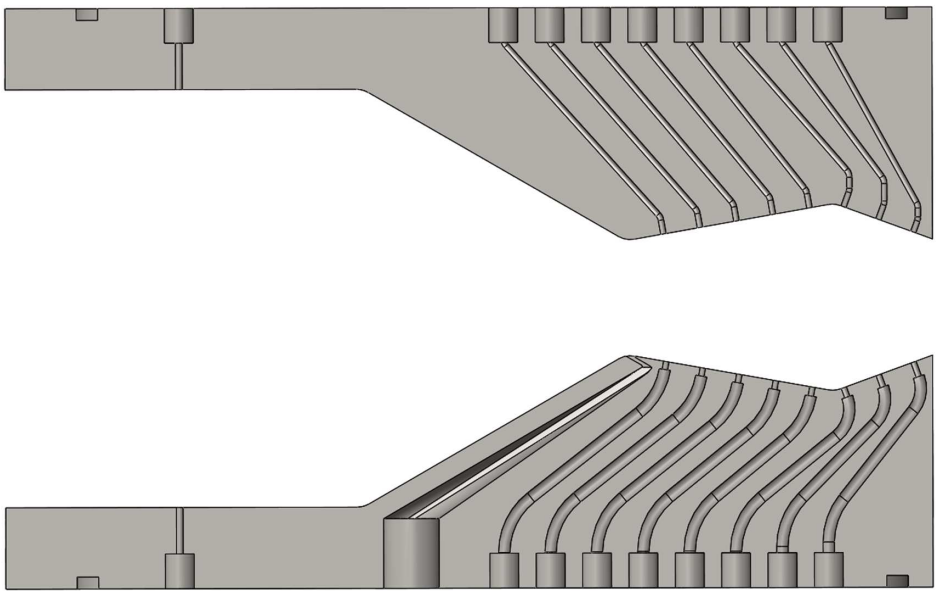

Figure 3.11: Standard secondary injection test insert configuration.

The main reason this configuration was used as opposed to symmetric nozzle inserts was to reduce the manufacturing and cost implications of requiring two nozzle inserts for each configuration instead of the one nozzle insert required using this configuration. Table 3.1 shows the configurations used for each of the three tests.

Beginning with case 1.*A*.2, Figure 3.12 shows the pressure ratio profile for the upper plain and lower injection walls.

Table 3.1: Secondary Injection Baseline Test Cases

Case	Lower Test Insert	Upper Test Insert	Injection Percentage (IP)	NPR
1.A.2	V1	Plain	0%	2
1.A.4	V1	Plain	0%	4
2.A.2	V2	Plain	0%	2
2.A.4	V2	Plain	0%	4
3.A.2	V3	Plain	0%	2
3.A.4	V3	Plain	0%	4

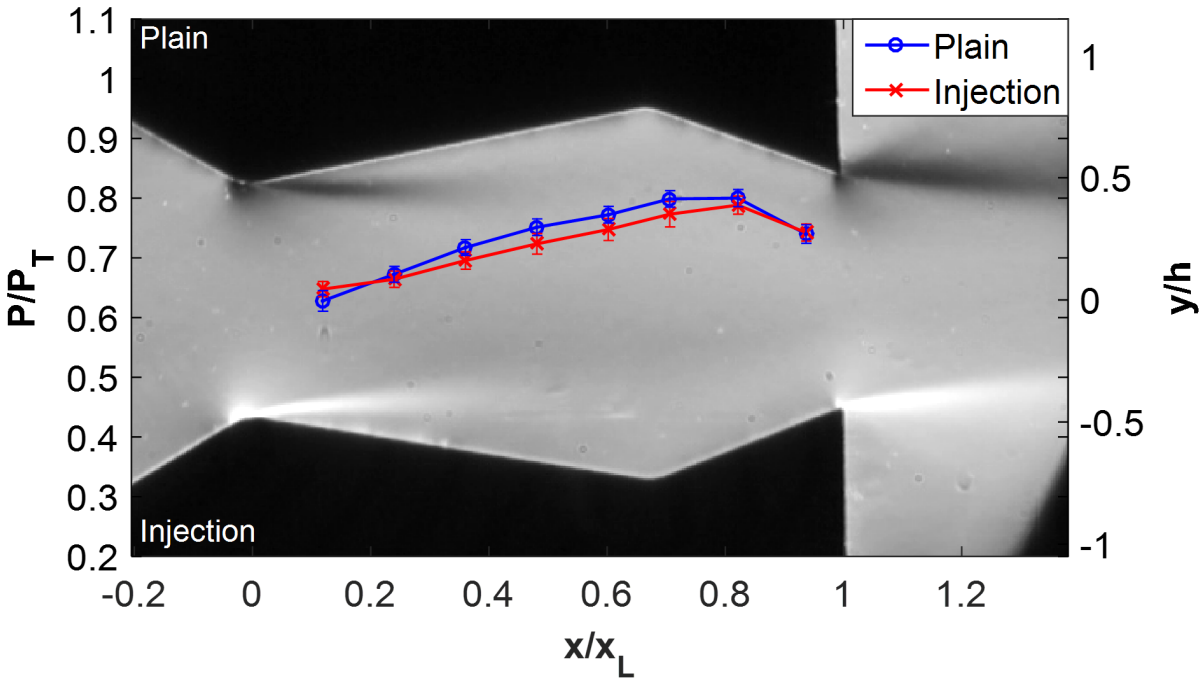

Figure 3.12: Case 1.A.2 schlieren and with associated pressure profile.

A clear bias is apparent where the pressure profile along the surface of the test insert with injection geometry is shifted slightly lower than the pressure profile along the plain insert. The pressure profile on the plain insert is as expected with an increase in the pressure ratio as the nozzle walls diverge. The pressure profile of the injection insert, however, suggests there is additional boundary layer separation. The more gradual increase in pressure between the first and second pressure tap indicates that the velocity of the flow near the wall is similar at these two points and suggests that the flow has detached. This concept can be more clearly seen in CFD data. A contour plot of the velocity calculated from CFD for case 1.*A*.2 is shown in Figure 3.13.

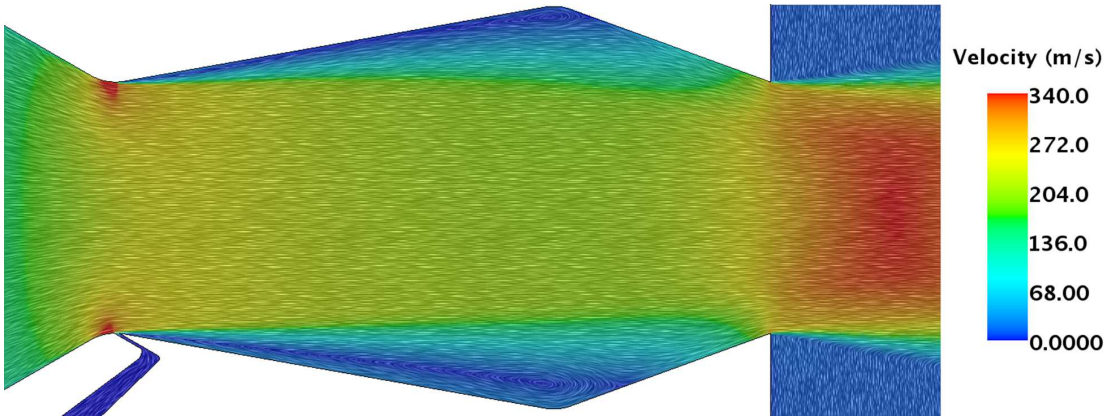

Figure 3.13: Case 1.A.2 CFD velocity contour plot.

The two separation regions can be clearly seen on the two diverging walls as the dark blue contours where the larger circulation region on the secondary injection wall indicates additional separation. The pressure profile derived from the CFD also present similar trends. Figure 3.14 below shows the wall pressure profiles from the CFD for case 1.*A*.2.

Similar to the experimental results, the pressure ratio of the lower wall is higher at the first throat but increases less along the profile compared to the upper plain wall. Figure 3.15 shows what the profile would look like if the CFD pressures were sampled at the same locations as the pressure taps in the experimental setup.

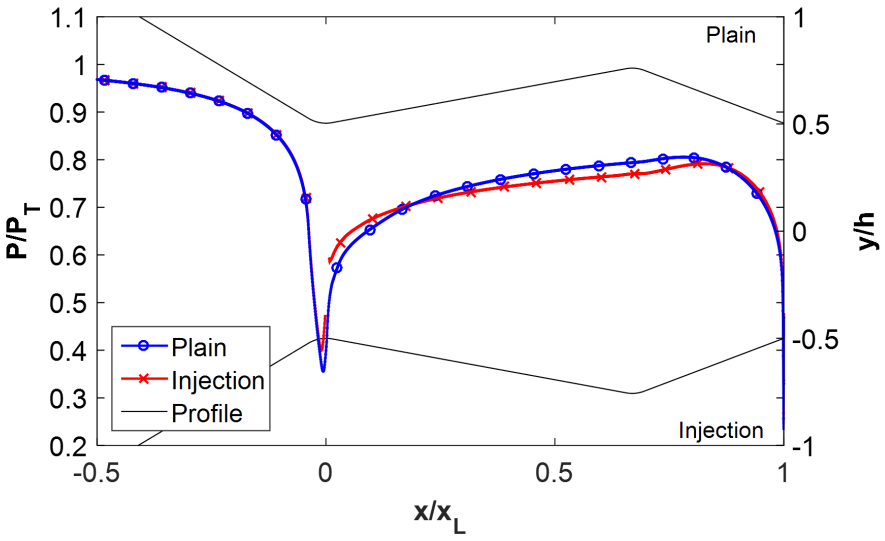

Figure 3.14: Case 1.A.2 CFD wall pressure profile.

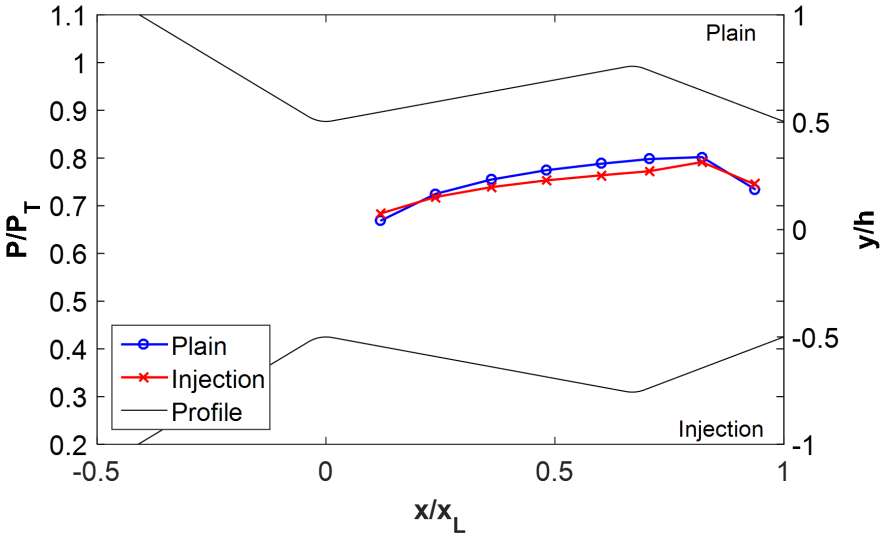

Figure 3.15: Case 1.A.2 CFD wall pressure sampled at experimental pressure tap locations.

It is apparent from this plot that the locations of the pressure taps is severely under-sampled near the throats. A direct comparison of the CFD and experimental results sampled at the same locations, however, show similar trends. Figure 3.16 shows the upper and lower wall profiles for the experimental and CFD results.

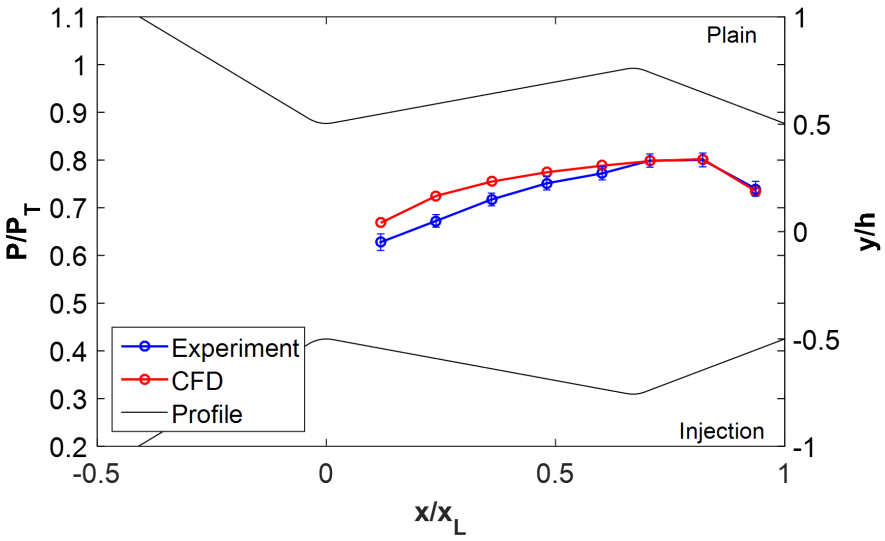

(a) Upper Wall Pressure Profile

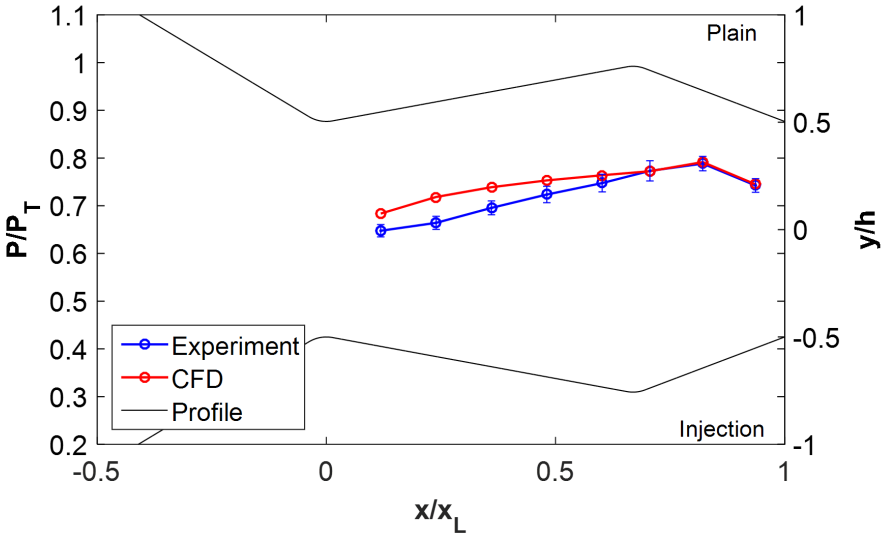

(b) Lower Wall Pressure Profile

Figure 3.16: Case 1.A.2 comparison between experimental and CFD pressure profile.

For both the upper and lower configurations, the CFD predicts less flow separation at the throat than the experiment shows. However, the experimental and CFD pressure ratio profiles match very well at the converging portion of the nozzle.

For a NPR of 4, the bias between the secondary injection and plain walls is greatly reduced. Figure 3.17 shows the pressure ratio profiles for case 1.*A*.4.

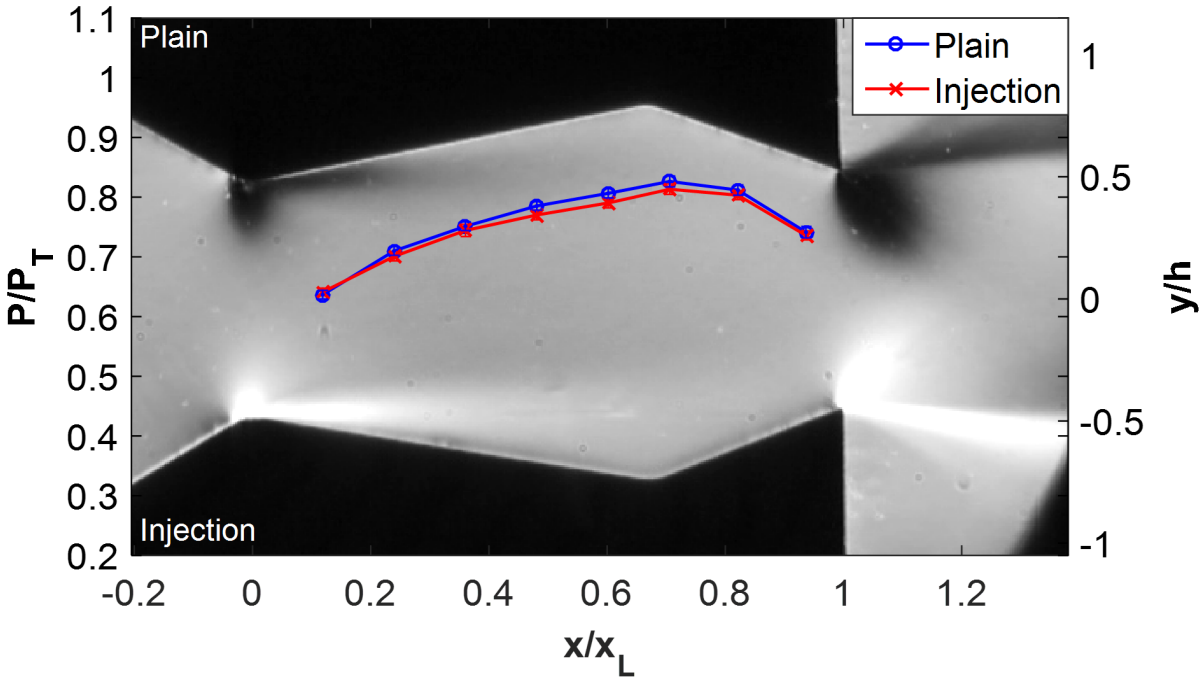

Figure 3.17: Case 1.A.4 schlieren and pressure profile.

The likely reason the secondary injection and plain wall pressure ratio profiles match better at a higher pressure ratio is because the Reynolds number doubles between a NPR of 2 and 4. The higher relative inertial forces that accompany higher Reynolds number flows likely dominate the flow separation that occurs at the first throat. This theory is corroborated by CFD results of case 1.*A*.4 flow conditions. A contour plot with a vector field of this is shown in Figure 3.18.

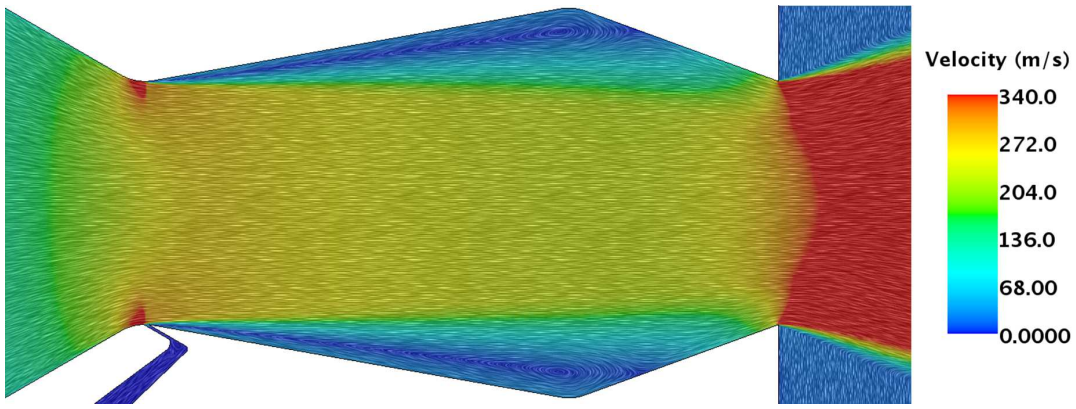

Figure 3.18: Case 1.A.4 CFD velocity contour plot.

In this vector field the separation regions are very apparent on both the secondary injection wall and plain wall. Additionally, the separation regions are about the same size indicating that the location and strength of the separation is the similar on both walls. Figure 3.19 shows the pressure ratio profile for the CFD.

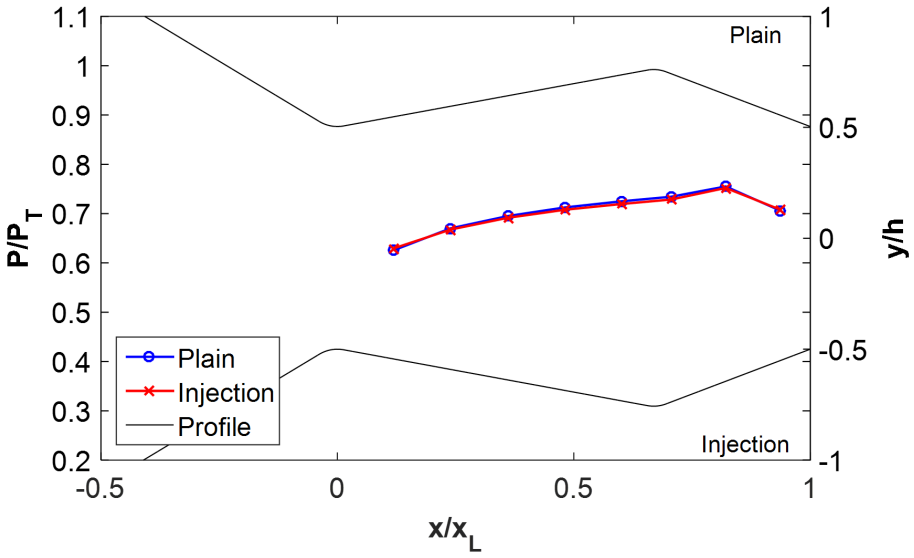

Figure 3.19: Case 1.A.4 CFD wall pressure sampled at experimental pressure tap locations

Similar to the experiment, the pressure profiles for the secondary injection and plain walls are almost identical. However, there is much less agreement between the experiment and CFD with the NPR of 4 flow. Figure 3.20 shows the pressure profile along the plain wall.

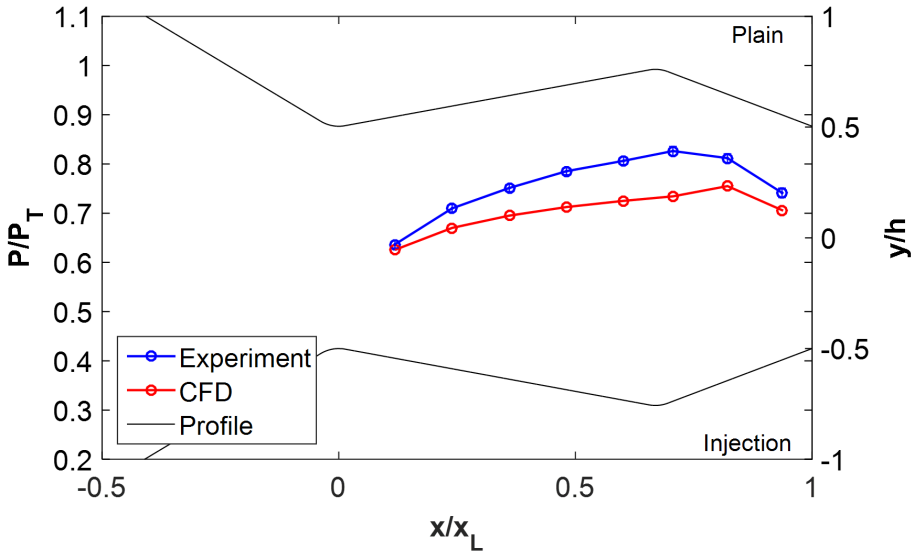

(a) Upper Wall Pressure Profile

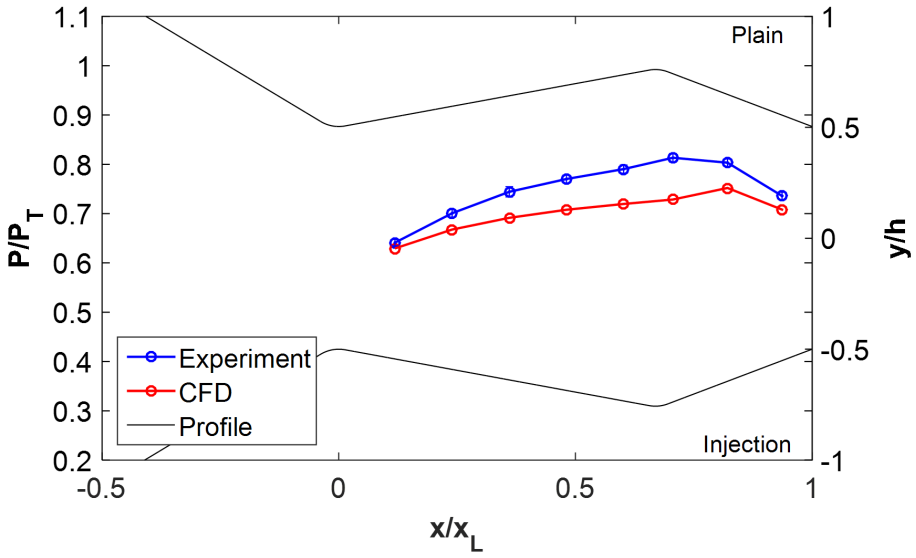

(b) Lower Wall Pressure Profile

Figure 3.20: Case 1.A.4 comparison between experimental and CFD pressure profile.

Unlike with a NPR of 2 in which the CFD did not predict the flow separation that was seen in the experiment, the CFD predicts additional flow separation with a NPR of 4. The reason for this inconsistency is not known, but is expected to be due to inaccurate separation prediction from the K-Epsilon's use of a wall function.

Since case 1.*A*.2 has the thinnest secondary injection geometry of all of the configurations, the impact of the secondary injections geometry was expected to be the smallest of all of the configurations in a baseline configuration without secondary injection. Case 2.*A*.2 doubled the thickness of the secondary injection slot and was expected to increase the amount of separation that occurs at the throat. Figure 3.21 shows the experimental pressure profile at a NPR of 2.

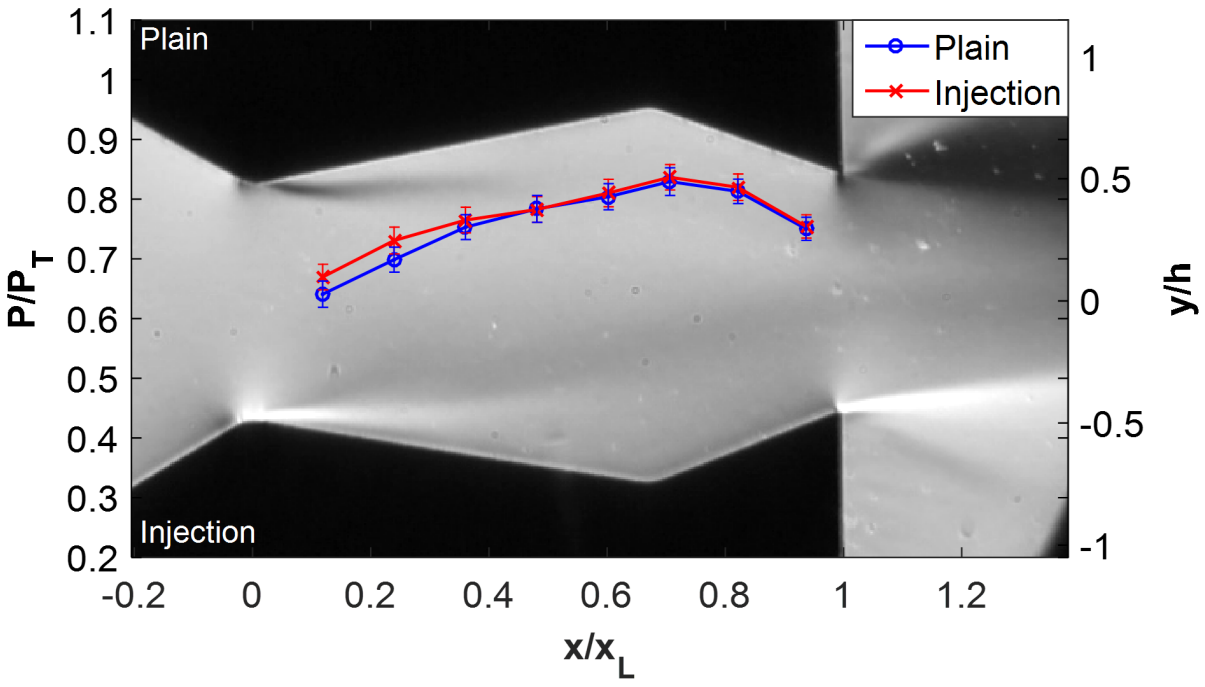

Figure 3.21: Case 2.A.2 schlieren and pressure profile.

Similar to case 1.*A*.2, the wall with the injection geometry has a higher pressure ratio near the throat. However, unlike in case 1.*A*.2, the pressure profile along the injection insert does not decrease below the pressure ratio of the plain surface as would be expected for separated flow

induced by the injection geometry. This decreased separation is corroborated by the schlieren image in Figure 3.21 which shows a larger separation region immediately downstream of the first throat, but is not corroborated by the CFD contour plots presented in Figure 3.22.

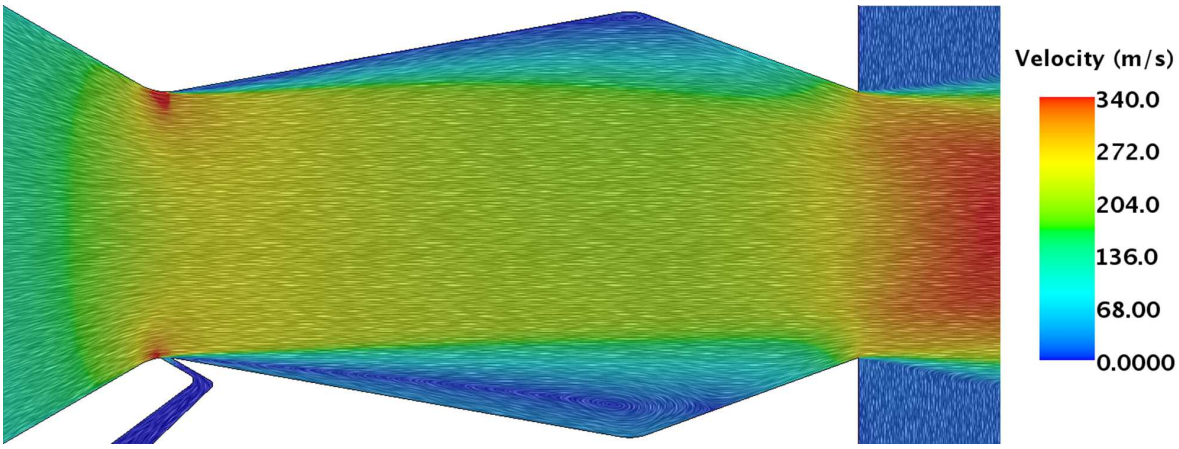

Figure 3.22: Case 2.A.2 CFD velocity contour plot.

In this vector plot, the lower cavity shows slightly increased circulation compared to case 1.A.2 as would have been expected. The increased circulation is a consequence of increased flow separation along that wall and results in a lower secondary injection wall pressure. This increased separation is expected since the thicker slot geometry results in the nozzle wall terminating before the flow is fully straightened. This can be seen in a close-up of the secondary injection geometry in Figure 3.23. In comparison, a later separation point can be seen in Figure 3.24 which shows the flow for the nozzle configuration without secondary injection geometry. The flow separates right at the apex of the corner instead of at the first secondary injection corner which is upstream of where the apex would be. The wall pressure profiles corroborate the increased separation that is seen and are shown in Figure 3.25 (a) and (b). Overall, the secondary injection wall and the plain wall follow the same profile that was seen in case 1.A.2 but the difference between the two profiles is increased. This is representative of increased separation of the secondary injection wall.

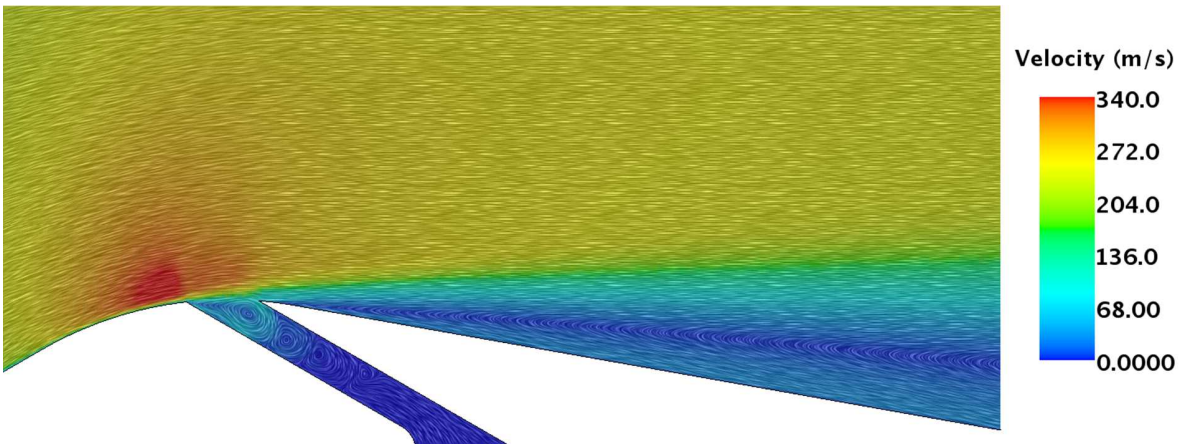

Figure 3.23: Case 2.A.2 CFD velocity contour plot secondary injection closeup.

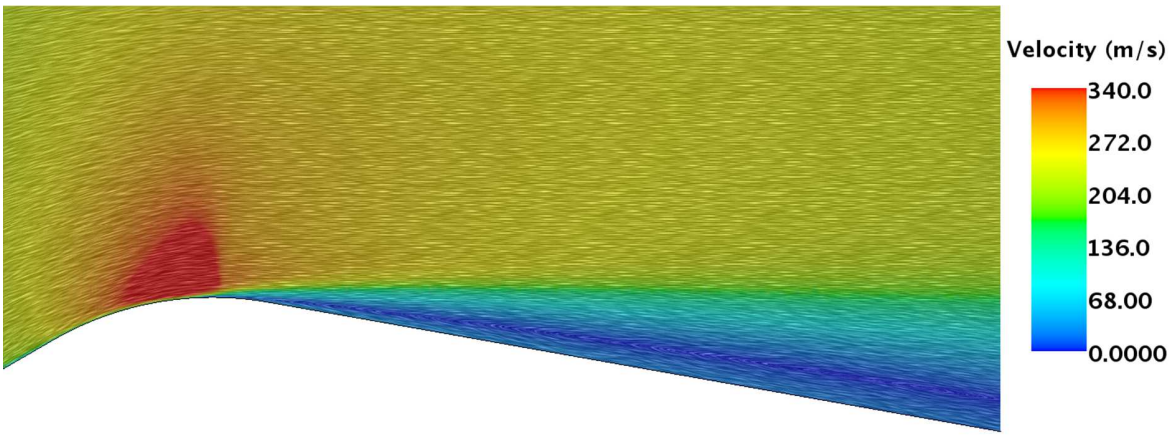

Figure 3.24: Plain CFD velocity contour plot upstream throat closeup.

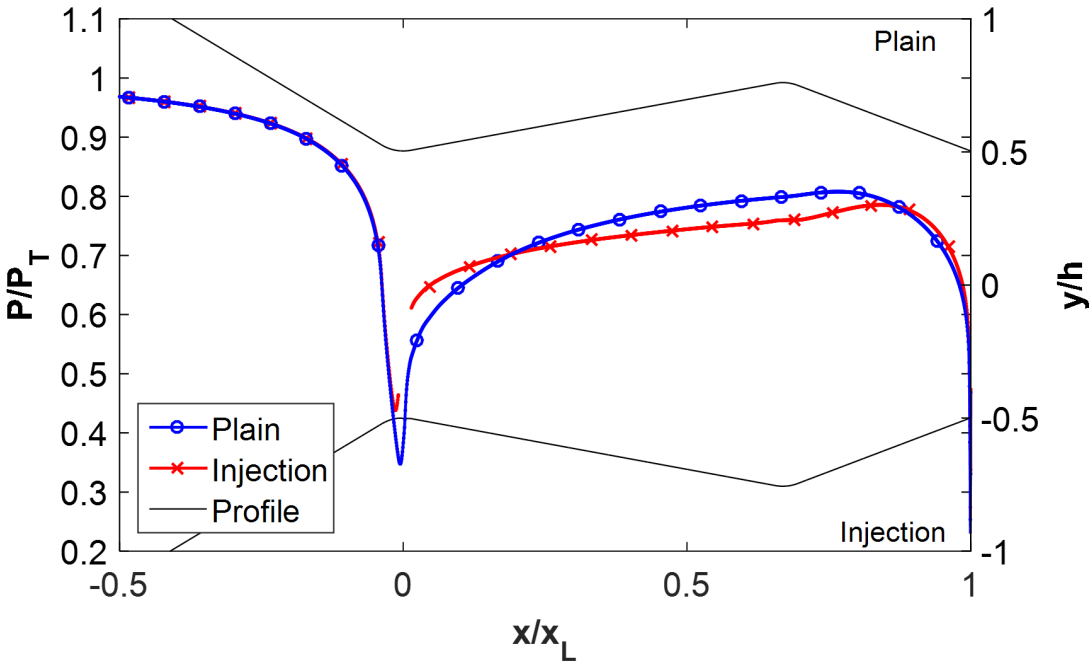

(a) Upper Wall Pressure Profile

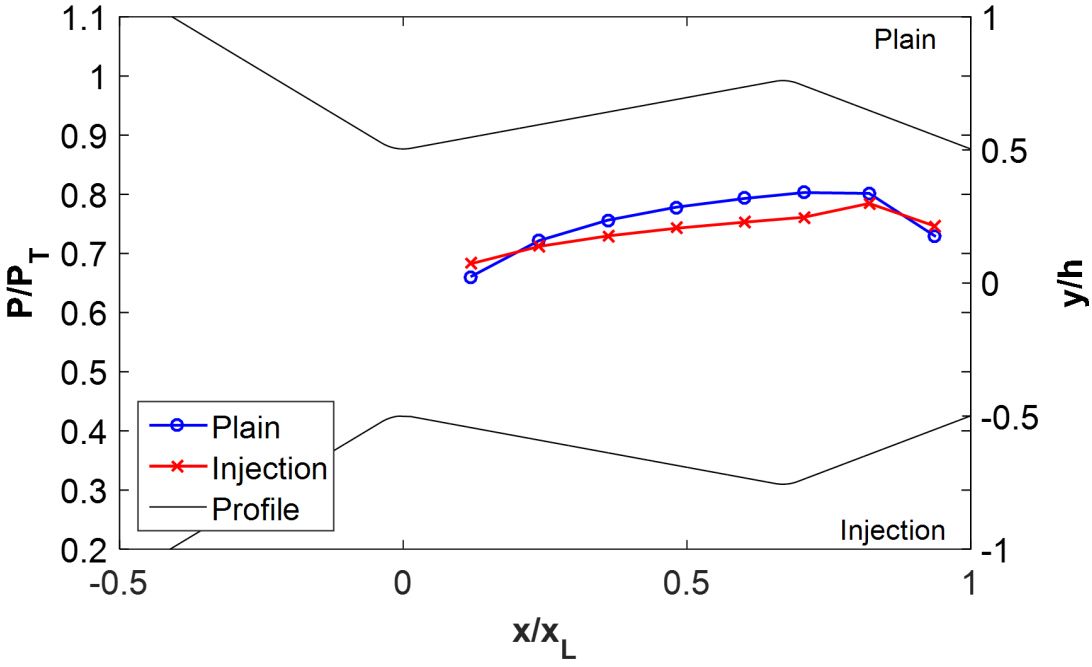

(b) Lower Wall Pressure Profile

Figure 3.25: Case 2.A.2 CFD complete and sampled wall pressure profile.

A possible explanation for why the experimental data does not corroborate the increased separation seen in the CFD can be observed during the transient startup of the tests. Figure 3.26 shows the progression of the schlieren images during the startup for case 2.A.2.

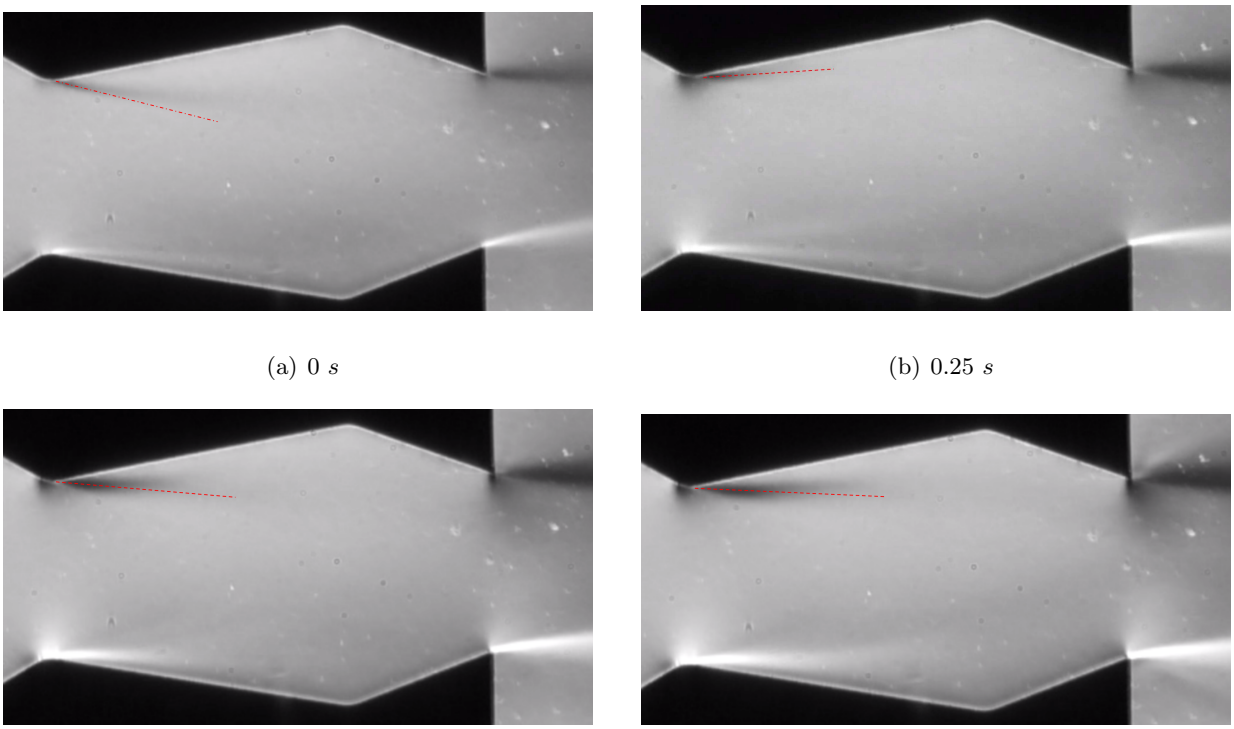

(a) 0 s (b) 0.25 s

(c) 0.5 s (d) 0.75 s

Figure 3.26: Schlieren images displaying the transient startup of case 2.A.2.

The first image at 0 s is taken during the first noticeable density gradient during startup. It is clear there is already a bias towards the lower wall with a large degree of separation at the upper upstream throat. A red dashed line is used to show the approximate direction of flow along the upper throat. This separation then decreases substantially on the upper wall and remains approximately the same on the lower wall. The next two images show the flow developing towards its steady state where the upper wall appears to show a larger degree of separation than the lower wall. This transient during startup where the flow at the upstream throat oscillates was not observed with case 1.A.2 suggesting this initial condition transient behavior may be affecting the

steady-state flow characteristics.

In case 3.*A*.2, secondary injection is provided using a series of holes instead of a slot. This inherent three dimensionality allows additional cross-stream components of the velocity to develop, especially in between the secondary injection hole geometries. Figure 3.27 shows the pressure ratio profiles for the secondary injection and plain wall with zero secondary mass injection.

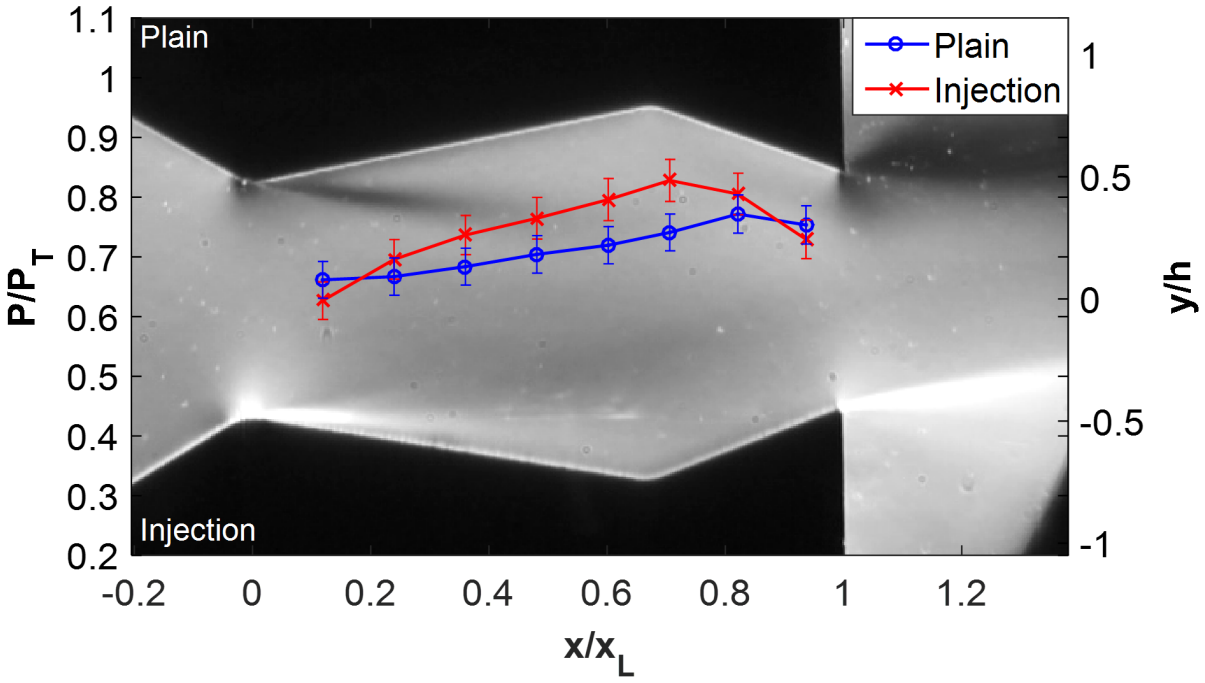

Figure 3.27: Case 3.A.2 schlieren and pressure profile.

In this baseline test without secondary injection, a significant pressure ratio bias towards the secondary injection wall was found. This effect is in stark contrast to the results from case 1.A.2 in which the pressure ratio profile on the injection insert indicated separation. In this configuration, however, the pressure profile and schlieren both indicate flow attachment to the secondary injection wall instead. A possible explanation for this behavior is that the three dimensionality of the secondary injection holes induces vortices in the streamwise direction. This effect could re-energize the boundary layer and reduce or even eliminate flow separation on that surface. Unfortunately,

since this secondary injection geometry is three dimensional, the 2D solver could not be used to solve this flow field. Thus a comparison can not be made with the CFD for this case. Overall, case 3.A.2 was tested 5 times and resulted in a relatively high standard deviation between tests. This is apparent in the error bars in Figure 3.27 in which part of its value is the variation between tests.

3.4 Secondary Injection Tests

For each of the configurations outlined in Table 3.1 secondary flow was added. A range of secondary mass flow rates were evaluated in order to derive a relationship between injection mass flow rate and vector angle. However, due to the pressure limit of the secondary mass flow controller, the maximum mass flow rate allowable for each configuration varied based on their total injection area. Table 3.2 shows the tests conducted for each configuration in terms of injection percentage and injection mass flow rate.

Table 3.2: Secondary Injection NPR = 2 Test Cases

	Case 1.*.2	Case 2.*.2	Case 3.*.2
Lower Test Insert	V1	V2	V3
Upper Test Insert	Plain	Plain	Plain
NPR	2	2	2
Case *.B.2	0.27% (0.105 $\frac{g}{s}$)	0.18% (0.075 $\frac{g}{s}$)	0.20% (0.078 $\frac{g}{s}$)
Case *.C.2	0.42% (0.161 $\frac{g}{s}$)	0.59% (0.245 $\frac{g}{s}$)	0.58% (0.232 $\frac{g}{s}$)
Case *.D.2	0.88% (0.334 $\frac{g}{s}$)	0.77% (0.324 $\frac{g}{s}$)	0.84% (0.327 $\frac{g}{s}$)
Case *.E.2	1.02% (0.389 $\frac{g}{s}$)	0.93% (0.403 $\frac{g}{s}$)	1.00% (0.394 $\frac{g}{s}$)
Case *.F.2	2.20% (0.808 $\frac{g}{s}$)	1.91% (0.818 $\frac{g}{s}$)	2.07% (0.817 $\frac{g}{s}$)
Case *.G.2	3.39% (1.21 $\frac{g}{s}$)	2.88% (1.22 $\frac{g}{s}$)	2.88% (1.22 $\frac{g}{s}$)
Case *.H.2	4.10% (1.46 $\frac{g}{s}$)	3.93% (1.63 $\frac{g}{s}$)	4.30% (1.63 $\frac{g}{s}$)
Case *.I.2	N/A	4.99% (2.04 $\frac{g}{s}$)	5.53% (2.08 $\frac{g}{s}$)

3.4.1 Nozzle Pressure Ratio of 2

3.4.1.1 Case 1.*.2

Starting with the case 1.*.2 test cases, secondary mass injection ranged from 0.27% to 4.1% of the core flow mass flow rate for this case. Figure 3.28 shows the case in which 0.27% of the core flow is injected.

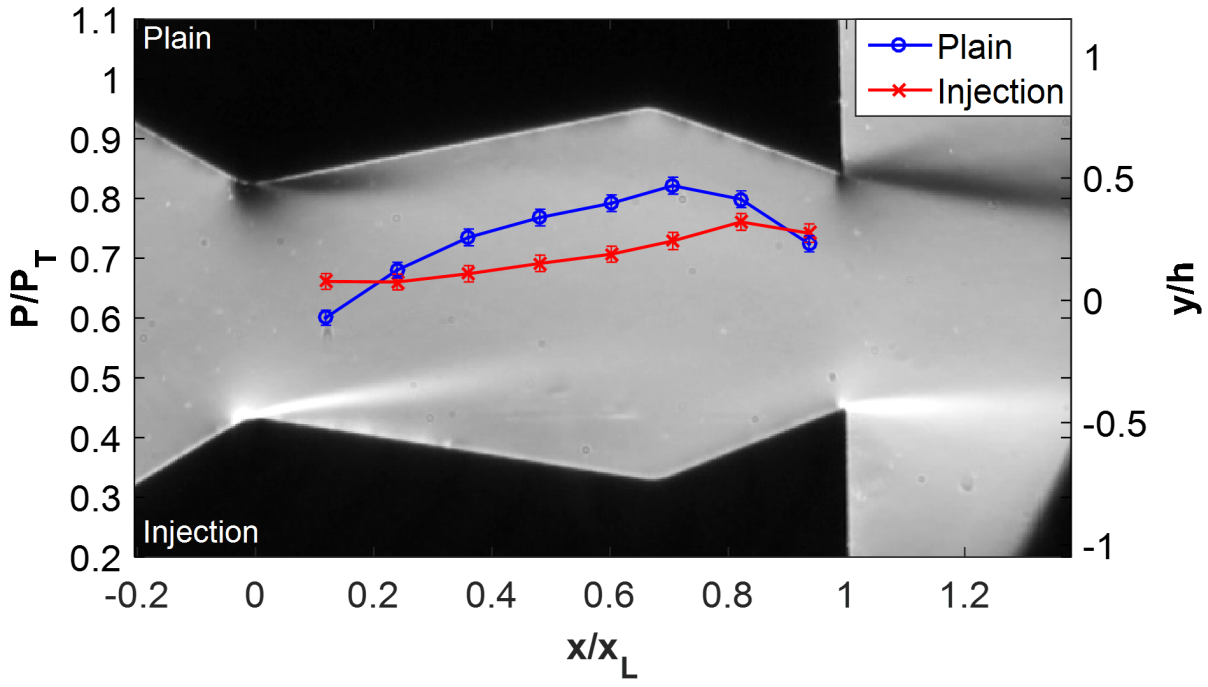

Figure 3.28: Case 1.B.2 schlieren and pressure profile.

The small amount of secondary injection in $1.B.2$ can be seen to considerably increase the amount of separation on the injection wall while improving the attachment along the plain upper wall. This can be seen visually as well with the schlieren with flow at the upstream throat showing a lightly upward direction. A progression of the wall pressure ratio profiles overlaid on the schlieren for the remaining test cases are shown in Figure 3.29 through 3.31.

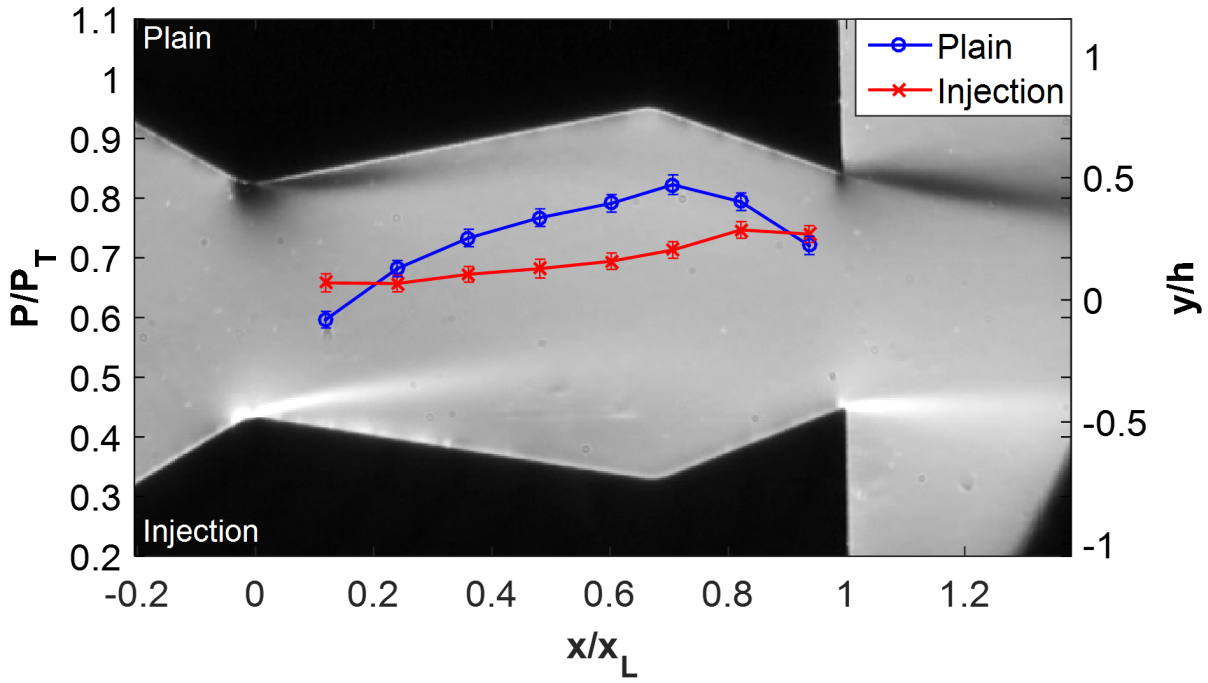

(a) Case 1.C.2

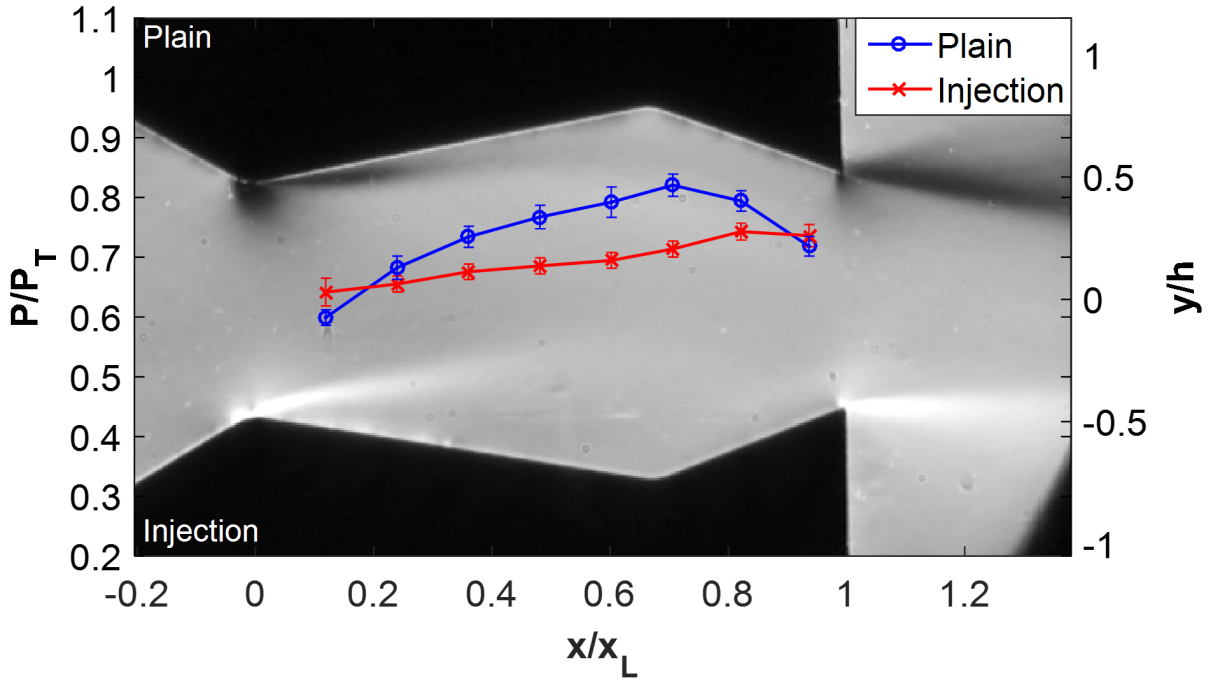

(b) Case 1.D.2

Figure 3.29: Cases 1.C.2 and 1.D.2

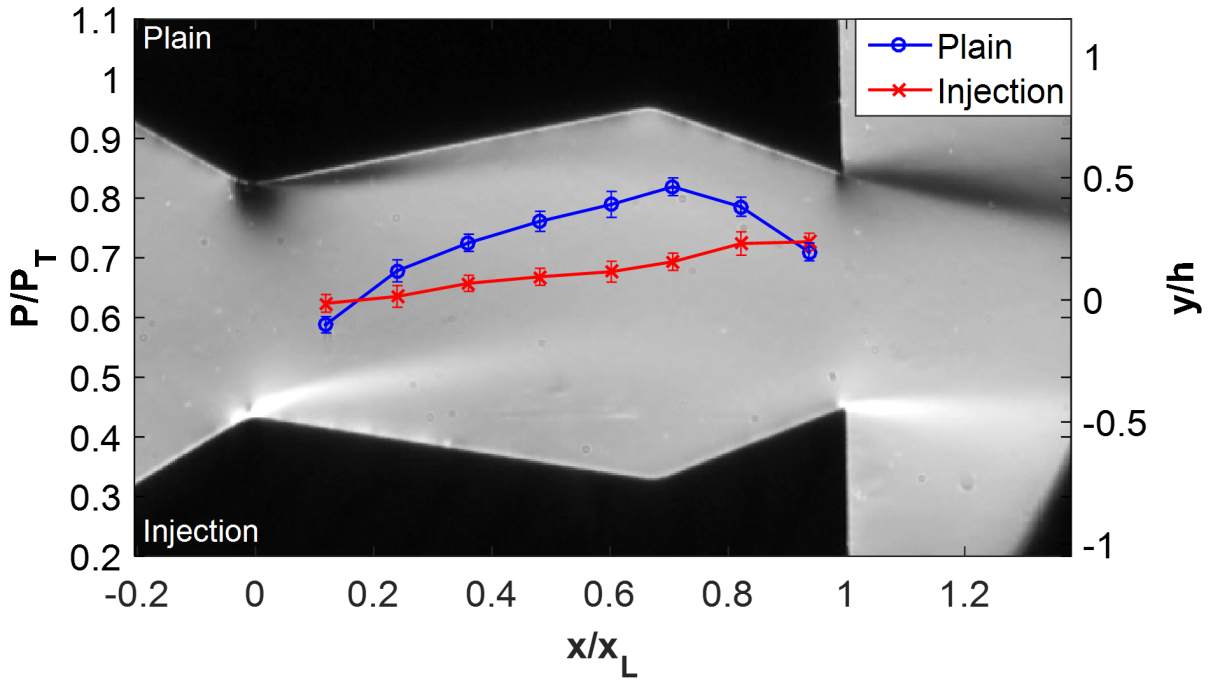

(a) Case 1.E.2

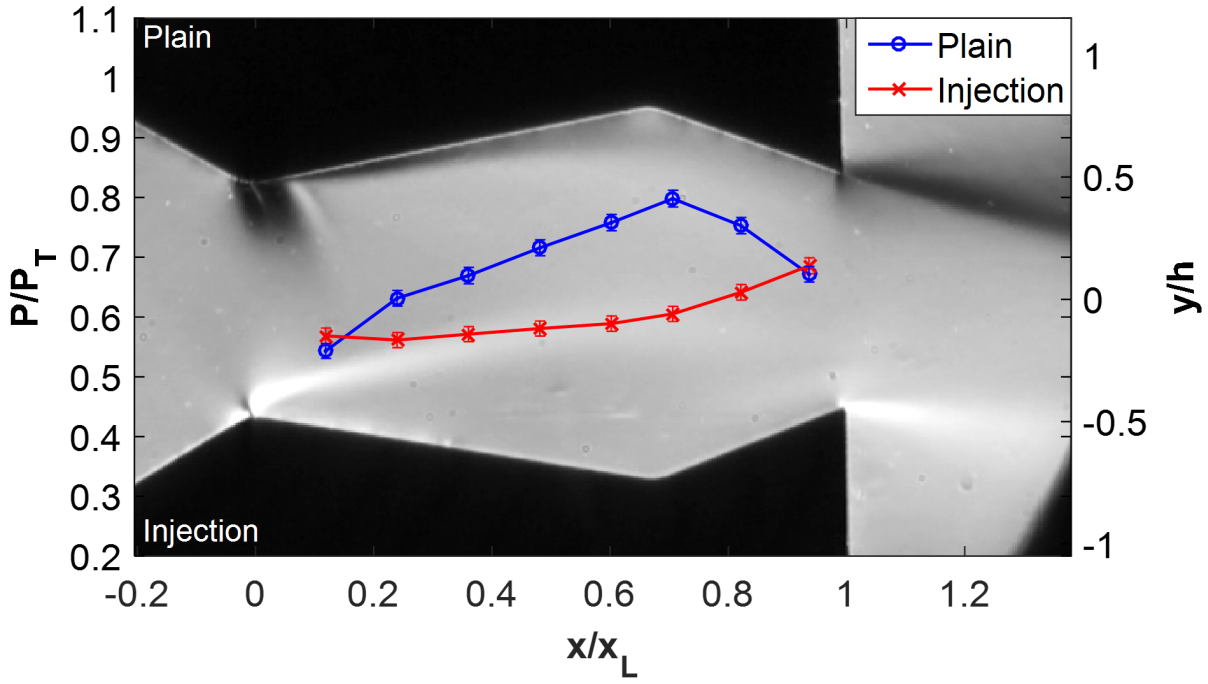

(b) Case 1.F.2

Figure 3.30: Cases 1.E.2 and 1.F.2

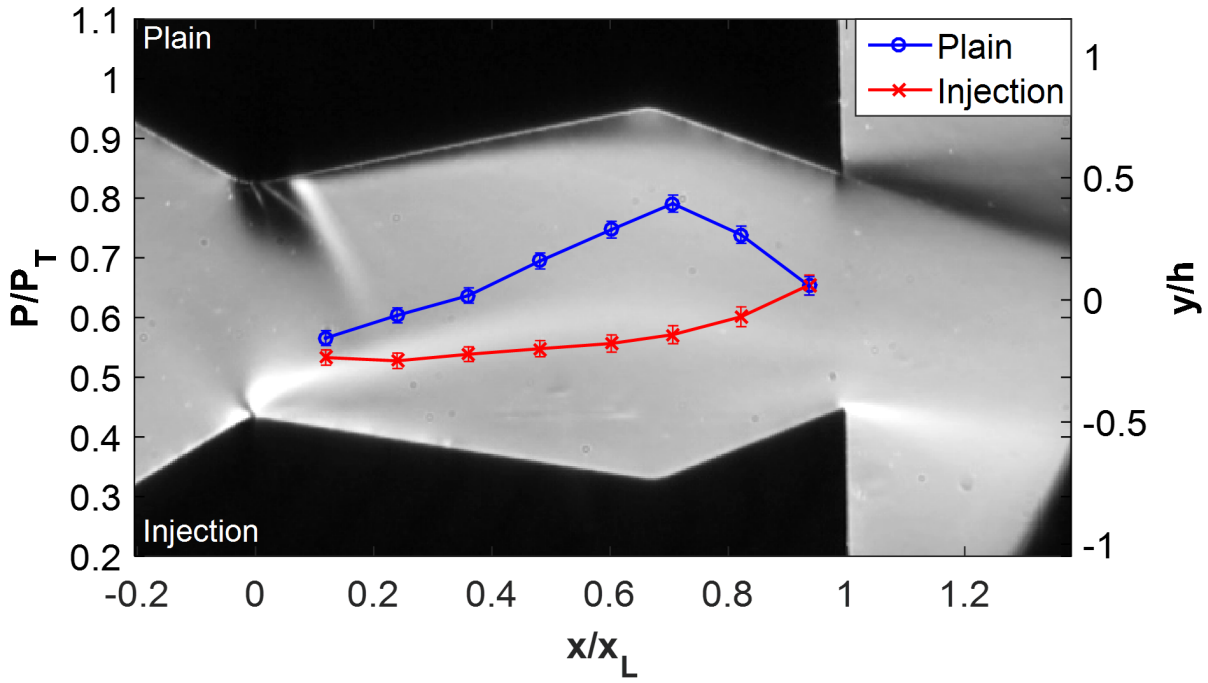

(a) Case 1.G.2

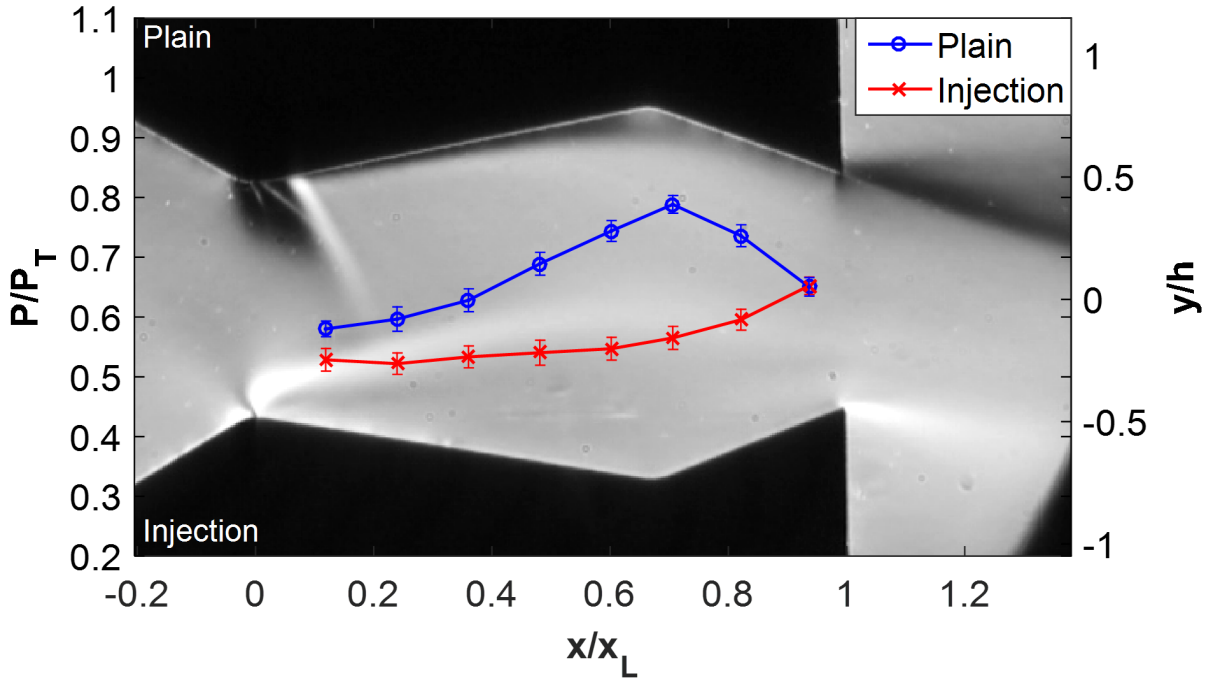

(b) Case 1.H.2

Figure 3.31: Cases 1.G.2 and 1.H.2

Cases 1.B.2 through 1.E.2 show relatively little change in the pressure ratio profile since there is little change in the injection percentage. However, beginning with case 1.F.2, a noticeable change in the flow structure can be seen with the development of a shock on the upper plain wall. With a further increase in secondary injection, the strength of the shock grows. In cases 1.G.2 and 1.H.2, this shock becomes strong enough to induce separation in the flow as indicated by the flattening of the upper plain wall pressure ratio between the first and second pressure taps. Reattachment can be seen to happen near the fourth pressure tap where there is noticeable increase in pressure ratio. To better visualize the pressure throughout the nozzle, Figure 3.32 shows the static pressure contours for the case 1.E.2 calculated from CFD. The asymmetry between the upper and lower surfaces is obvious. While a large supersonic expansion region can be seen on the upper wall at the upstream throat, there is separation at the lower wall resulting in no expansion and a roughly constant static pressure. Figure 3.33 shows the complementary vector field. In this vector plot, it is actually possible to see that the area of lowest pressure at the upstream throat is supersonic and is terminated by an oblique shock. Flow then decreases in velocity along the plain upper wall as the area between the top of separation pocket on the lower injection wall and the plain wall increases. The wall pressures associated with the CFD are shown in Figure 3.34 where Figure 3.34 (a) shows the full CFD pressure ratio profile and Figure 3.34 (b) shows the CFD pressure profile sampled at the experimental pressure tap locations. Once again, the pressure ratio profile sampled at experimental locations drastically under sample the pressure at the two throats which is the location of the highest pressure gradients. However, the rest of the nozzle is well sampled with the discretization providing little error within the sampled region. A comparison between the CFD and the experiment shows a significant discrepancy between the two as shown in Figure 3.35.

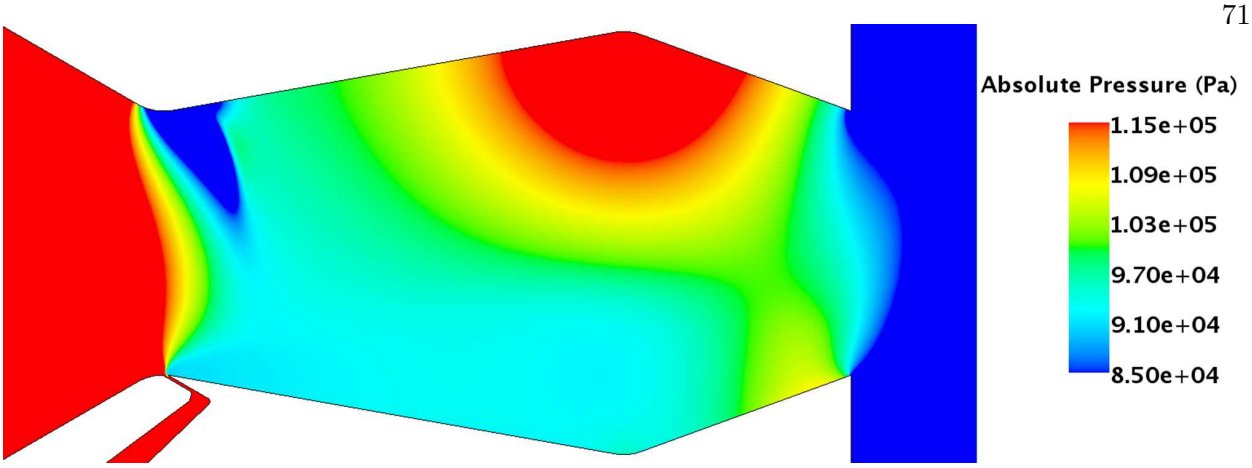

Figure 3.32: Case 1.E.2 CFD static pressure contour plot.

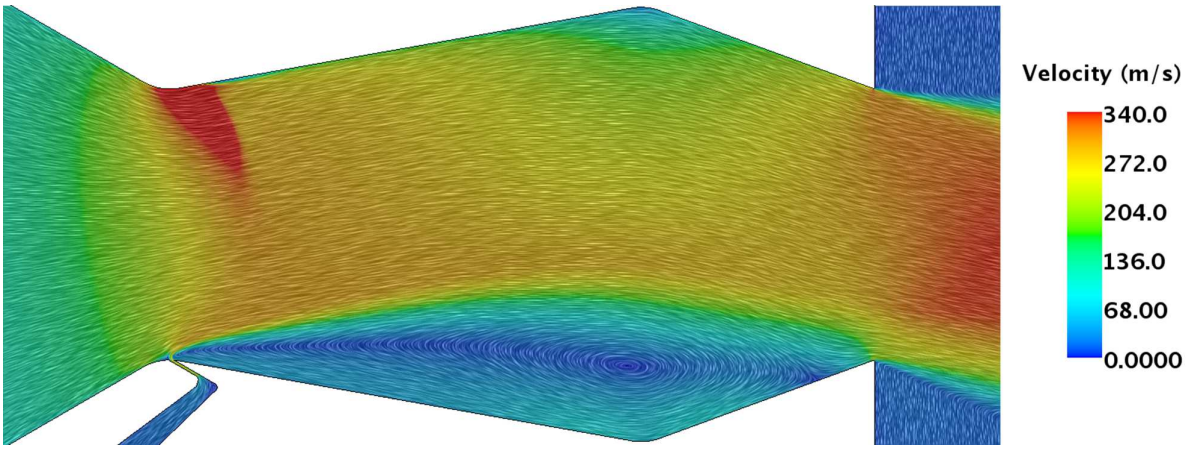

Figure 3.33: Case 1.E.2 CFD velocity contour plot.

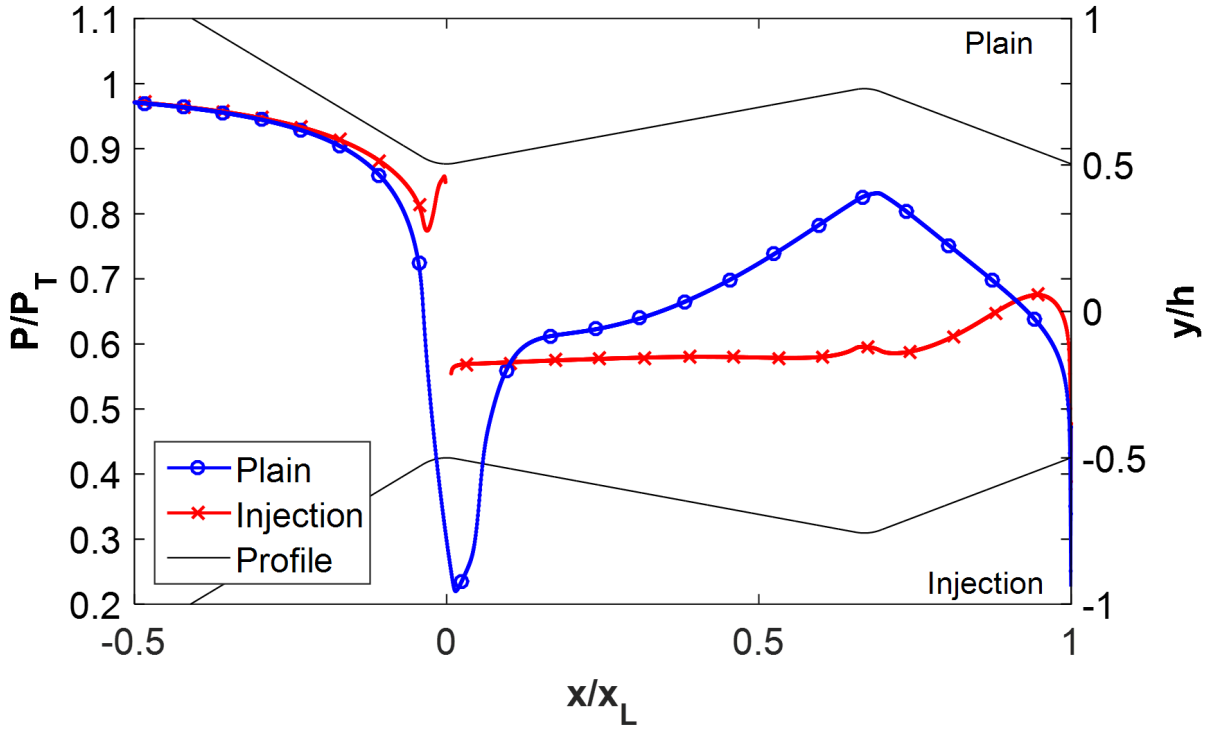

(a) Case 1.E.2 CFD Profile

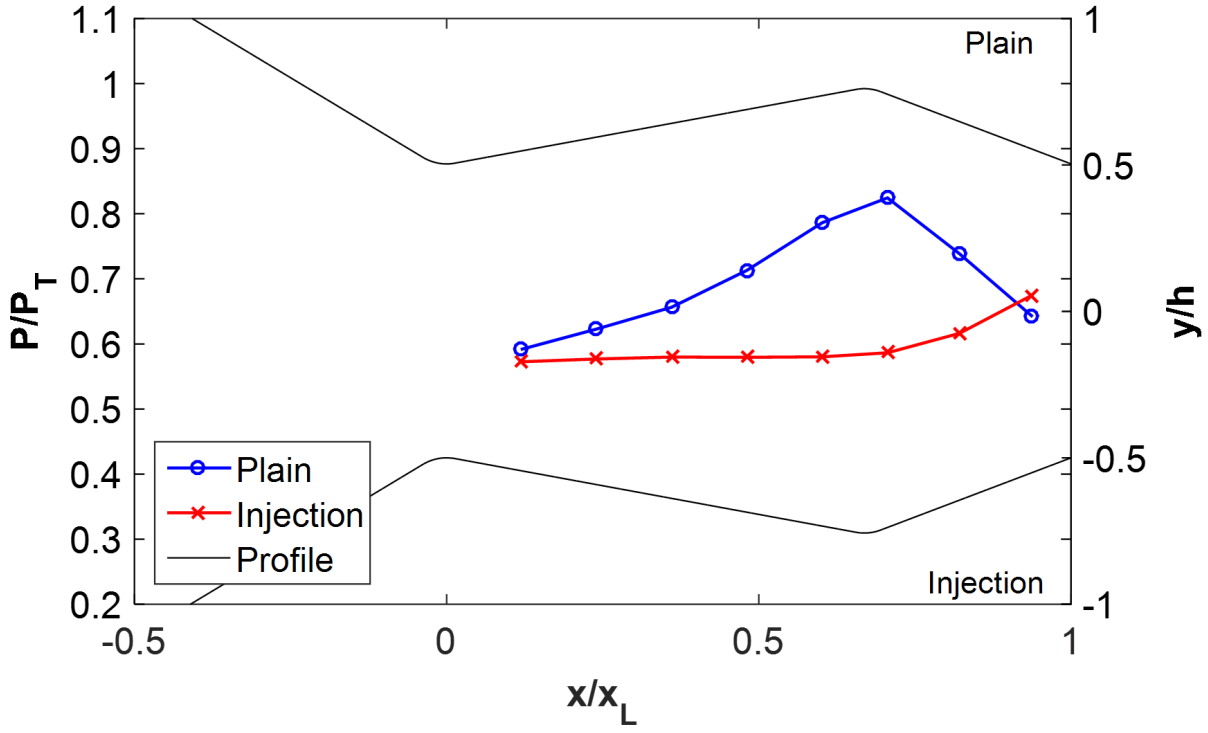

(b) Case 1.E.2 Sampled CFD Profile

Figure 3.34: Case 1.E.2 CFD pressure profiles.

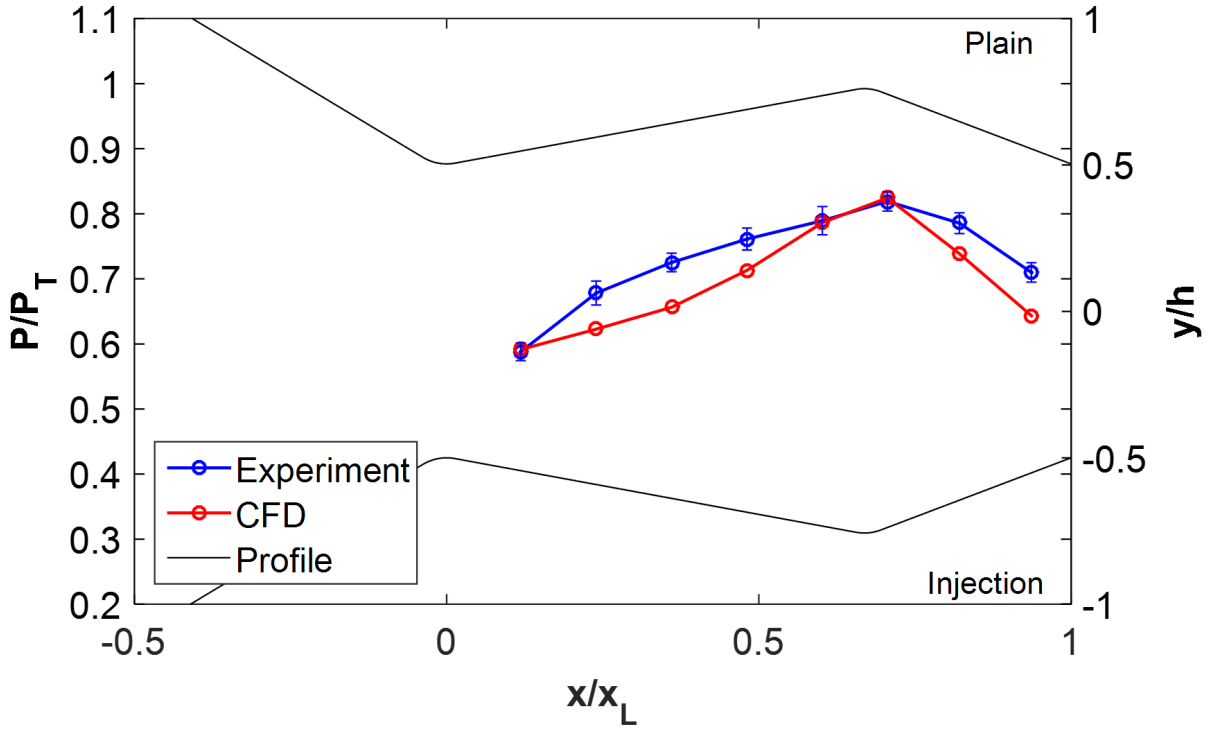

(a) Upper Wall Pressure Profile

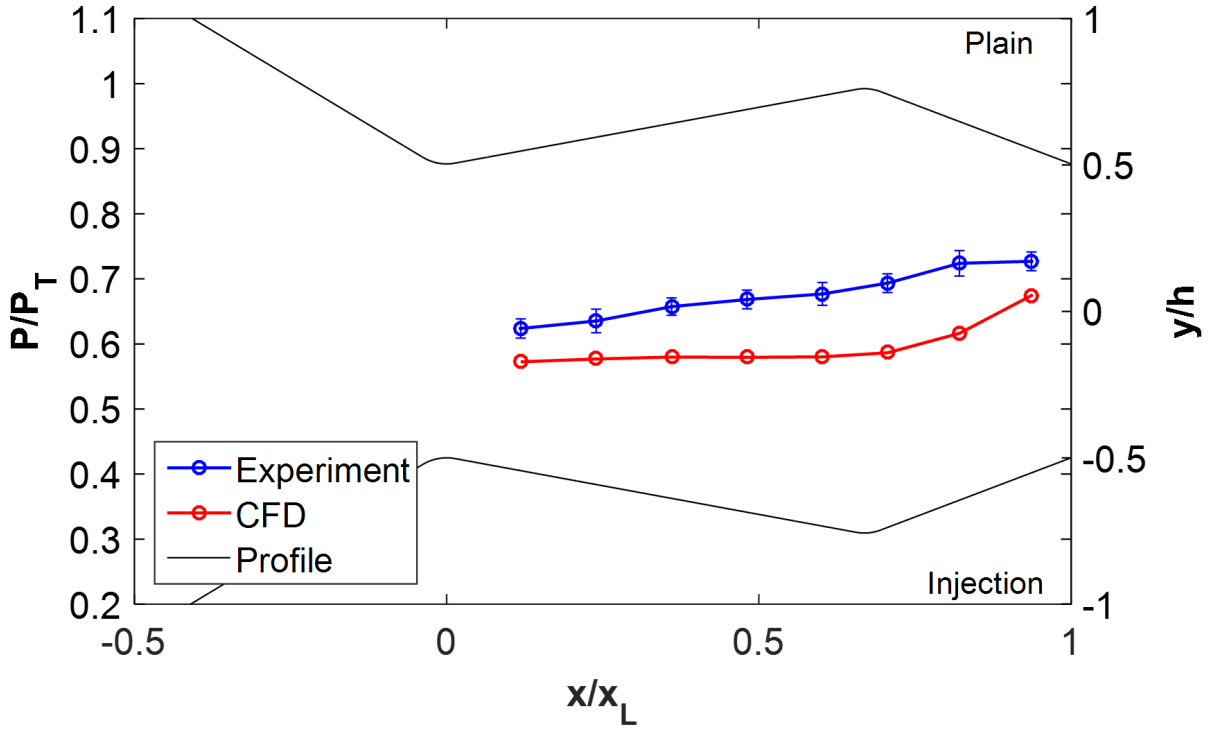

(b) Lower Wall Pressure Profile

Figure 3.35: Case 1.E.2 comparison between experimental and CFD pressure profile.

For both the upper and lower wall pressure profiles, the CFD either matches or underestimates the pressure ratio at each sampling location. This is the opposite phenomenon seen for the case 1.A.2 test in which the CFD underestimated the amount of separation at the upstream throat and gave a higher pressure ratio than the experiment. The likely reason for this separated region on the upper plain wall is the shock that is formed immediately after the upstream throat. A close-up of this region is shown in Figure 3.36.

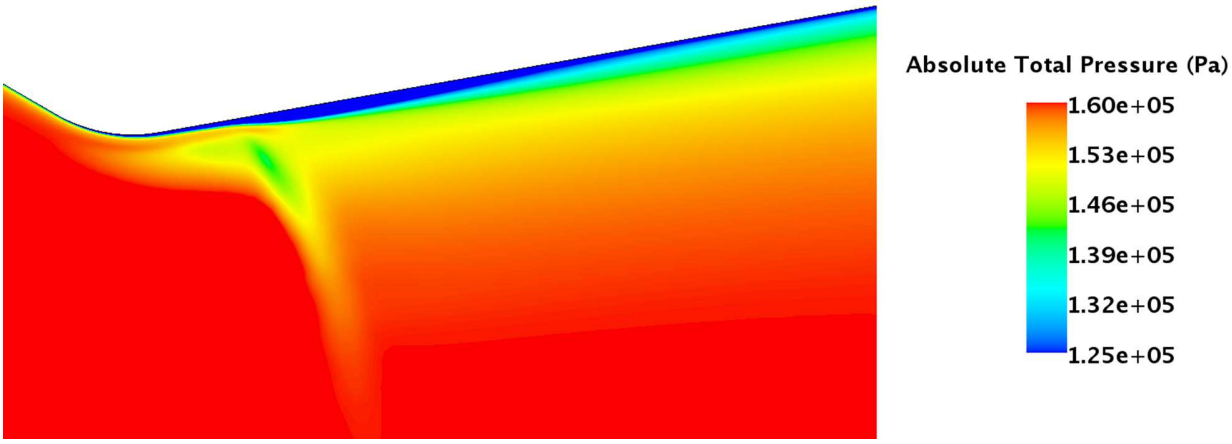

Figure 3.36: Case 1.E.2 CFD shock induced separation.

In the contour plot, a separated region can be seen developing at the point the shock intersects the wall. This shock boundary layer interaction is known to induce boundary layer separation and is likely the cause of the separation seen in this case. However, while this shock is seen in the CFD, there is no indication of a large density gradient in the schlieren of case 1.E.2. A close-up of the schlieren is shown in Figure 3.37.

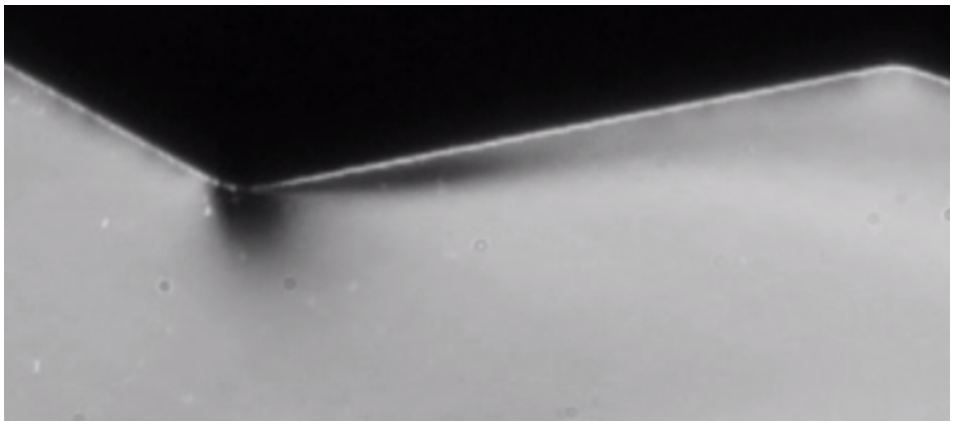

Figure 3.37: Case 1.E.2 schlieren shock induced separation.

As the secondary injection mass flow rate is increased, the formation of this shock becomes more apparent in the experimental data. Additionally, the drooping of the upper plain wall pressure ratio profile that was seen in the CFD of case 1.E.2 develops in the pressure ratio profiles of case 1.G.2, 1.H.2, and 1.I.2 as shown in Figure 3.38.

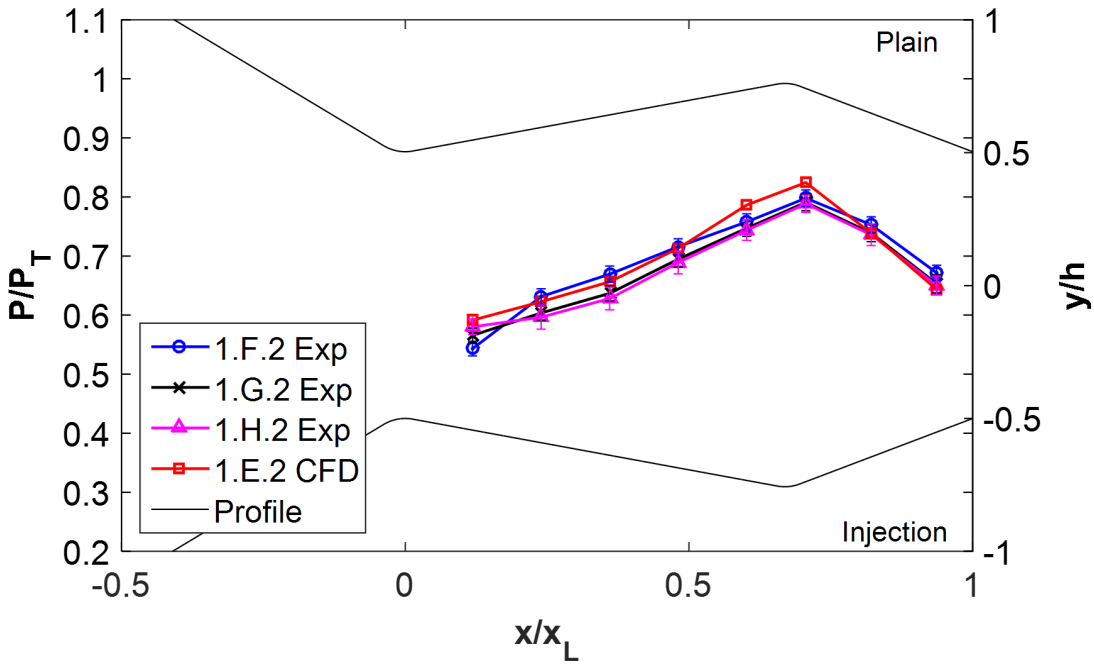

Figure 3.38: Case 1.F.2 through 1.H.2 upper plain pressure profiles.

Compared with the CFD of the 1.E.2 case, the experimental data of each of the higher injection cases matches the general form of the pressure profile. This suggests that at least for the 1.E.2 case, the CFD is predicting a much more significant expansion fan around the upstream throat which is resulting in a stronger shock. This shock, however, is seen to have the same effect computationally as it does experimentally where the shock interacts with the boundary layer and induces separation. The progression of wall profiles as a function of injection percentage shows a clear trend in which the plain wall pressure profile increases in pressure while the secondary injection wall profile decreases. Figure 3.39 shows the plain and injection wall profiles as a function of injection percentage for both experimental and CFD results.

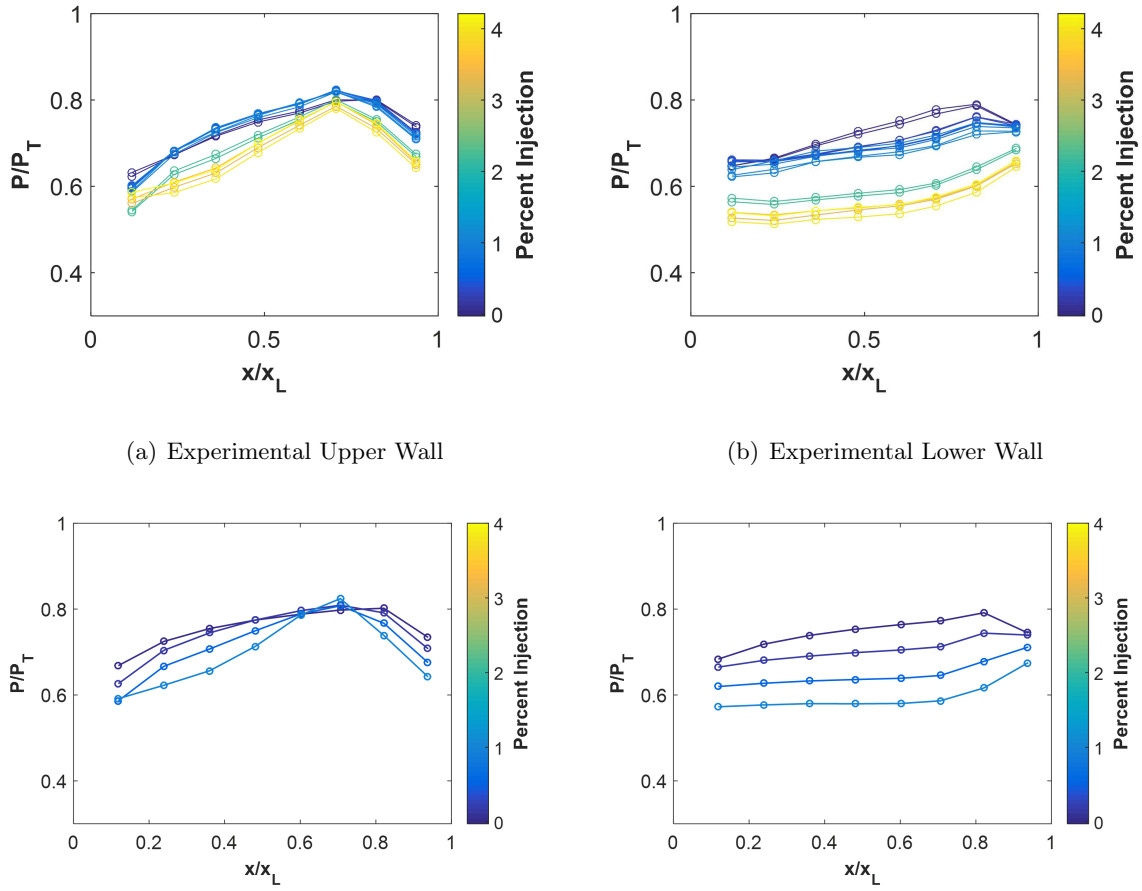

(a) Experimental Upper Wall

(b) Experimental Lower Wall

(c) CFD Upper Wall

(d) CFD Lower Wall

Figure 3.39: Case 1.*.2 wall pressure profile progression as a function of injection percentage.

The trends seen in the experimental results on the secondary injection and plain walls are generally the same as those seen in the CFD, however there are some discrepancies. The most distinct is how the lower injection wall pressure profile shifts down as the injection percentage increases. Although this was seen in the experimental results, it was only seen with much larger injection percentages.

3.4.1.2 Case 2.*.2

The second configuration analyzed for injection is case 2.*.2. The only difference between case 1.*.2 and 2.*.2 is that the injection slot is doubled in thickness. Changes in the pressure profiles as well as the flow structure were of particular interest. Additionally, since the injection geometry was larger than that of Configuration 1.*.2, the secondary injection mass flow rates were increased slightly and ranged from 0.18% to 4.99% of the core mass flow rate. Figure 3.40 shows the secondary injection and plain wall pressure profile for an injection percentage of 0.18%.

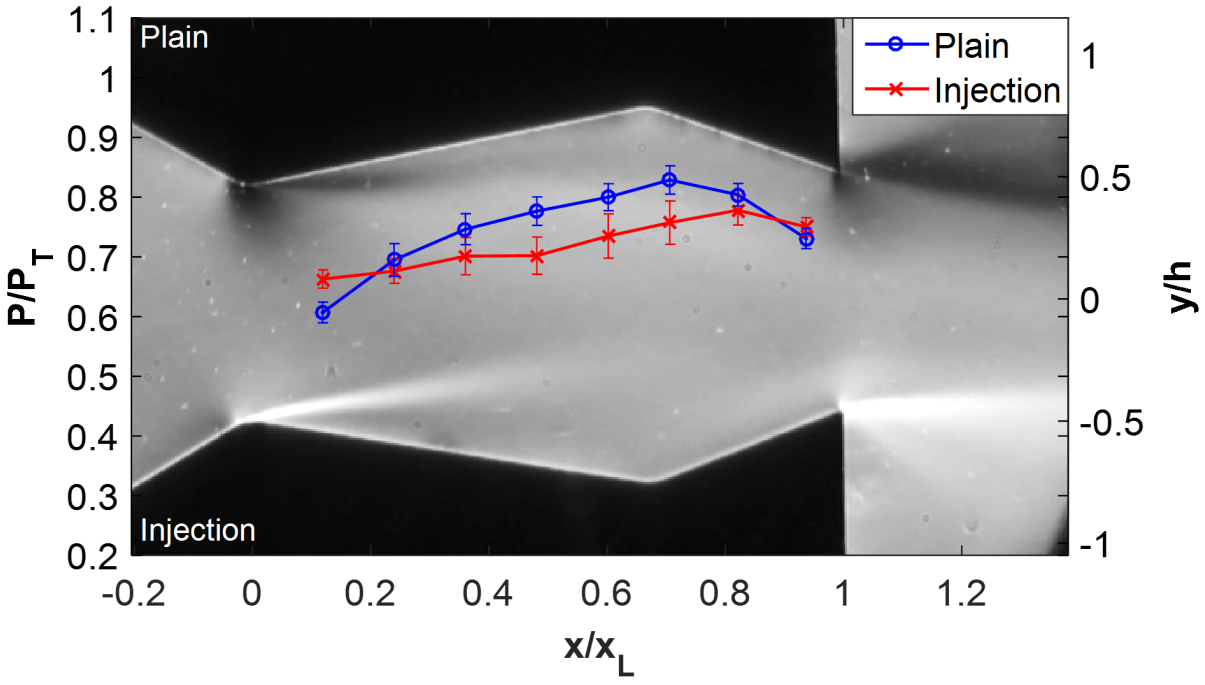

Figure 3.40: Case 2.B.2 schlieren and pressure profile.

Similar to case 1.B.2, the small amount of secondary mass flow rate was seen to considerably increase the amount of separation on the lower injection wall. However, a difference that was noted between the 1.B.2 and 2.B.2 is a significantly larger error at each of the pressure taps, likely due to the component of the error based on the standard deviation of the data between tests. This behavior is likely due to the same startup transient behavior that was noted during the 2.A.2 tests shown in Figure 3.26. However, as shown in the following figures, this variation between tests decreases as the secondary injection mass flow rate is increased. Figure 3.41 through 3.43 shows a progression of the wall pressure profiles for the remaining 2.*.2 tests.

Similar to the case 1.*.2 cases, there is relatively little change in the pressure profiles between 2.B.2 and 2.E.2. Additionally, the same drooping shape of the upper plain wall pressure profile does begin to form at case 2.I.2 and is accompanied by a similar shock on the upper wall just after the upstream throat. However, a noticeable difference is that this shock only begins to form in the schlieren at 4.99% secondary injection, while in the 1.*.2 case the shock was seen as soon as 2.2% secondary injection. A difference in pressure contours between the 1.E.2 case and the 2.E.2 case was also noted. Figure 3.44 shows the pressure contours for the latter.

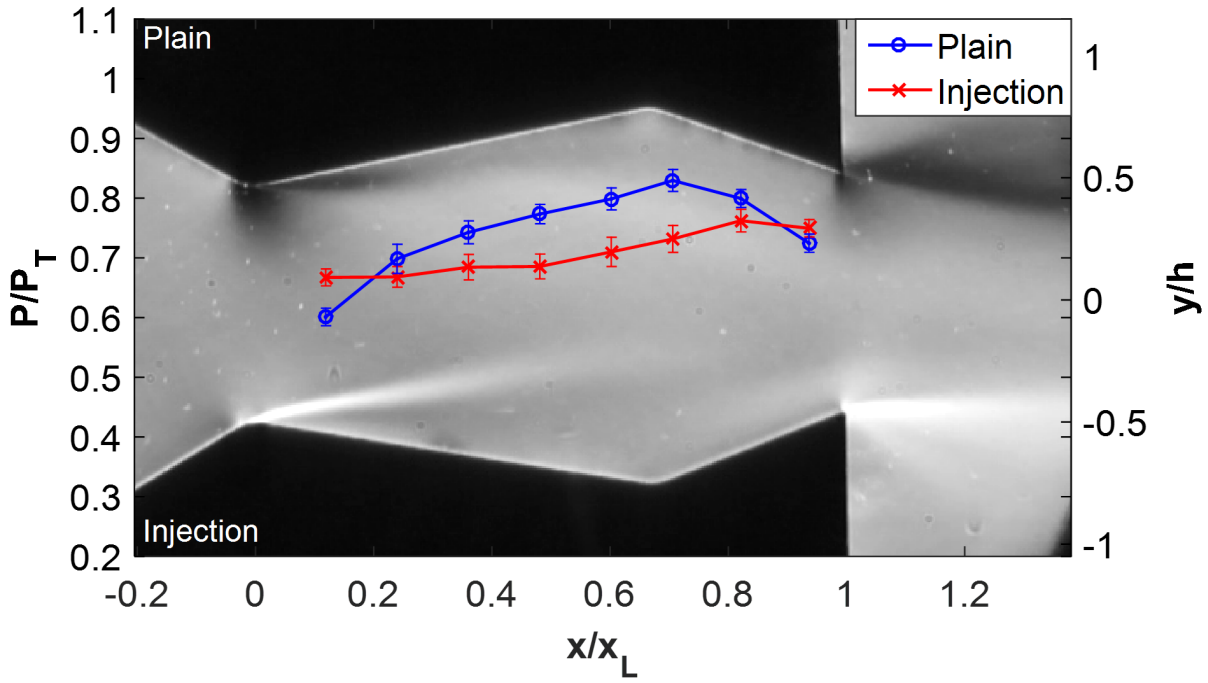

(a) Case 2.C.2

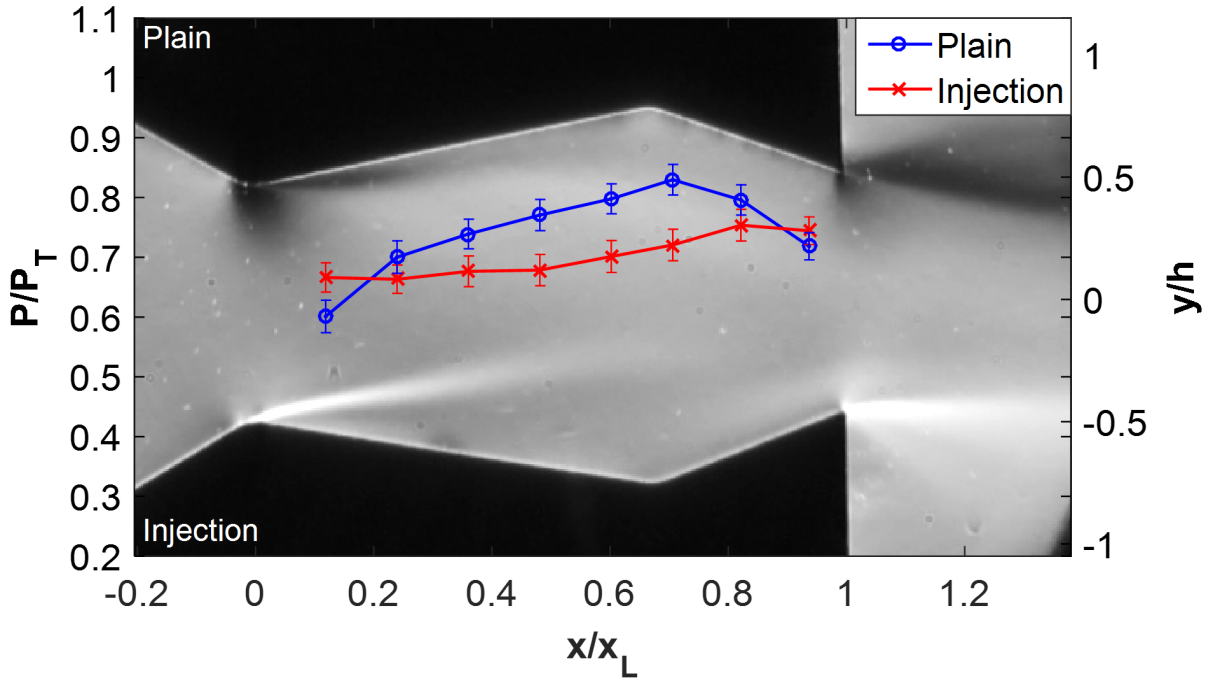

(b) Case 2.D.2

Figure 3.41: Cases 2.C.2 and 2.D.2

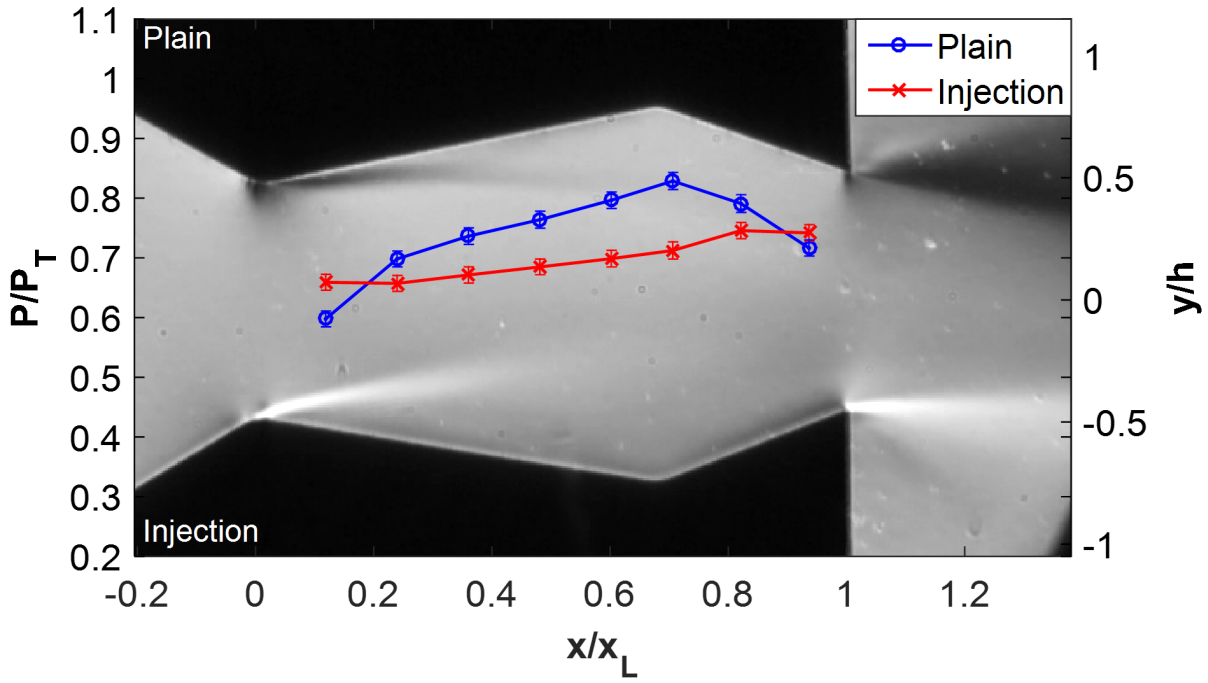

(a) Case 2.E.2

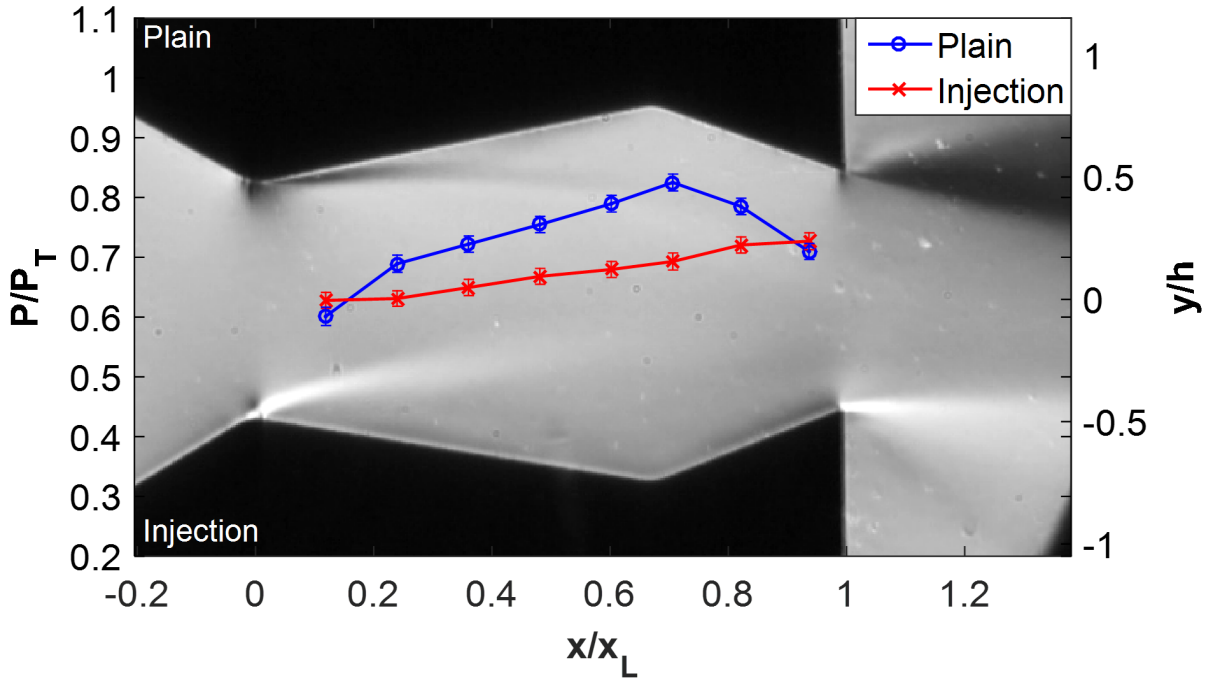

(b) Case 2.F.2

Figure 3.42: Cases 2.E.2 and 2.F.2

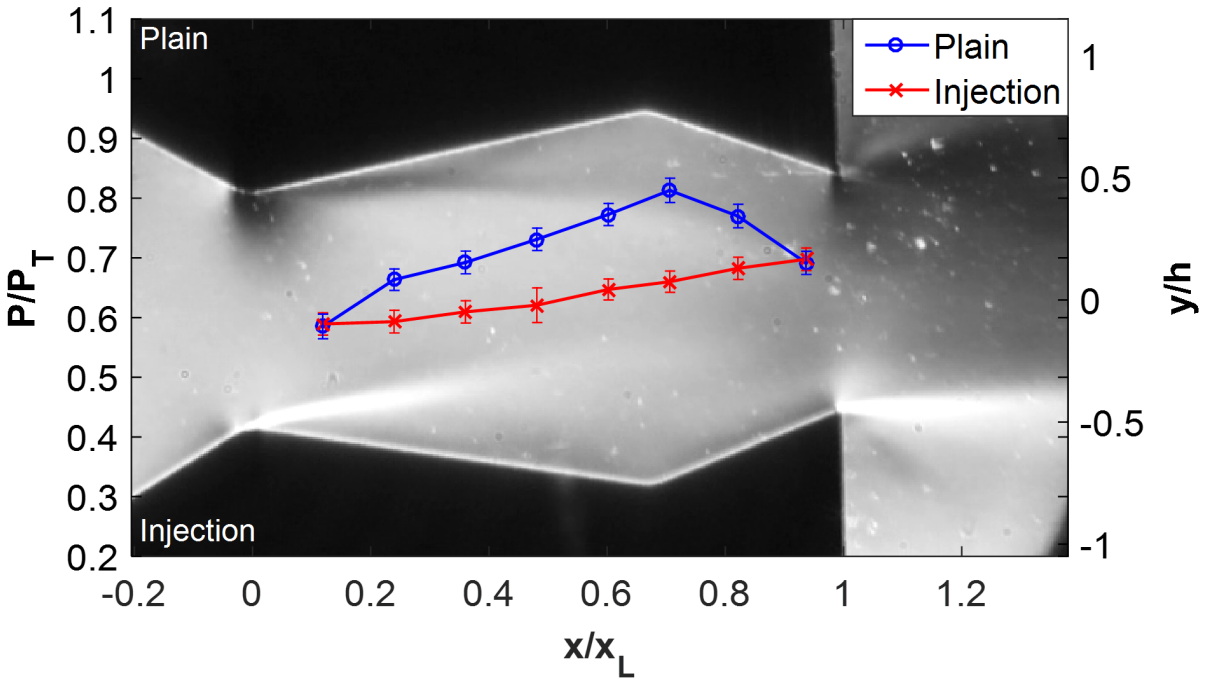

(a) Case 2.G.2

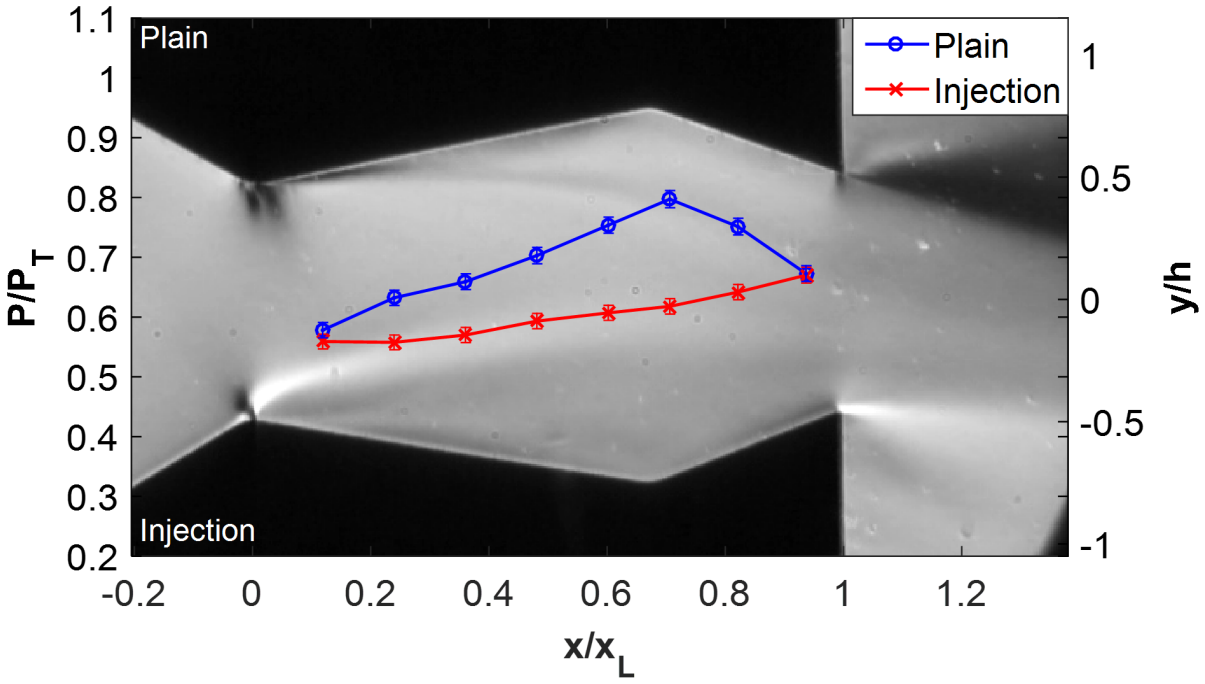

(b) Case 2.H.2

Figure 3.43: Cases 2.G.2 and 2.H.2

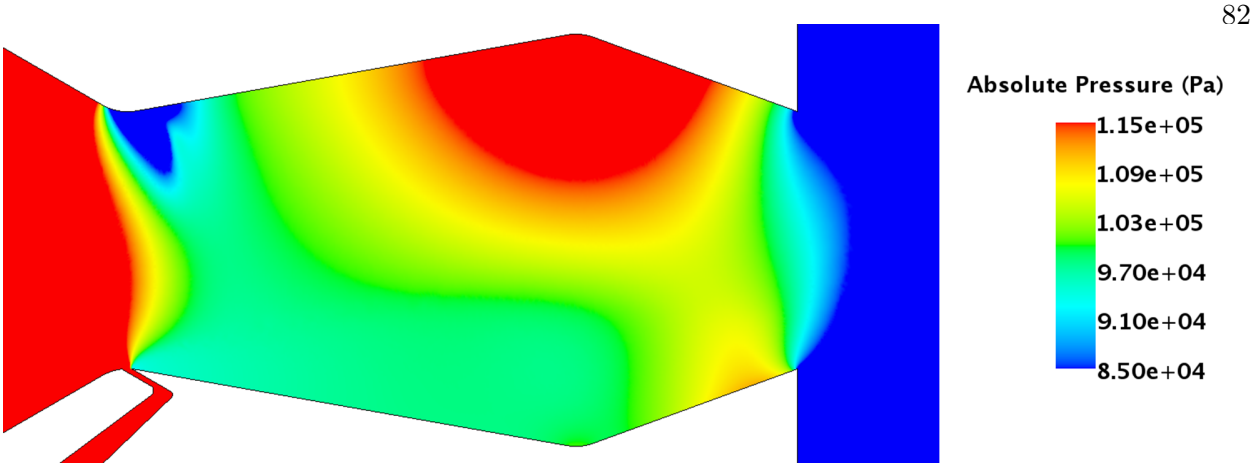

Figure 3.44: Case 2.E.2 CFD static pressure contour plot.

The general pressure distribution is similar to that of 1.E.2. However, there is a noticeable difference in pressure contours around the plain wall upstream throat. In case 1.E.2, the low pressure contour extends approximately half way down the height of the throat. However, in case 2.E.2, the contour only extends about one third of the way down. Additionally, the pressure is higher in the lower left quadrant compared to 1.E.2. This indicates that the circulation pocket is smaller in 2.E.2 and is resulting in a lower thrust-vector at the nozzle exit. This circulation pocket can be seen in Figure 3.45 showing a velocity vector plot.

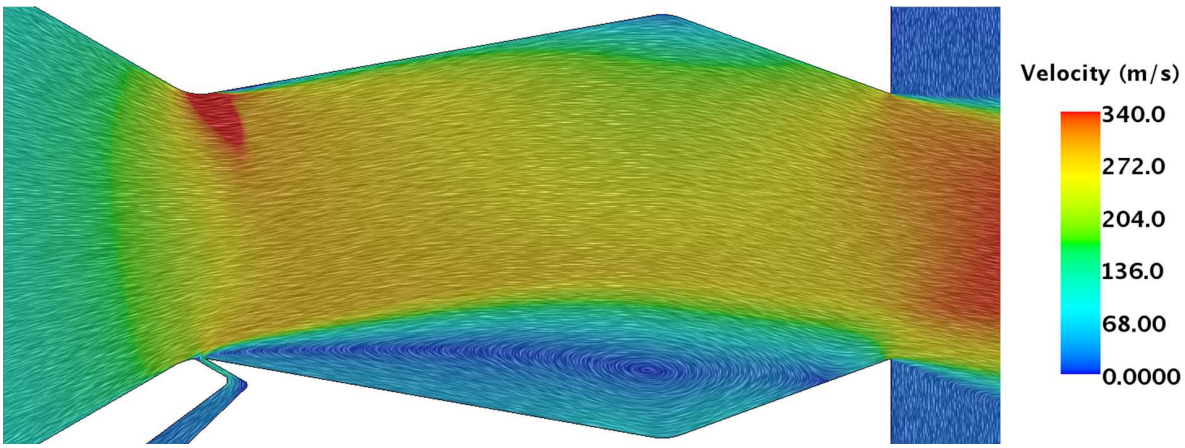

Figure 3.45: Case 2.E.2 CFD velocity contour plot.

The reason for this smaller circulation pocket is apparent when the y component of the velocity is compared at the secondary injection locations as shown in Figure 3.46.

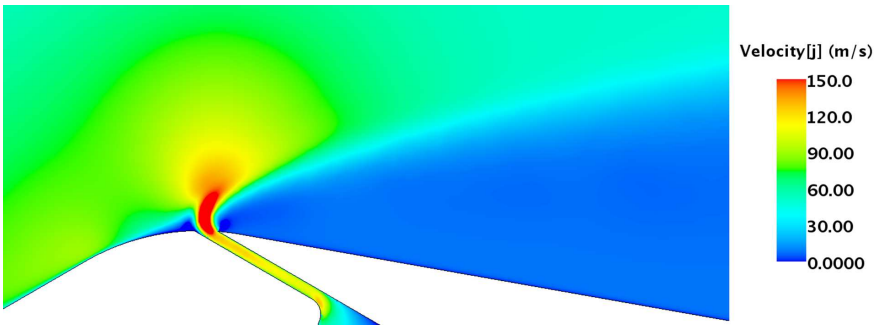

(a) Case 1.E.2

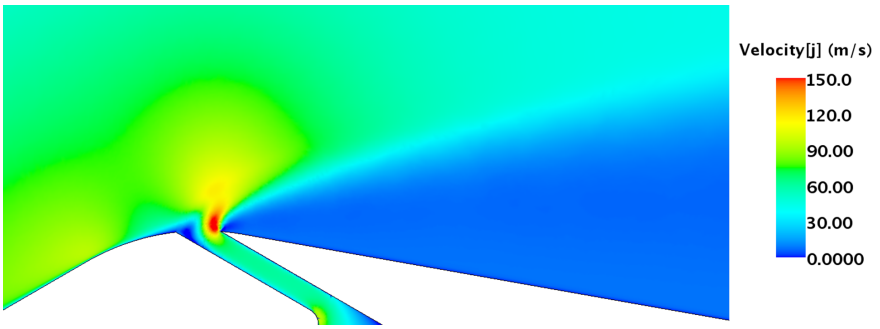

(b) Case 2.E.2

Figure 3.46: Cases 1.E.2 and 2.E.2 vertical component of secondary injection velocity.

The contour plots shows a clear increase in velocity at the exit of the secondary injection geometry for case 1.E.2. This increase in exit velocity results in increased penetration into the core flow which contributes to an increased vector angle. The wall pressure profiles associated with the CFD results for case 2.E.2 are shown in Figure 3.47.

A comparison with case 1.E.2 shows a number of similarities with the general shape of the upper and lower wall pressure profiles. The most noticeable difference is at the peak of the plain wall pressure profile at the junction where the diverging and converging portions of the nozzle meet. This peak is lower and less smooth than in case 1.E.2 and is caused by increased flow separation at this junction. Comparing the CFD results, however, returns similar correlation as with case 1.E.2 and as shown in Figure 3.48.

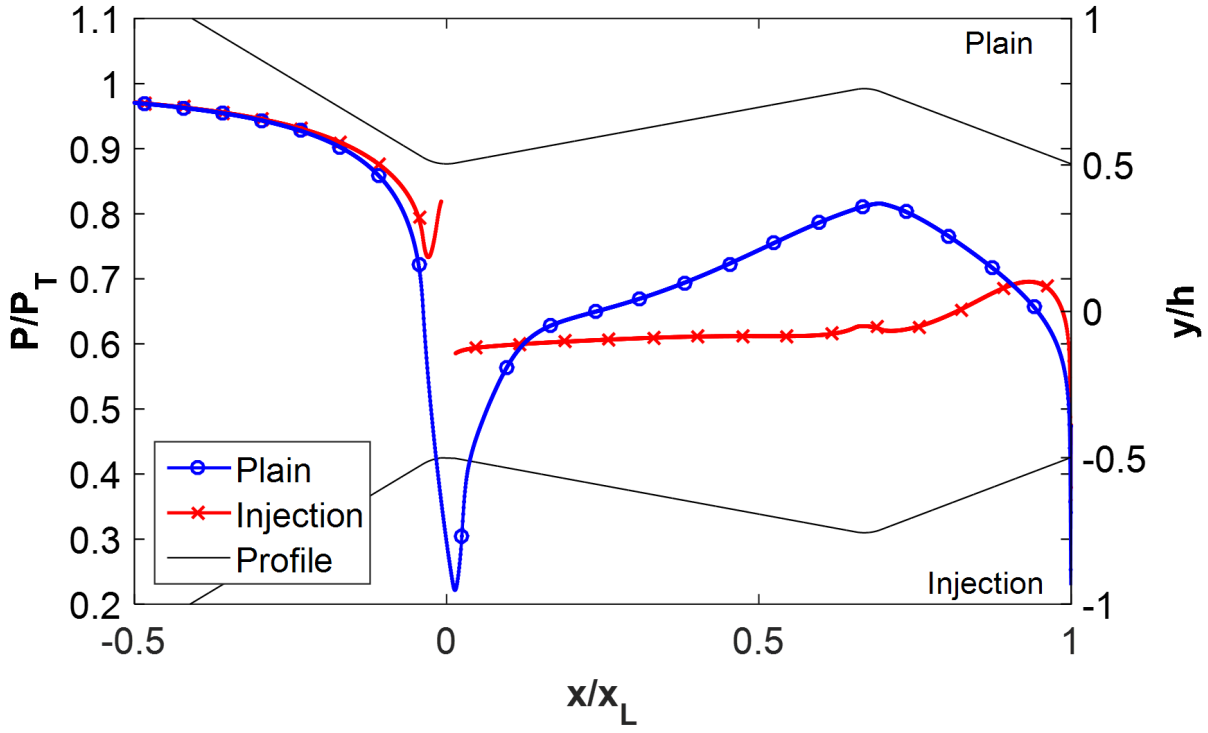

(a) Case 2.E.2 CFD Profile

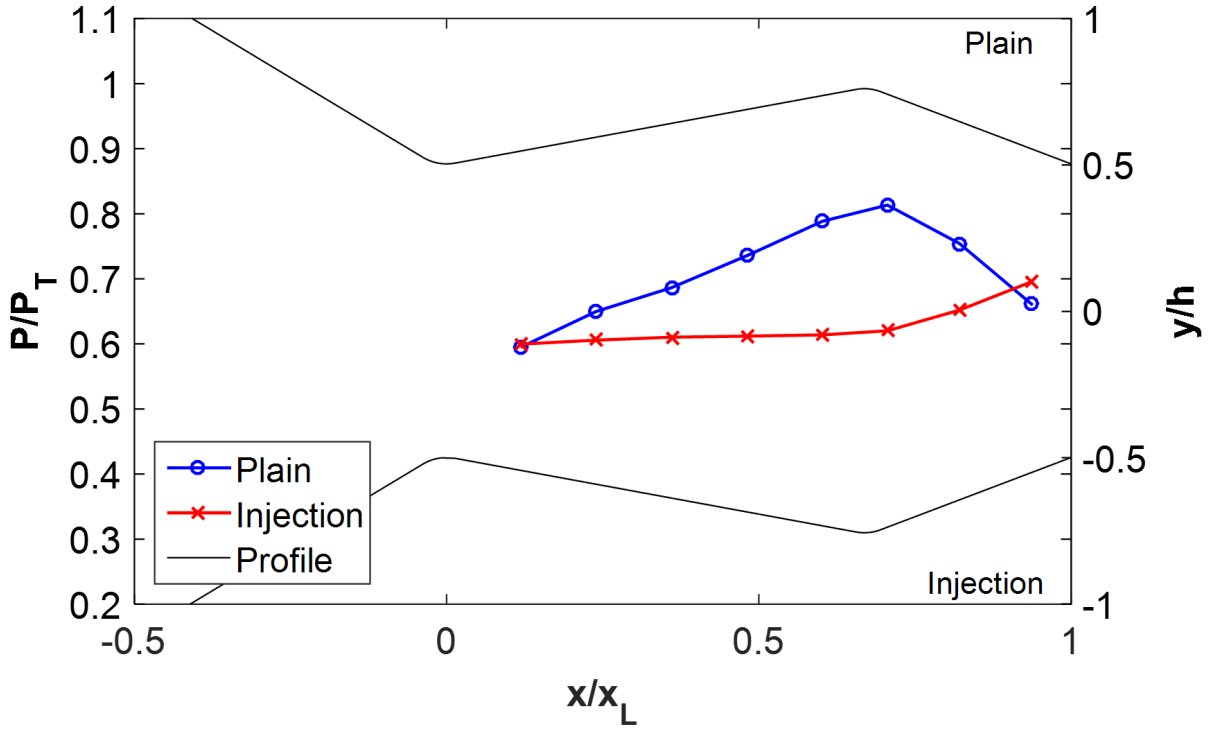

(b) Case 2.E.2 Sampled CFD Profile

Figure 3.47: Case 2.E.2 CFD pressure profiles.

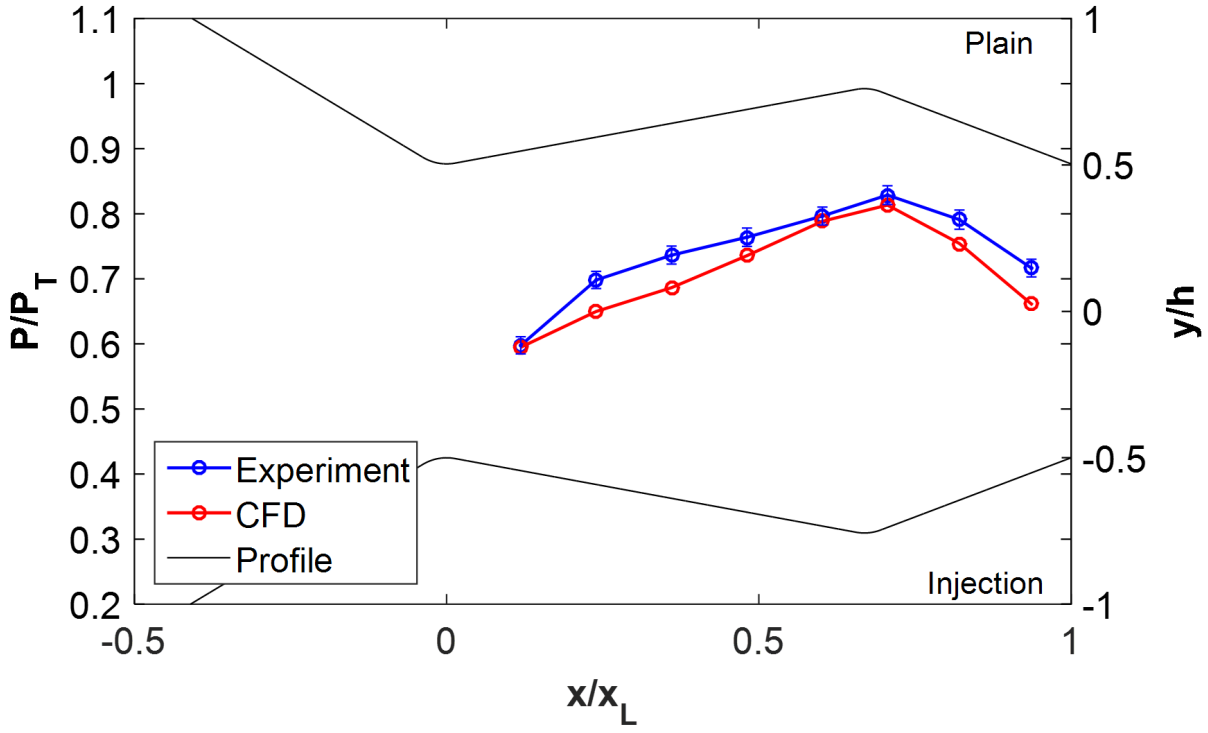

(a) Upper Wall Pressure Profile

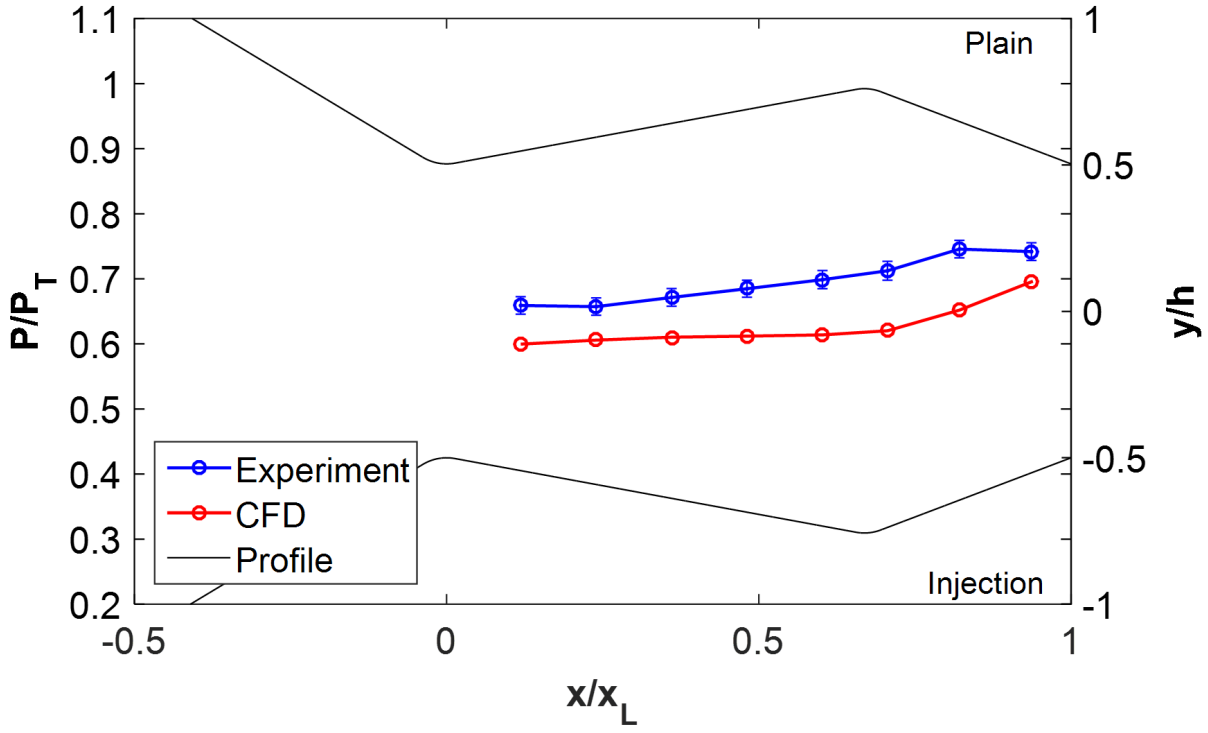

(b) Lower Wall Pressure Profile

Figure 3.48: Case 2.E.2 comparison between experimental and CFD pressure profile.

The upper plain wall CFD pressure profile matches significantly closer to the experimental data than the lower wall does. This is the same trend seen for the other cases, and the reason for the substantial difference of lower wall pressure ratio between the experimental results and CFD is likely due to the poor prediction of flow separation by the K-Epsilon closure model. The trends for the upper plain wall and lower injection wall are predicted well by the CFD as seen in Figure 3.49. However, similar to 1.*.2, the CFD predicts the same progression of the wall pressure profile shapes over a much smaller range of secondary injection than what is seen experimentally.

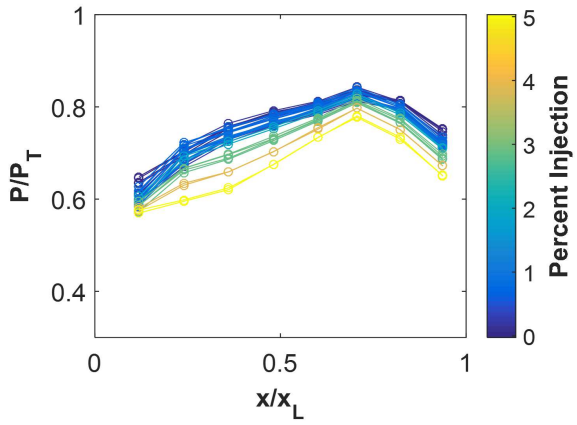

(a) Experimental Upper Wall Pressure Profile Progression

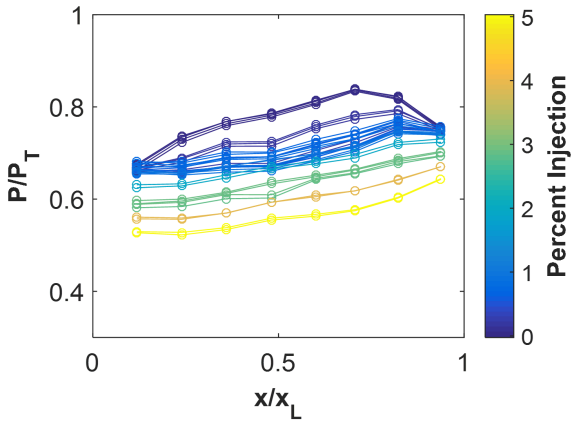

(b) Experimental Lower Wall Pressure Profile Progression

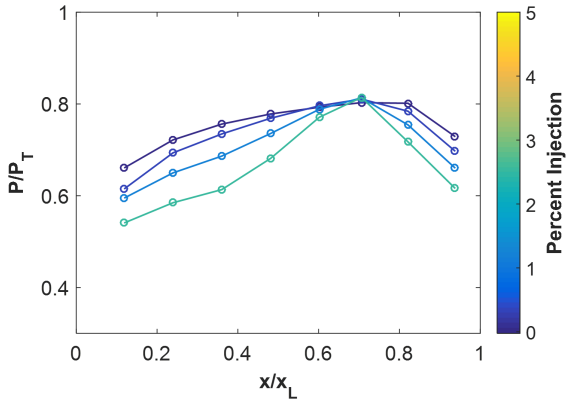

(c) CFD Upper Wall Pressure Profile Progression

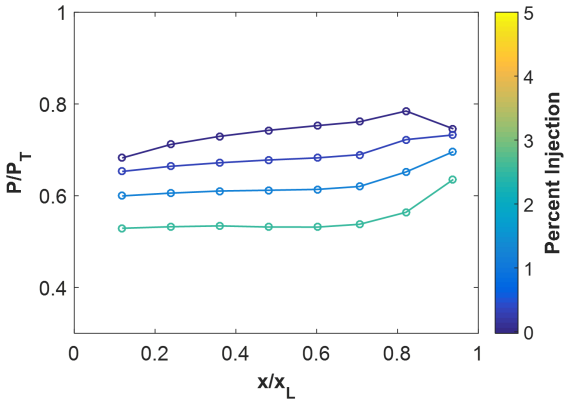

(d) CFD Lower Wall Pressure Profile Progression

Figure 3.49: Case 2.*.2 wall pressure profile progression as a function of injection percentage.

3.4.1.3 Case 3.*.2

The last configuration investigated at a NPR of 2 is case 3.*.2. This geometry is much different from the other cases in that the secondary injection is a series of holes instead of a slot. Because this is inherently a three dimensional geometry, no CFD study was conducted for this case. Figure 3.50 shows the first secondary injection case, 3.B.2.

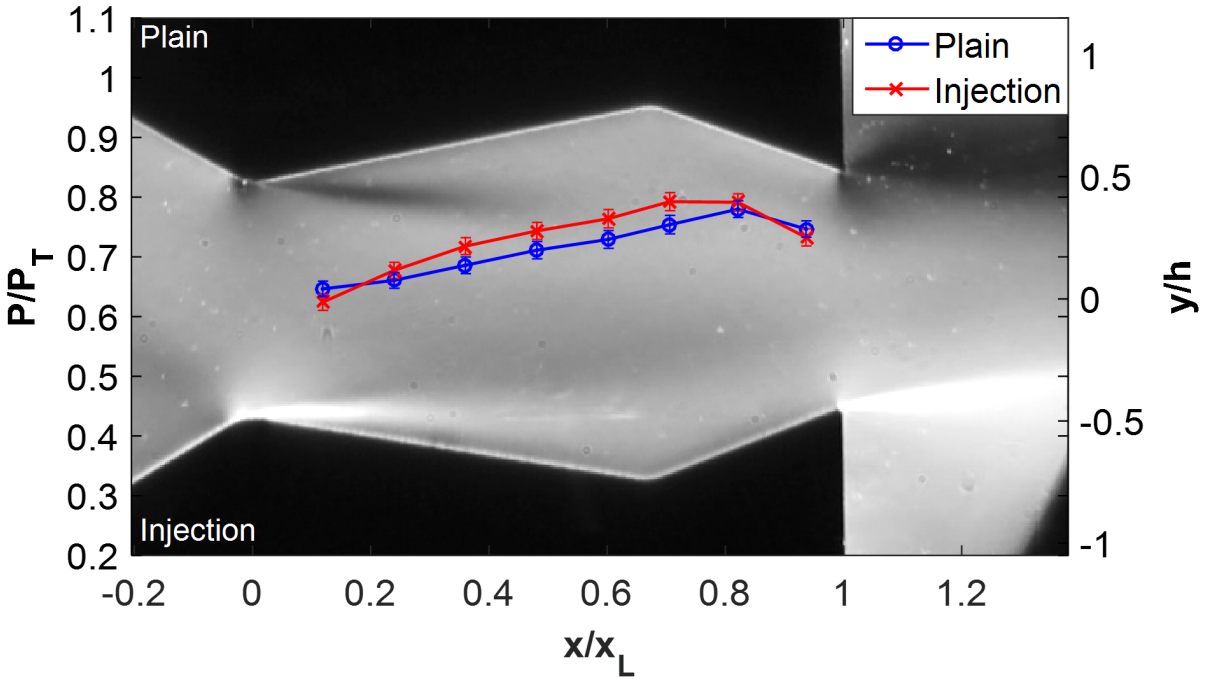

Figure 3.50: Case 3.B.2 schlieren and pressure profile.

As discussed previously, the secondary injection holes were found to have the opposite effect of the secondary injection slot which increased the amount of separation on the lower wall. This wall pressure profile bias for cases 3.*.2 can even be seen with the introduction of secondary injection. Even with 0.2% secondary injection, the wall pressure profiles show more separation along the upper plain wall than lower injection wall. Figures 3.51 through 3.54 show the progression as injection flow rate is increases for cases 3.*.2.

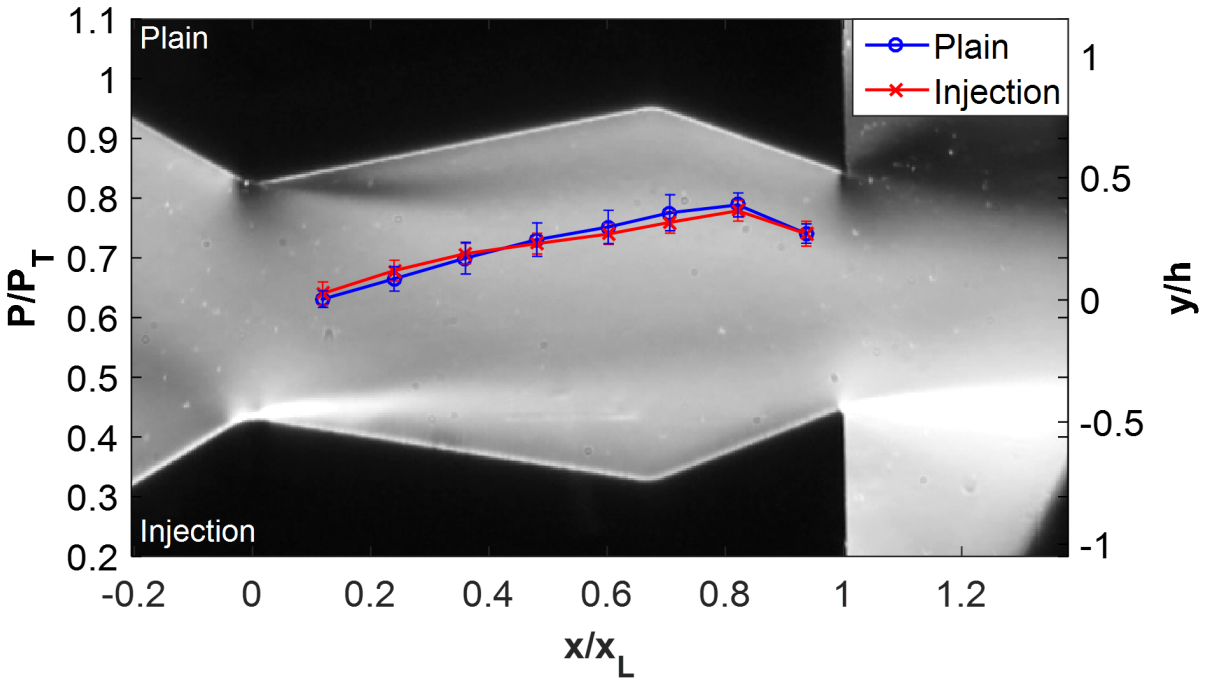

(a) Case 3.C.2

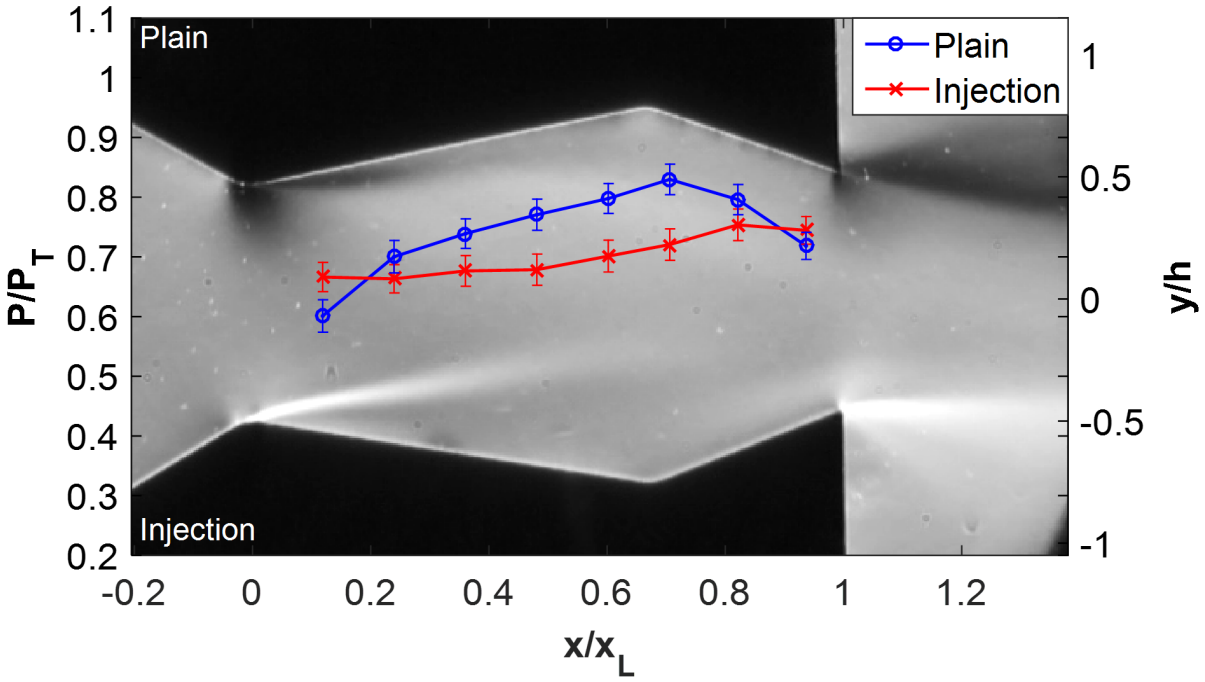

(b) Case 3.D.2

Figure 3.51: Cases 3.C.2 and 3.D.2

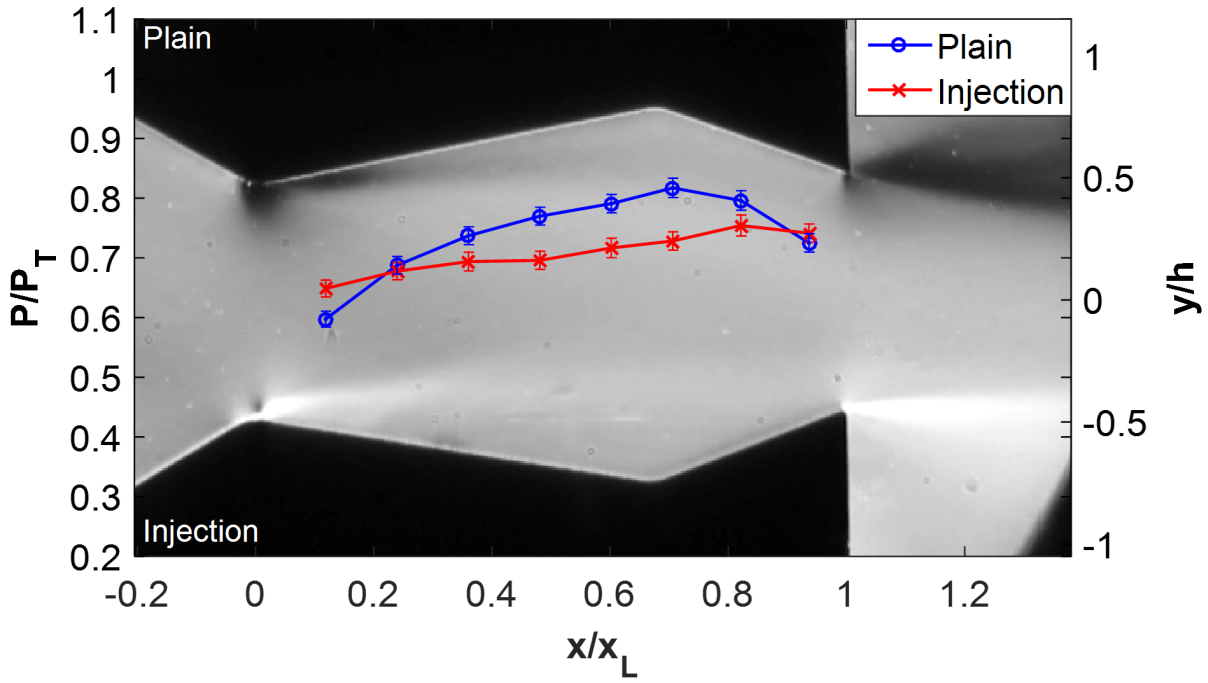

(a) Case 3.E.2

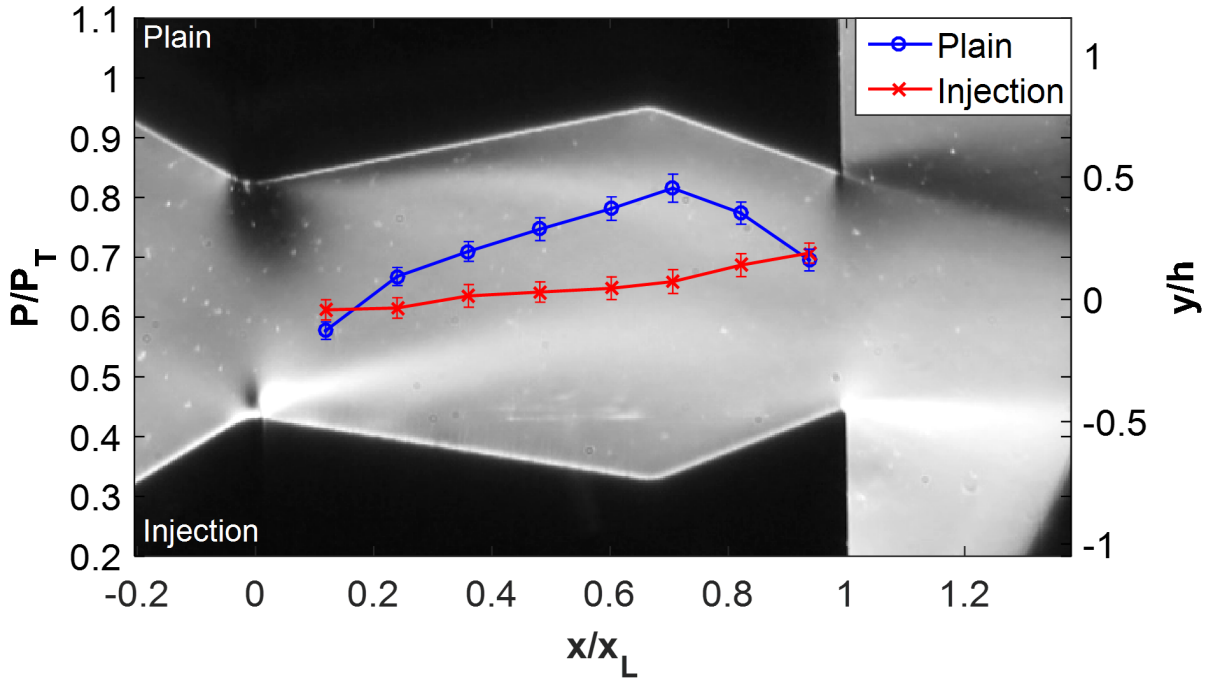

(b) Case 3.F.2

Figure 3.52: Cases 3.E.2 and 3.F.2

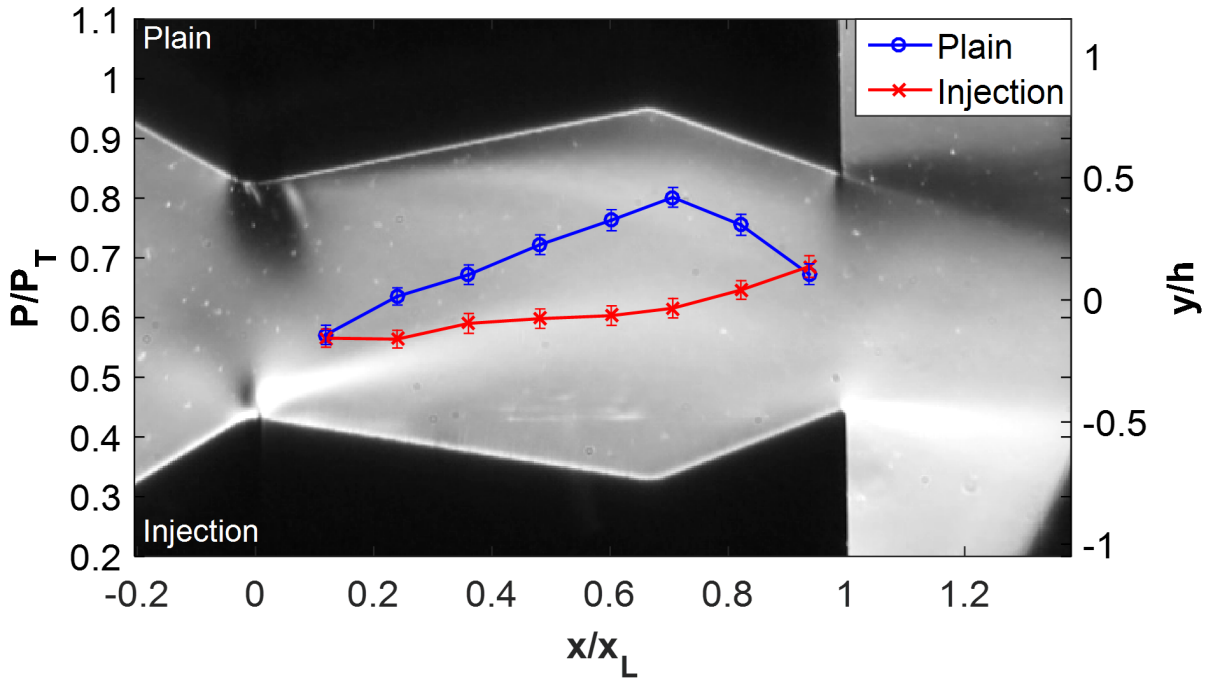

(a) Case 3.G.2

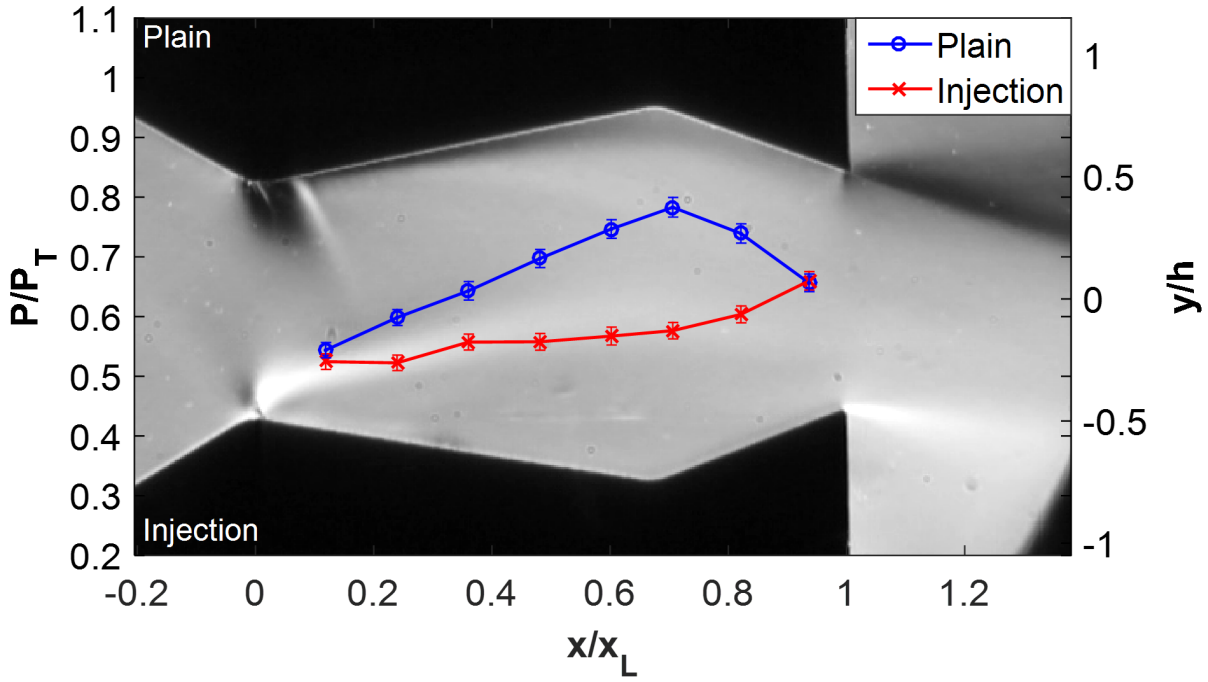

(b) Case 3.H.2

Figure 3.53: Cases 3.G.2 and 3.H.2

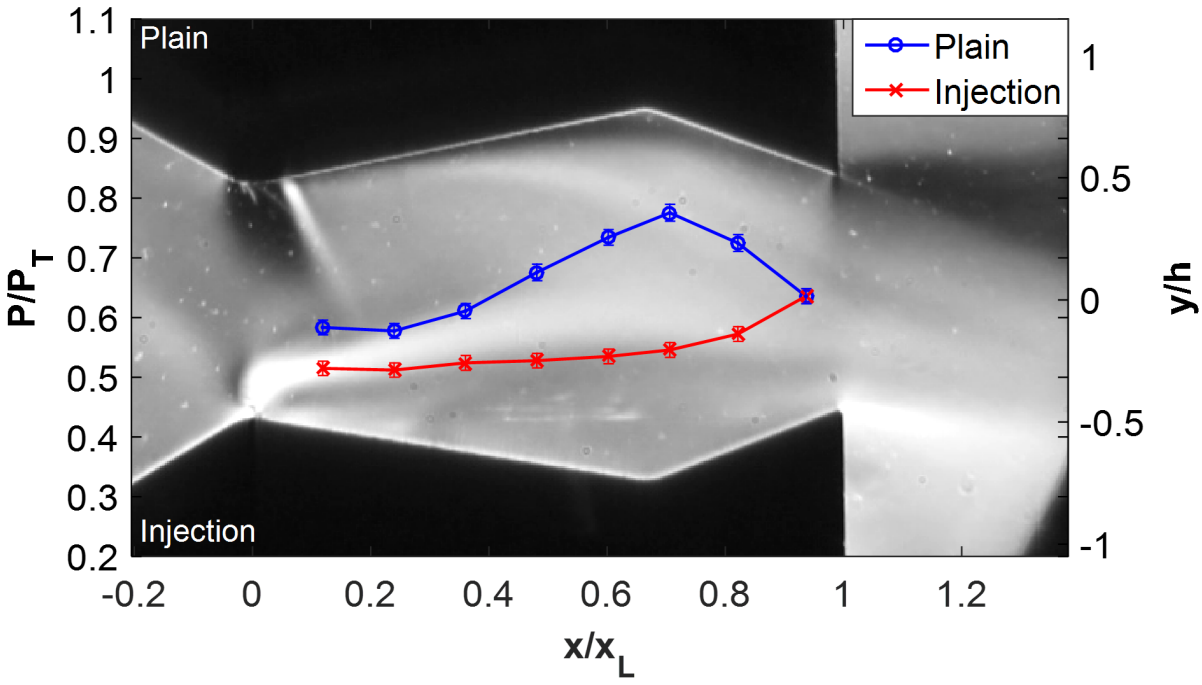

Figure 3.54: Case 3.I.2

It can be seen through the progression of wall pressure profiles that at high enough secondary injection mass flow rates, the bias induced from the injection hole geometry is overcome and a positive thrust-vector angle is generated. Additionally, the same upper wall shock phenomena seen the both of the previous test cases actually occurs at a similar injection percentage as case 2.*.2. The progression of the wall profiles is seen in Figure 3.55.

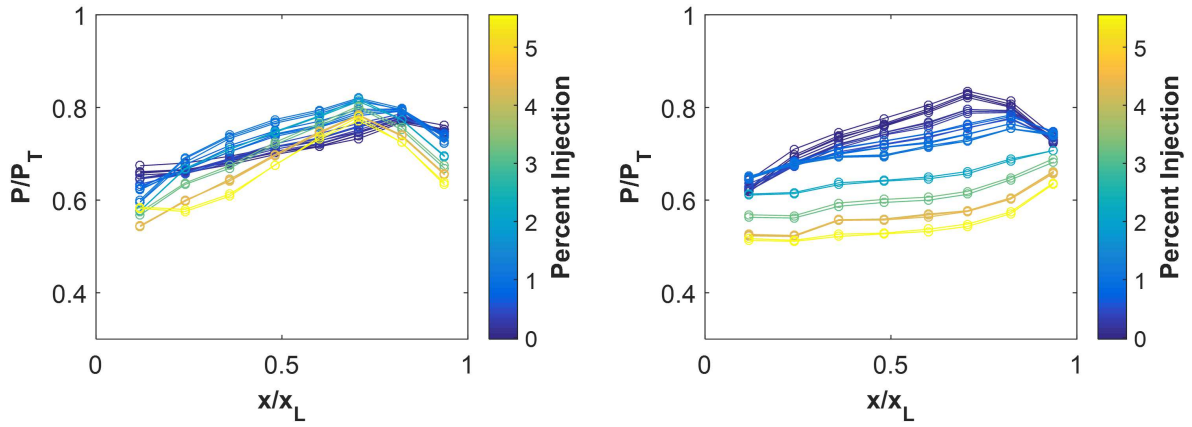

(a) Upper Wall Pressure Profile Progression

(b) Lower Wall Pressure Profile Progression

Figure 3.55: Case 3.*.2 wall pressure profile progression as a function of injection percentage.

The progression of wall pressure profiles for case 3.*.2 is unique since the upper plain wall and lower injection wall both show the opposite progression of wall pressure profiles for injection percentages between approximately 0 and 2%.

3.4.2 Nozzle Pressure Ratio of 4

A set of tests were performed at a NPR of 4 for all three of the nozzle configurations. Due to the same pressure limit on the secondary mass flow controller, the flow rates tested were similar to the flow rates used for the NPR of 2 cases, however, the core flow mass flow rate roughly doubled which decreased the secondary injection percentage. Additionally, due to time constraints, CFD was only conducted on two secondary injection cases. Table 3.3 shows the tests conducted for each configuration for a NPR of 4.

Table 3.3: Secondary Injection NPR = 4 Test Cases

	Case 1.*.4	Case 2.*.4	Case 3.*.4
Lower Test Insert	V1	V2	V3
Upper Test Insert	Plain	Plain	Plain
NPR	4	4	4
Case *.B.4	0.20% (0.167 $\frac{g}{s}$)	0.24% (0.225 $\frac{g}{s}$)	0.48% (0.403 $\frac{g}{s}$)
Case *.C.4	0.50% (0.405 $\frac{g}{s}$)	0.42% (0.398 $\frac{g}{s}$)	0.96% (0.807 $\frac{g}{s}$)
Case *.D.4	0.77% (0.625 $\frac{g}{s}$)	0.67% (0.634 $\frac{g}{s}$)	1.23% (1.01 $\frac{g}{s}$)
Case *.E.4	0.99% (0.813 $\frac{g}{s}$)	0.87% (0.817 $\frac{g}{s}$)	1.47% (1.23 $\frac{g}{s}$)
Case *.F.4	1.29% (1.03 $\frac{g}{s}$)	1.07% (1.03 $\frac{g}{s}$)	1.73% (1.44 $\frac{g}{s}$)
Case *.G.4	1.53% (1.22 $\frac{g}{s}$)	1.31% (1.25 $\frac{g}{s}$)	2.20% (1.81 $\frac{g}{s}$)
Case *.H.4	1.81% (1.46 $\frac{g}{s}$)	1.94% (1.85 $\frac{g}{s}$)	N/A
Case *.I.4	N/A	2.38% (2.25 $\frac{g}{s}$)	N/A

3.4.2.1 Case 1.*.4

Beginning with case 1.*.4, test cases were conducted at secondary injection mass flow rates ranging from 0.2 to 1.83% of the core flow mass flow rate. Figure 3.56 below shows the first case 1.B.4.

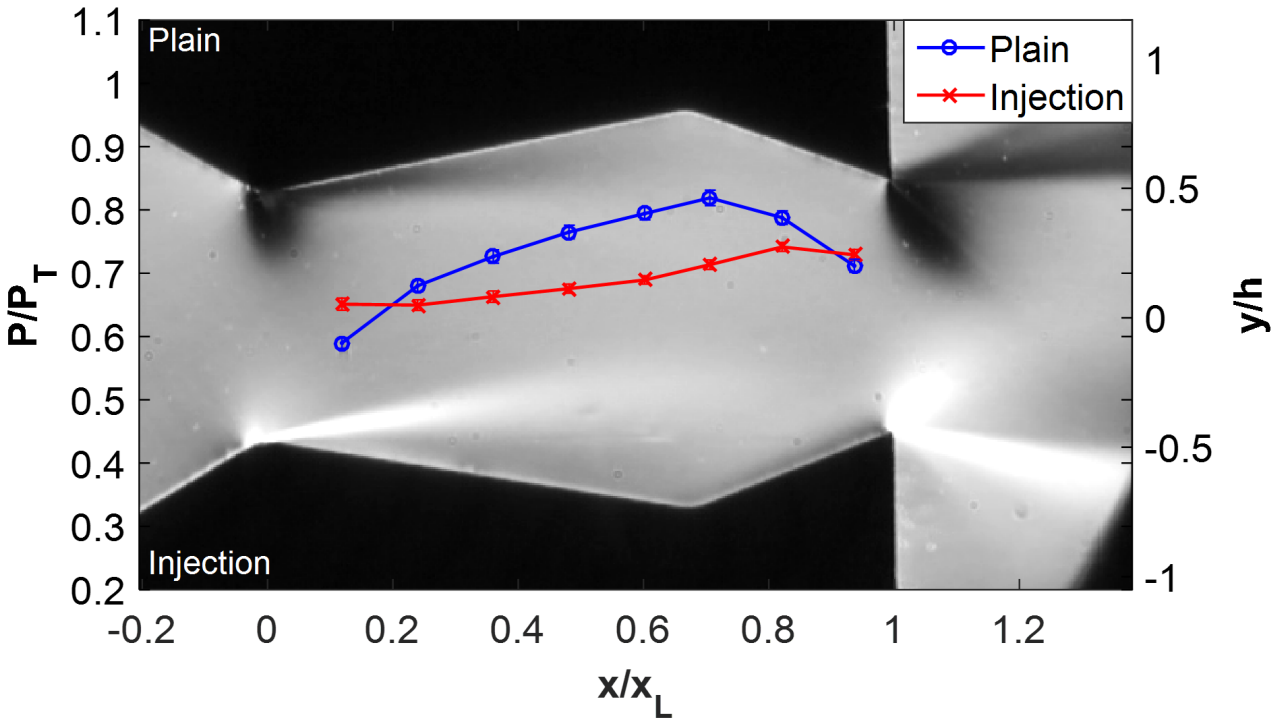

Figure 3.56: Case 1.B.4 schlieren and pressure profile.

The most notable feature of the pressure profiles is their similarity to the 1.B.2 case with almost exact agreement at each pressure tap. This similar performance is expected since the ratio of secondary mass flow rate to core mass flow rate is comparable between the two cases. Figure 3.57 through 3.59 shows the progression for the remaining test cases.

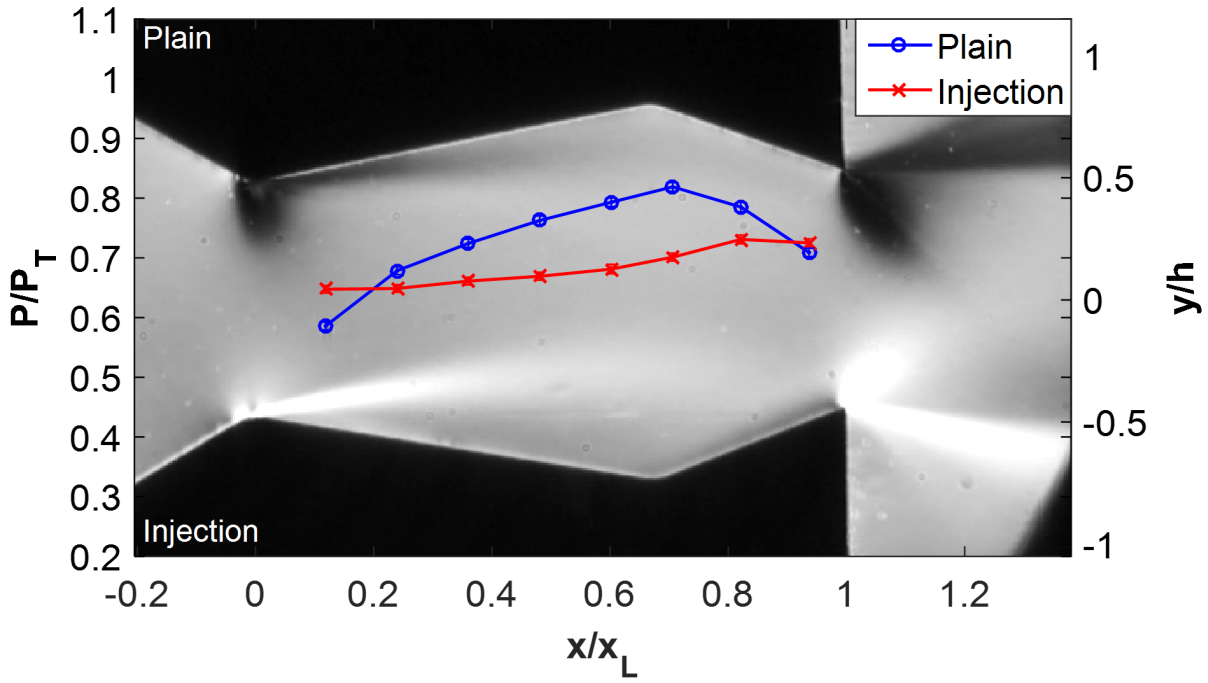

(a) Case 1.C.4

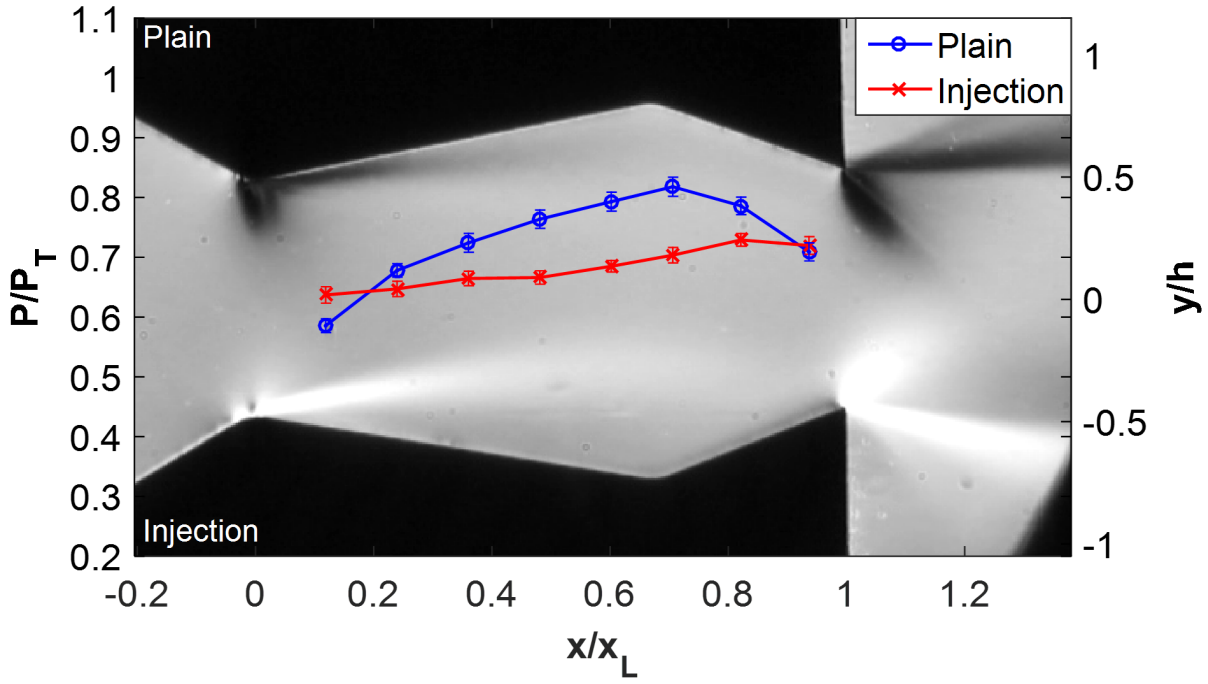

(b) Case 1.D.4

Figure 3.57: Cases 1.C.4 and 1.D.4

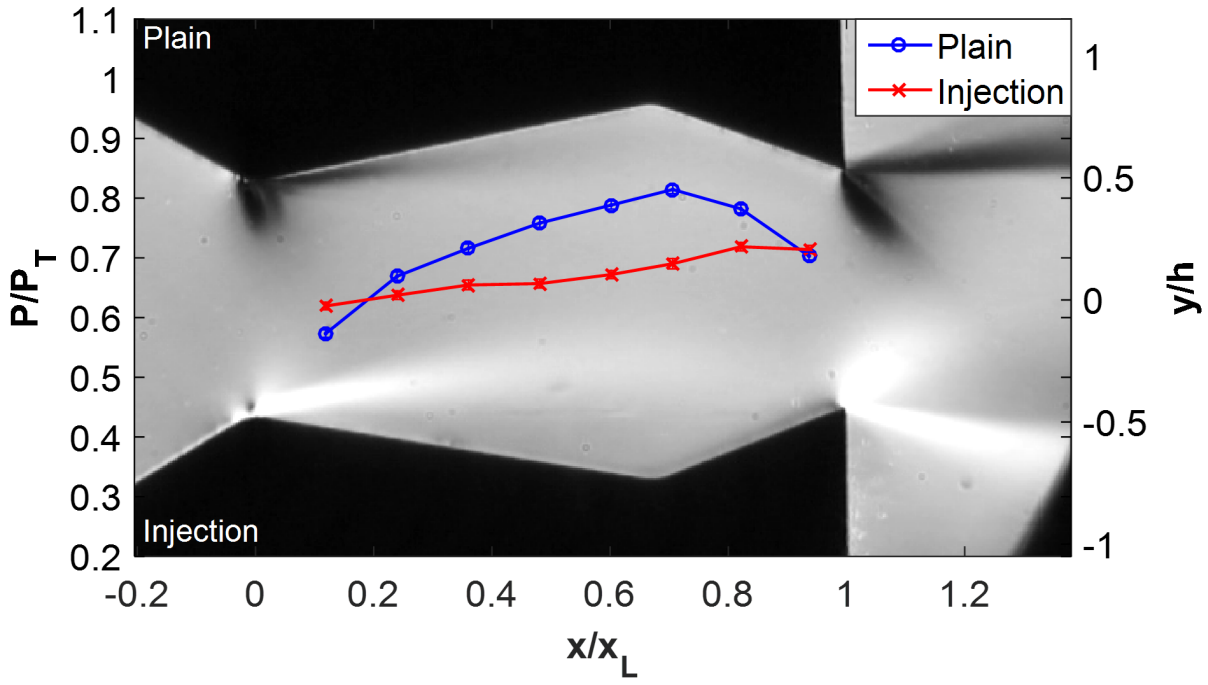

(a) Case 1.E.4

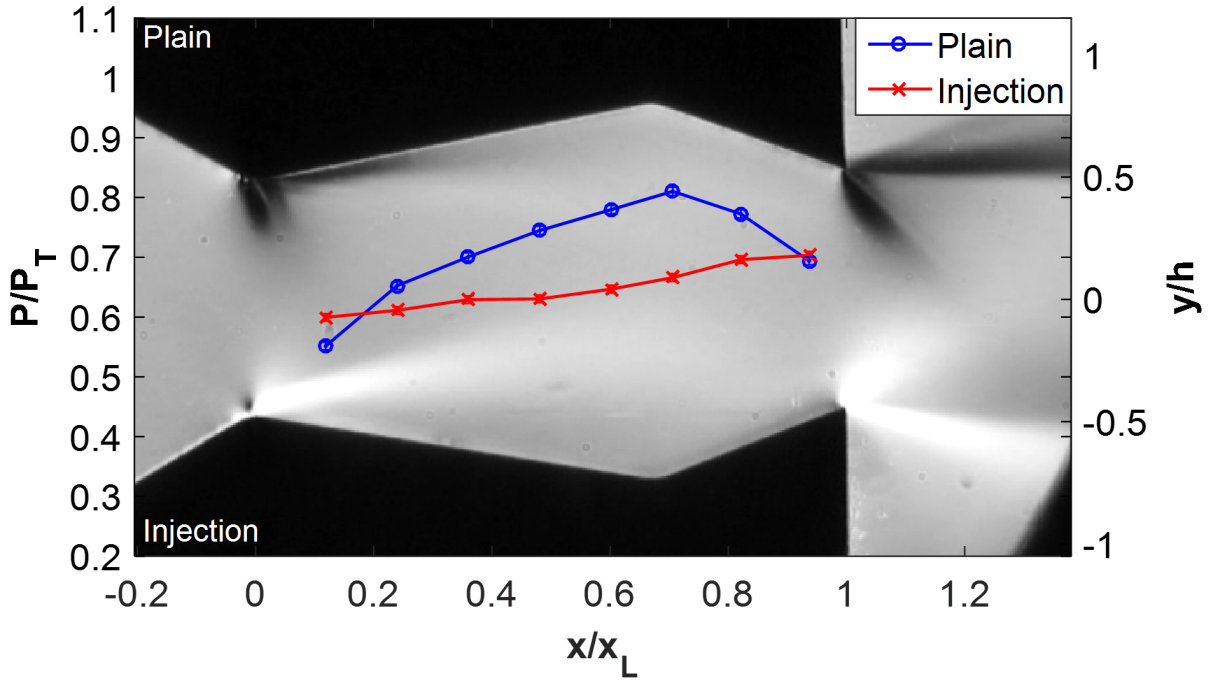

(b) Case 1.F.4

Figure 3.58: Cases 1.E.2 and 1.F.2

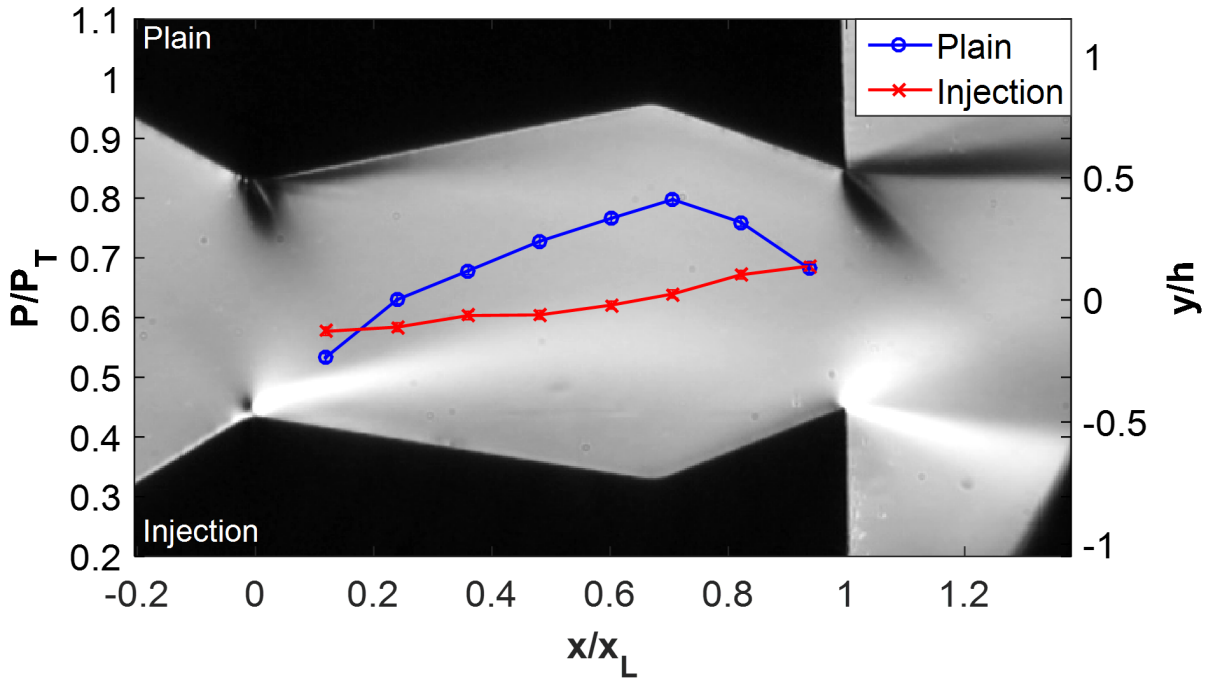

(a) Case 1.G.4

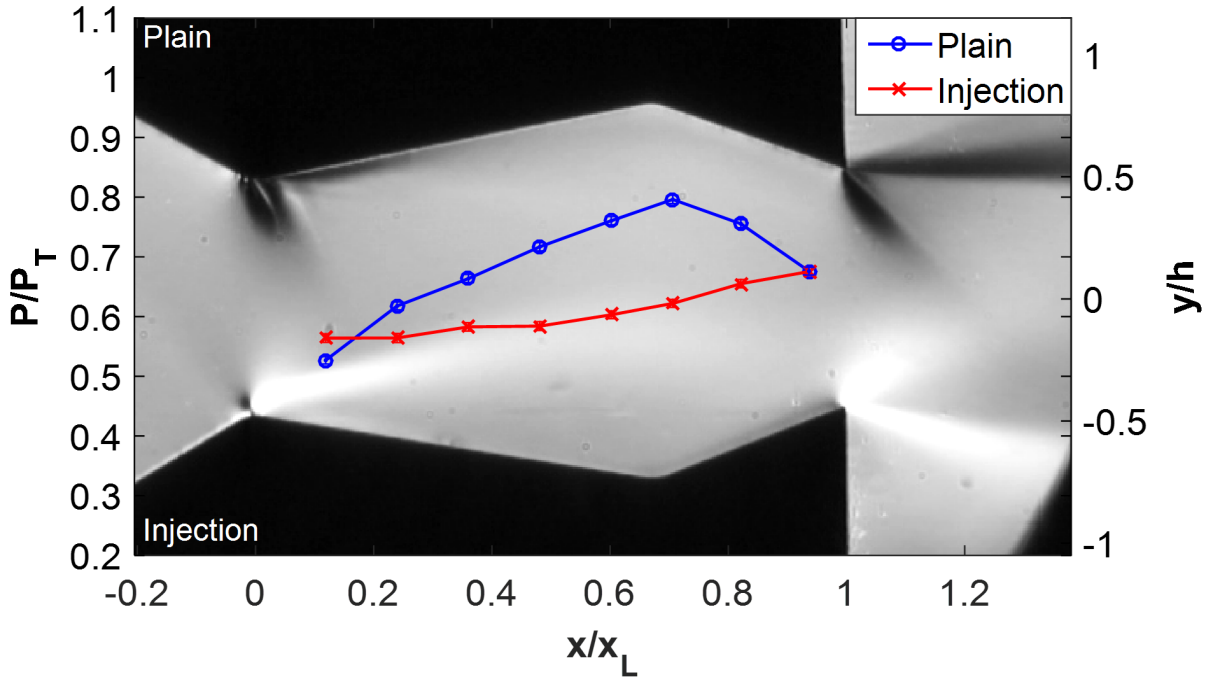

(b) Case 1.H.4

Figure 3.59: Cases 1.G.4 and 1.H.4

The progression of wall pressure profiles bears similar results to that of the 1.*.2 cases. Additionally, the development of the shock on the upper plain wall occurs at 1.H.4, a similar secondary injection percentage at which it first occurs in case 1.F.2. An overlayed progression of wall pressure profiles is shown in Figure 3.60.

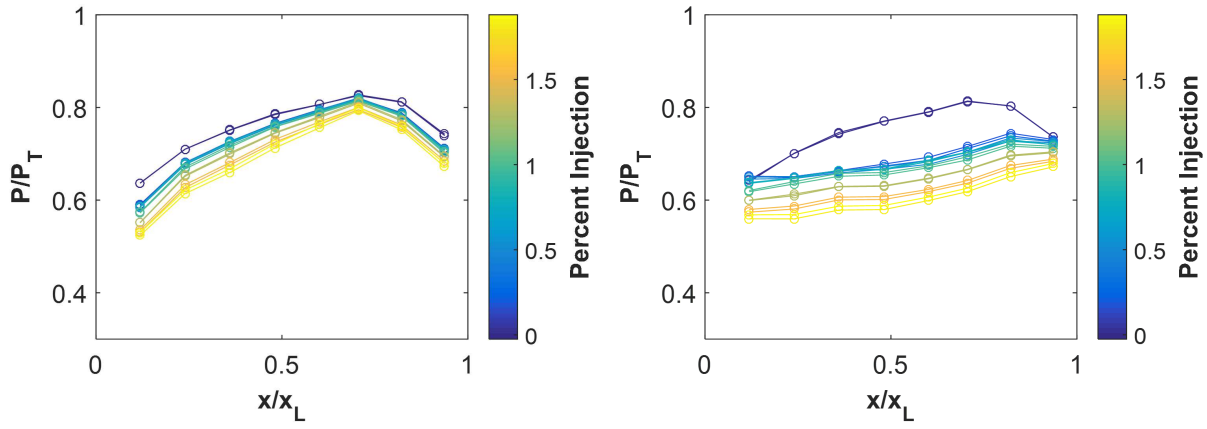

(a) Upper Wall Pressure Profile Progression

(b) Lower Wall Pressure Profile Progression

Figure 3.60: Case 1.*.4 wall pressure profile progression as a function of injection percentage.

A distinct difference that was seen between the 1.*.2 and 1.*.4 cases was a significantly more expanded pressure profile along the upper and lower wall for the higher NPR 1.*.4 case. The progression of both of the wall pressure profiles are seen to show a clear decreasing trend with an increase in injection percentage.

3.4.2.2 Case 2.*.4

The second test case at a NPR of 4 was conducted at similar injection percentages, but required noticeably different secondary injection mass flow rates compared to case 1.*.4. The larger secondary mass flow rate required was due to the lower penetration of the secondary injection jet produced by this geometry, which resulted in a larger primary throat area and higher core flow mass flow rate. Figure 3.61 shows the results of test case 2.B.4.

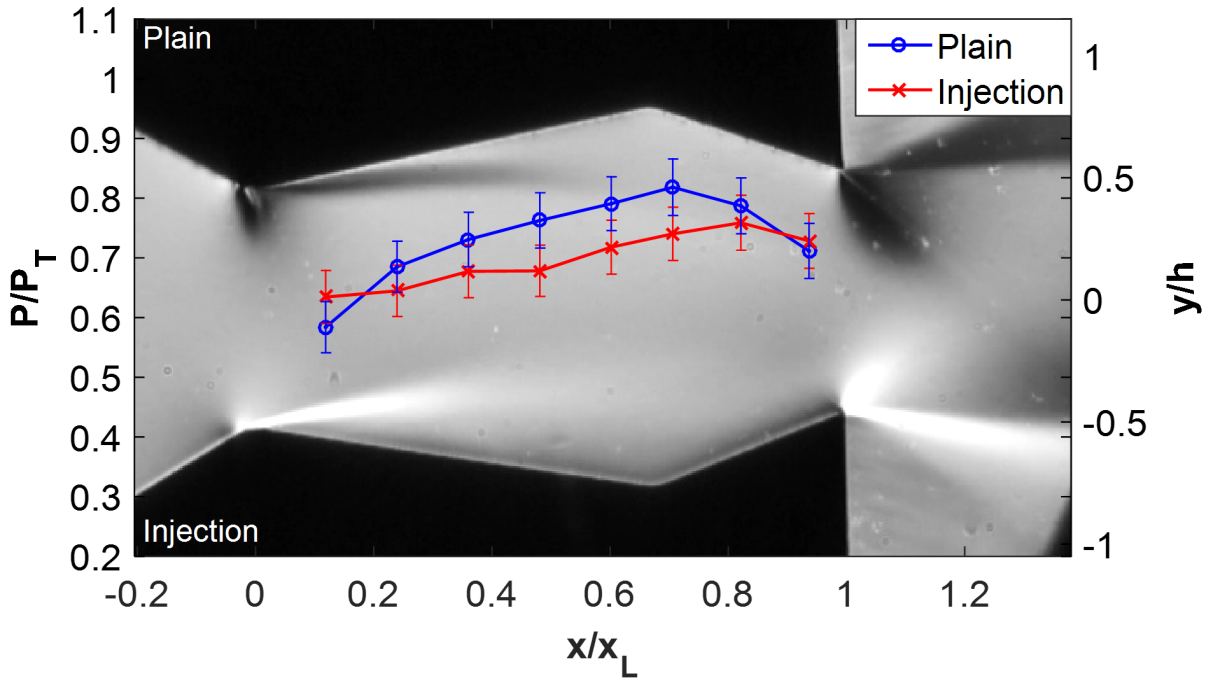

Figure 3.61: Case 2.B.4 schlieren and pressure profile.

This test case resulted in abnormally high error bounds, a problem that was also seen in the 2.*.2 case. Transient behavior at startup was seen as a likely cause for this unpredictability with oscillatory behavior similar to that presented in Figure 3.40. An increase in secondary mass flow rate, however, resulted in more stable behavior as seen in the following progression in Figures 3.62 through 3.65.

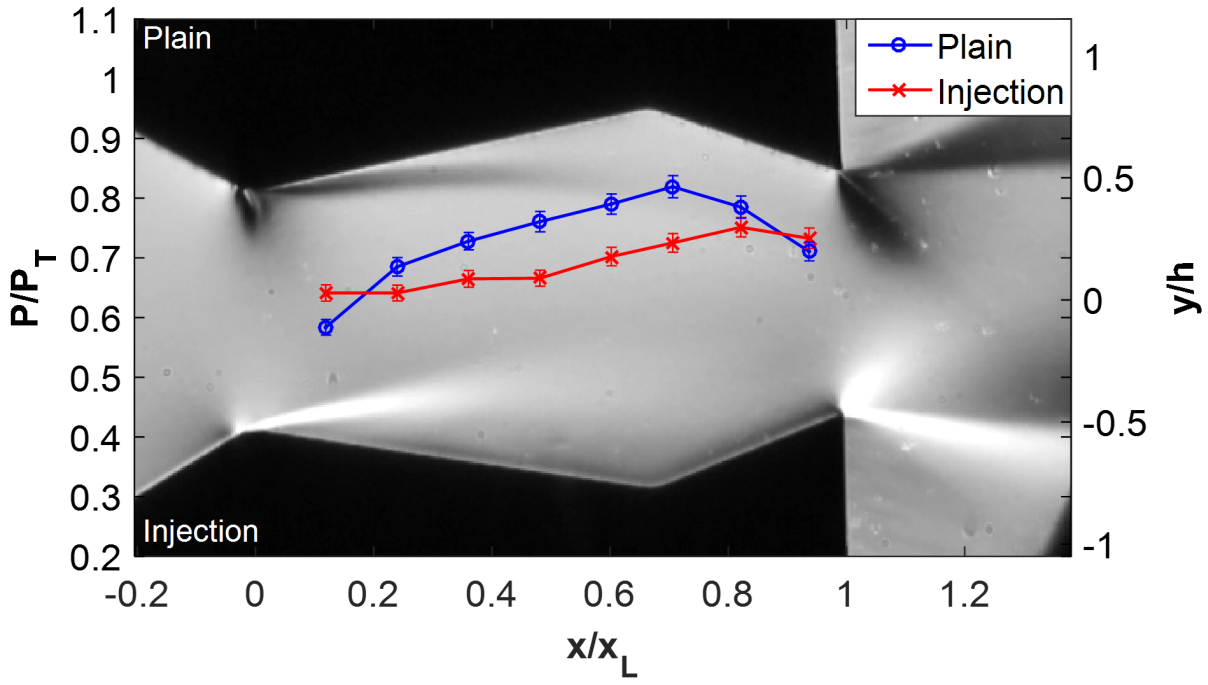

(a) Case 2.C.4

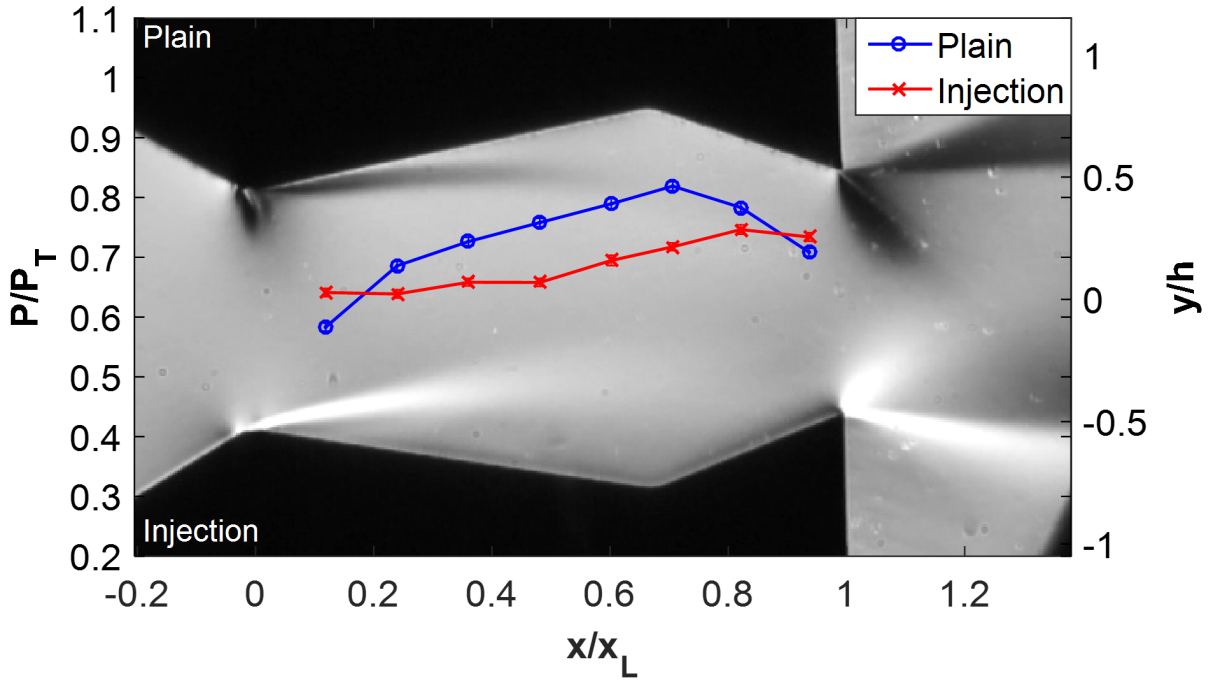

(b) Case 2.D.4

Figure 3.62: Cases 2.C.4 and 2.D.4

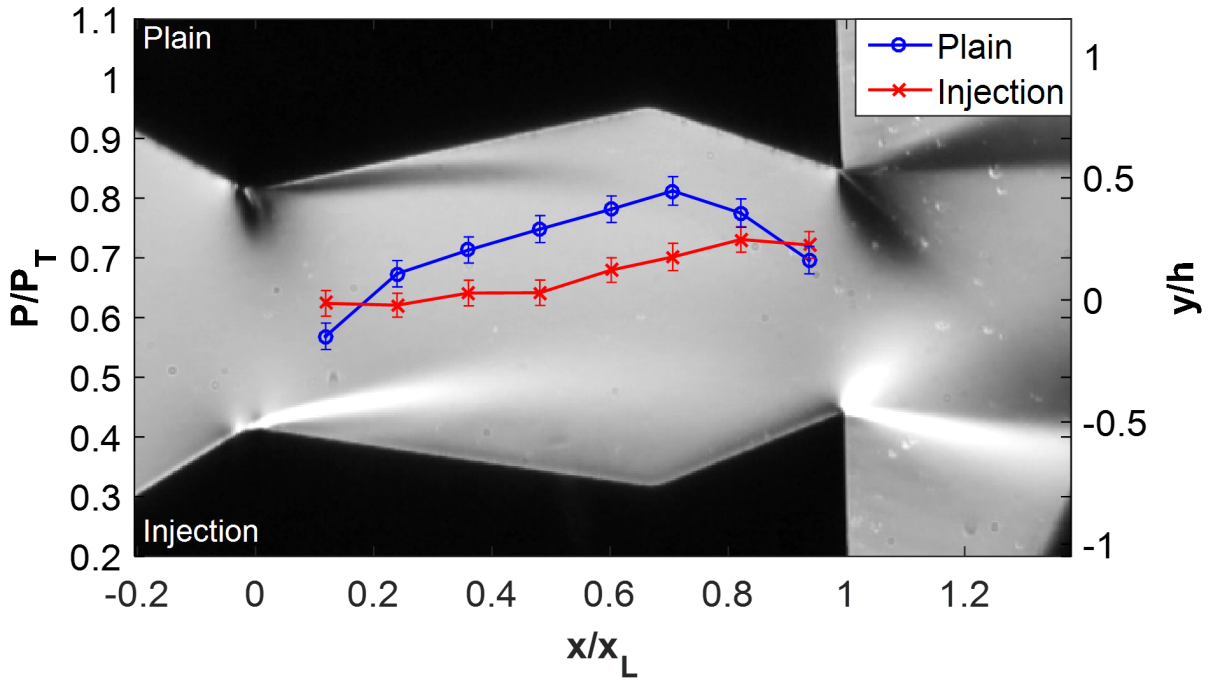

(a) Case 2.E.4

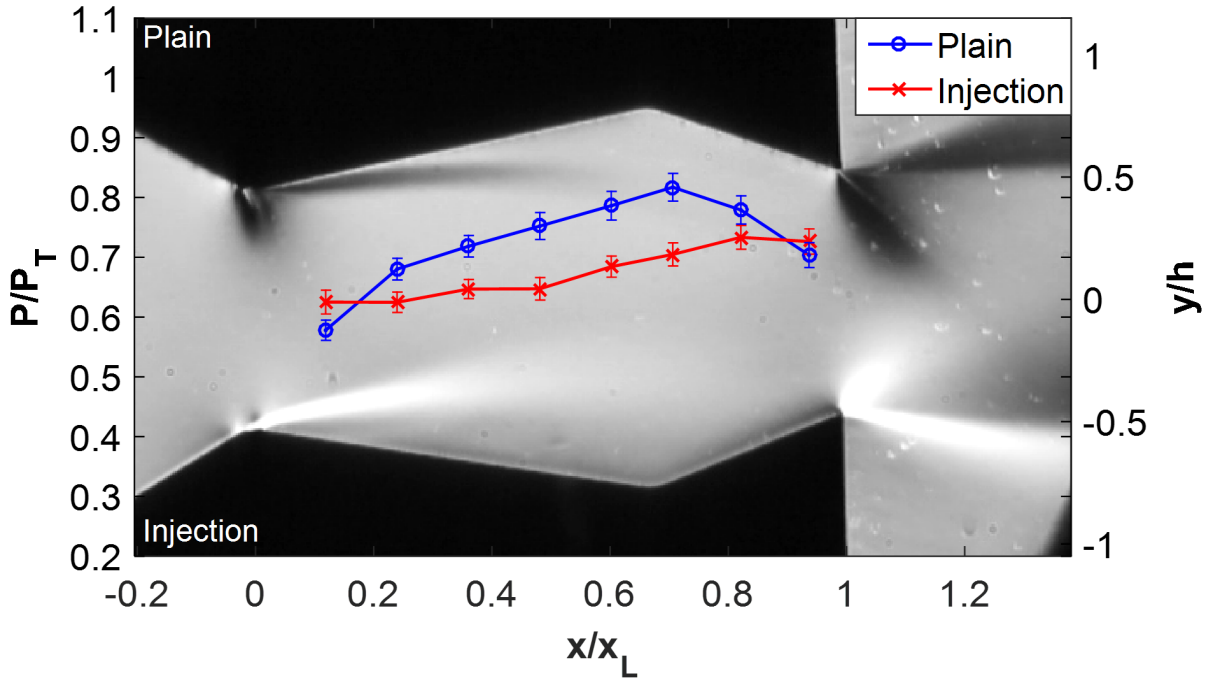

(b) Case 2.F.4

Figure 3.63: Cases 2.E.2 and 2.F.2

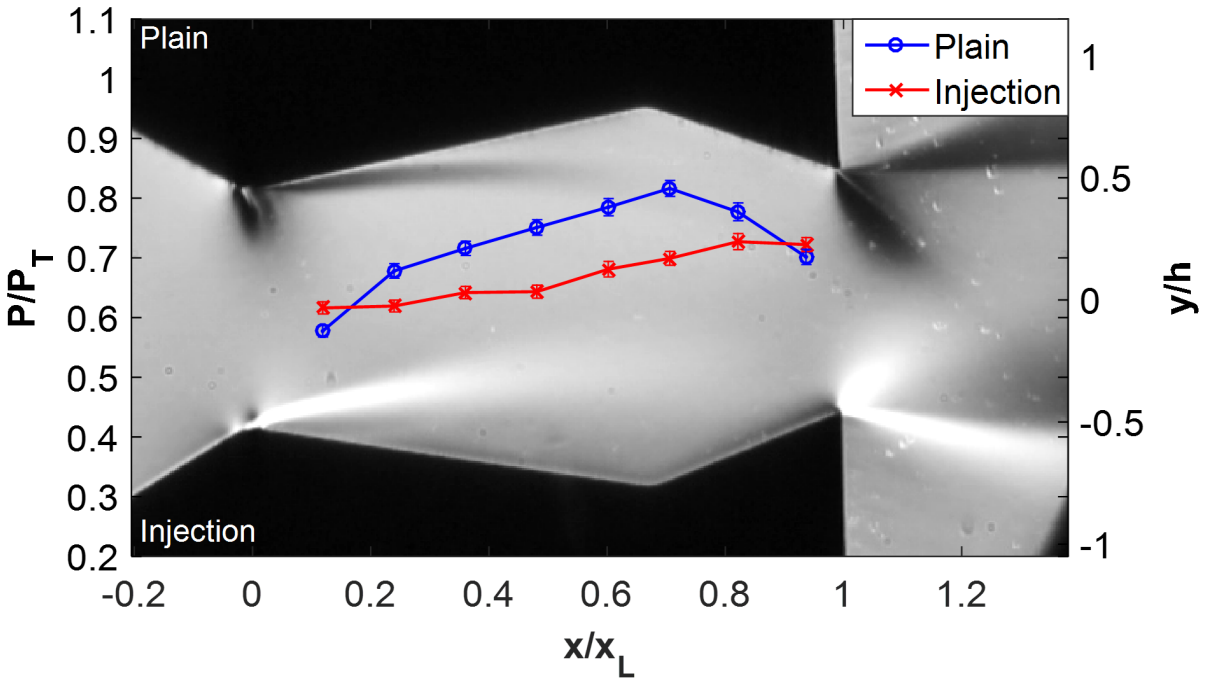

(a) Case 2.G.4

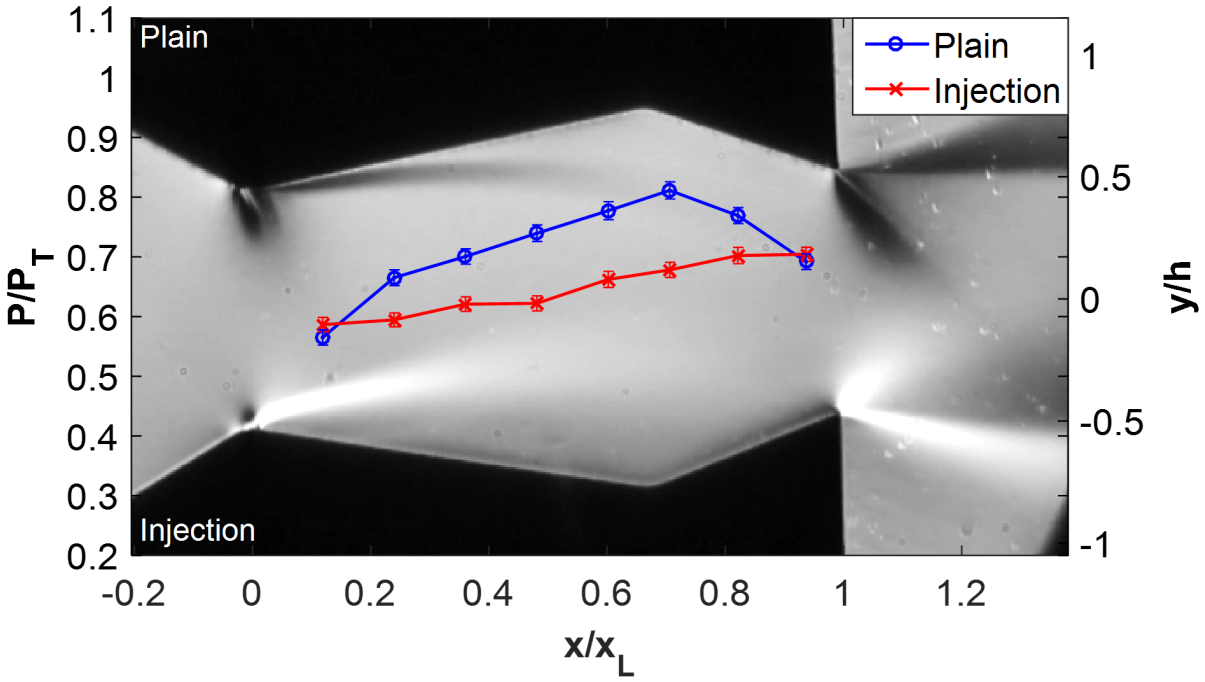

(b) Case 2.H.4

Figure 3.64: Cases 2.G.4 and 2.H.4

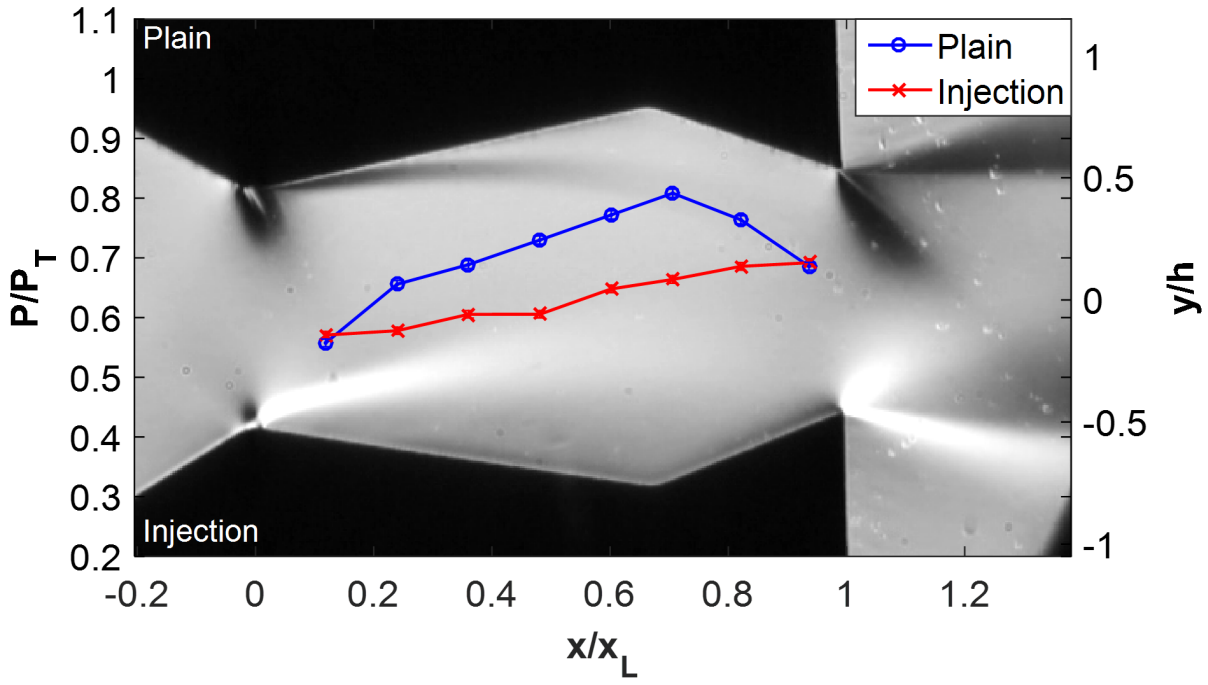

Figure 3.65: Case 2.I.4

As expected based on results from case 2.*.2, the development of a shock on the upper wall did not occur over this range of secondary injection percentages. However, a noticeable feature of this case is the shape of the lower injection pressure profile between the third and fifth pressure tap. The droop between these two pressure taps is apparent throughout the range of secondary injection percentages tested, and can also seen in cases 2.B.2 through 2.D.2. This irregularity suggests that the either the V2 secondary injection geometry is generating a slightly different recirculation region compared to V1 and V3, or a burr or other pressure tap defect on the insert is generating this lower pressure. Manufacturing and testing another nozzle insert would be necessary to further isolate the cause. The progression of the wall pressure profiles for this case is shown in Figure 3.66.

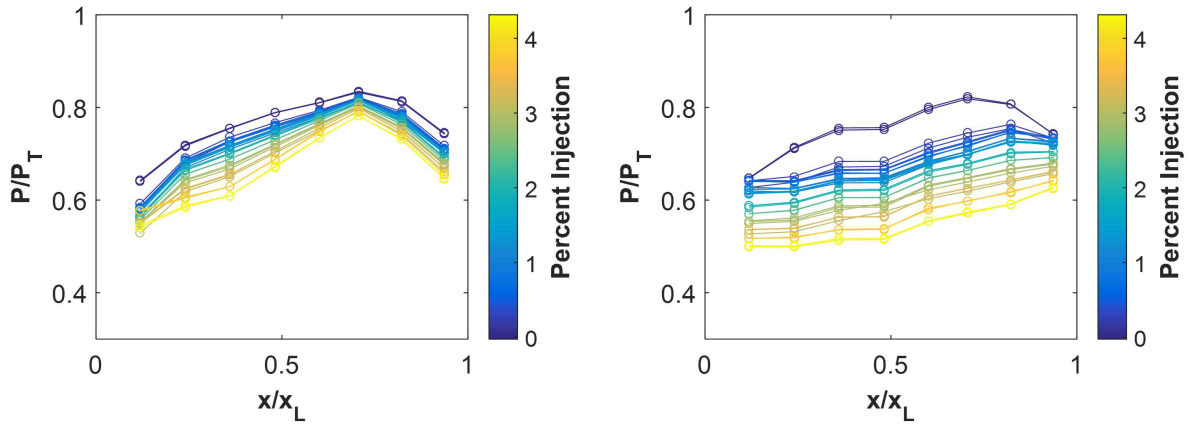

(a) Upper Wall Pressure Profile Progression

(b) Lower Wall Pressure Profile Progression

Figure 3.66: Case 2.*.4 wall pressure profile progression as a function of injection percentage.

The step-like feature described previously can be seen on the lower injection wall pressure profile throughout the range of injection percentages tested. However, the remaining features of pressure profiles are very similar to the trends seen in the previous 1.*.4 case.

3.4.2.3 Case 3.*.4

The final case tested is the case which employed holes as its secondary injection geometry. Unlike cases 3.*.2 where a significant reattachment phenomena was seen along the lower injection wall, the high pressure ratio of case 3.*.4 appeared to negate this effect. Figure 3.67 shows case 3.B.4.

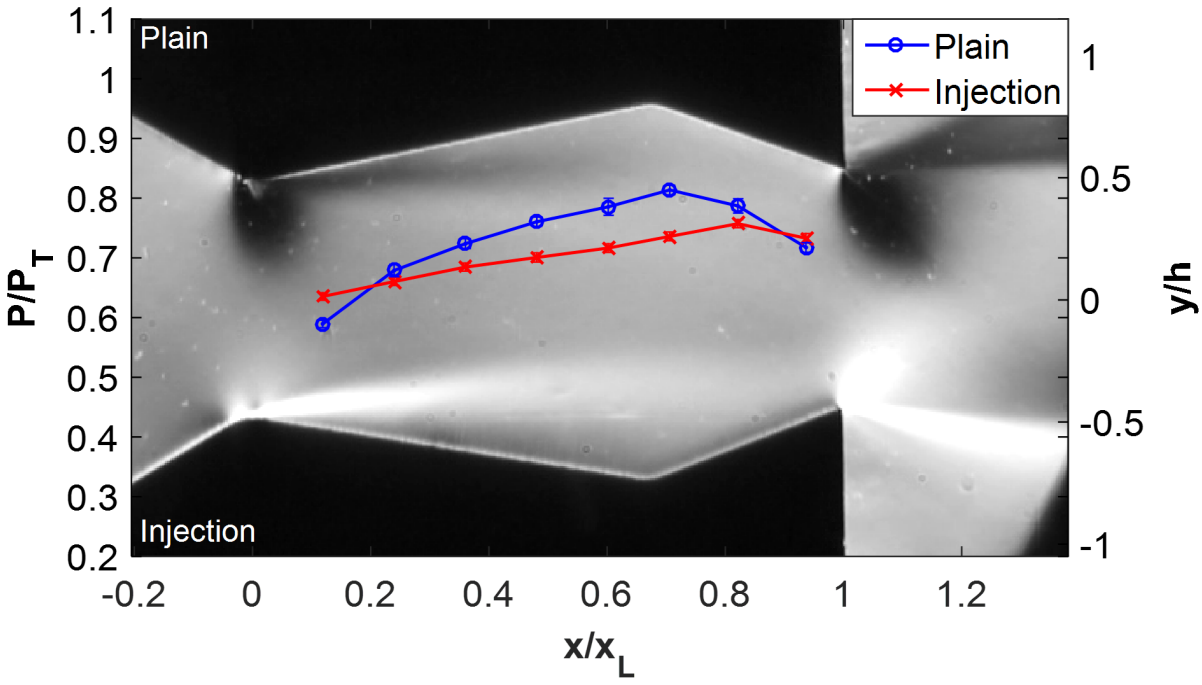

Figure 3.67: Case 3.B.4 schlieren and pressure profile.

Unlike in the 3.B.2 case, the pressure profiles show increased separation along the lower injection wall with a larger degree of attachment along the upper plain wall resulting in pressure profiles similar to the 1.*.4 and 2.*.4 cases. Figures 3.68 through 3.70. show the progression for the remaining 3.*.4 cases.

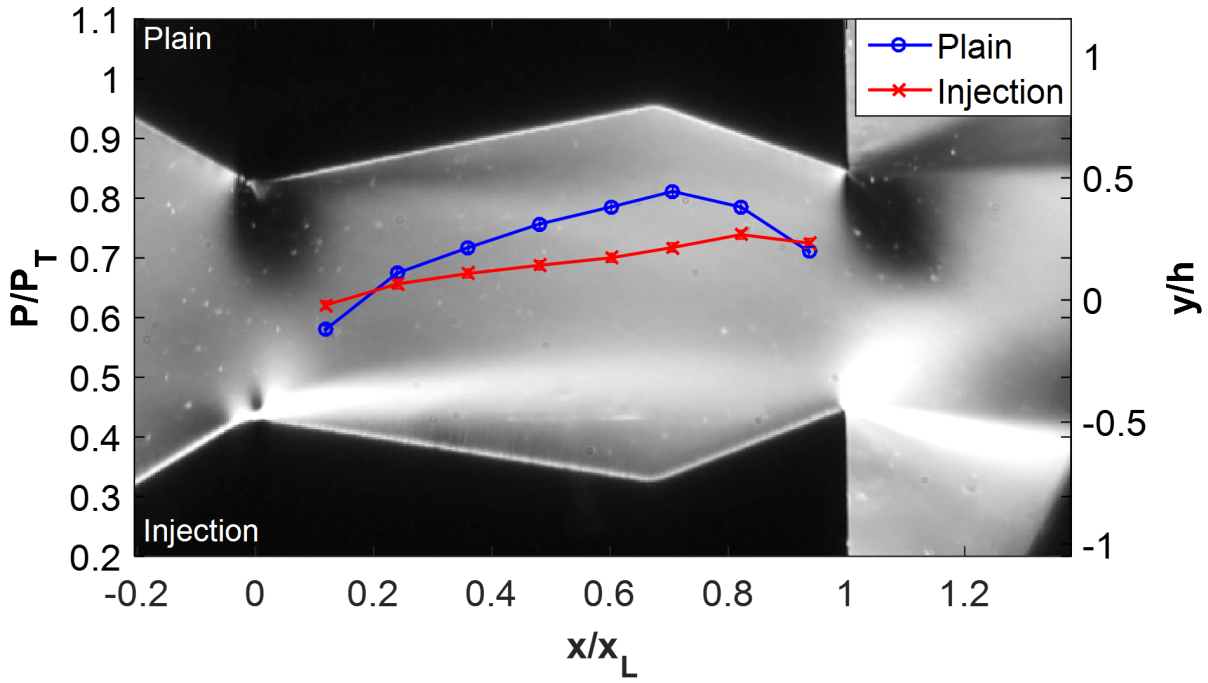

(a) Case 3.C.4

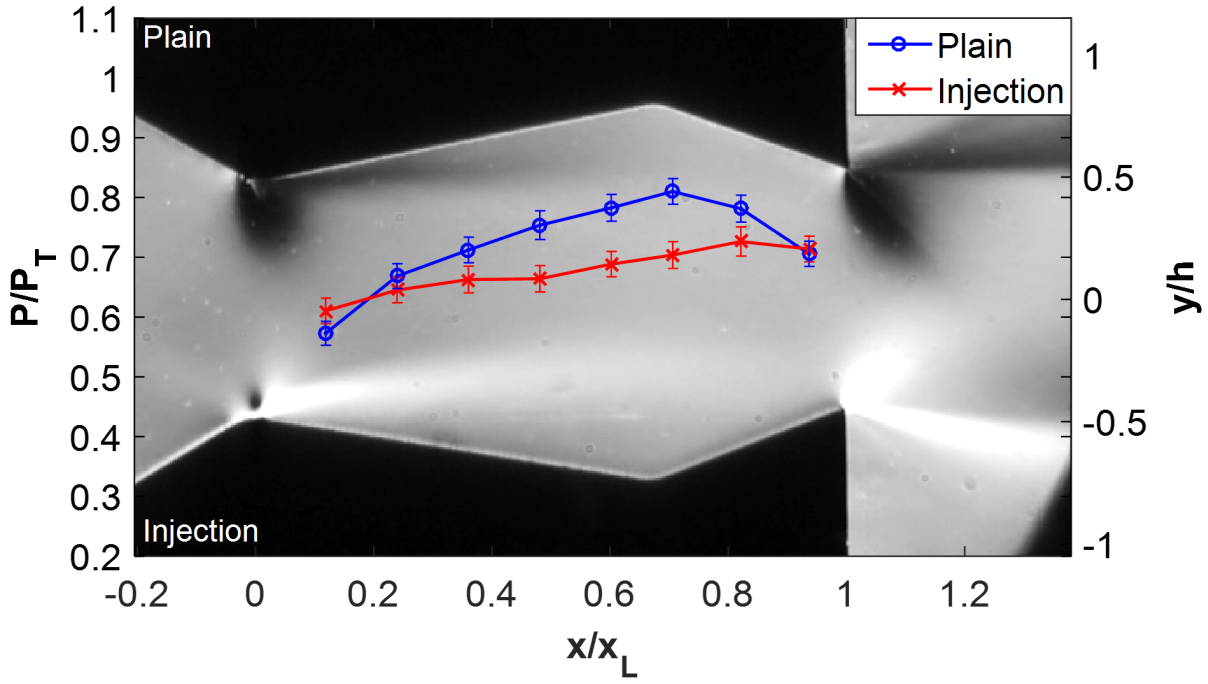

(b) Case 3.D.4

Figure 3.68: Cases 3.C.4 and 3.D.4

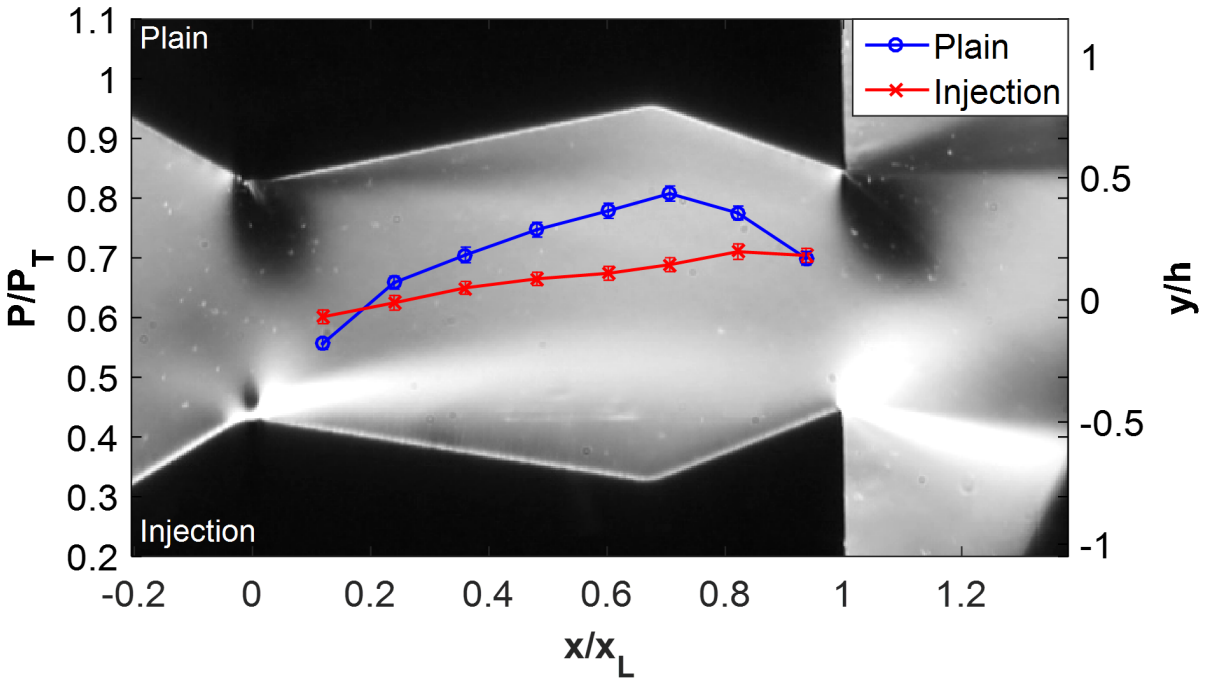

(a) Case 3.E.4

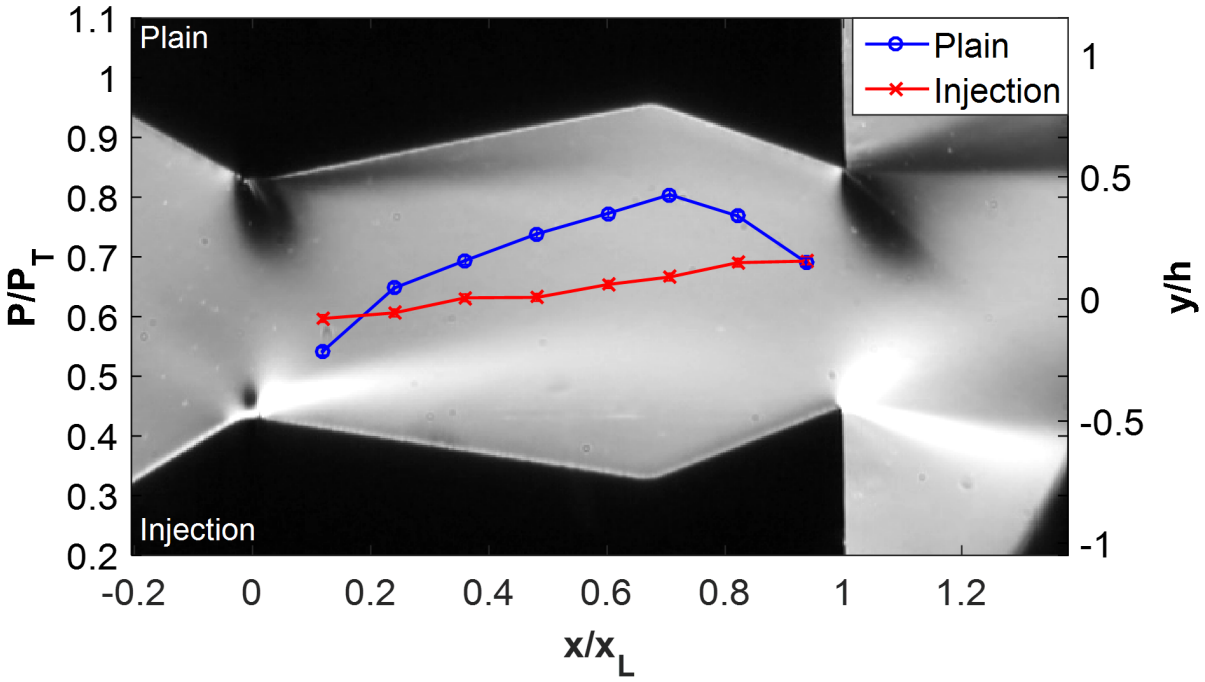

(b) Case 3.F.4

Figure 3.69: Cases 3.E.2 and 3.F.2

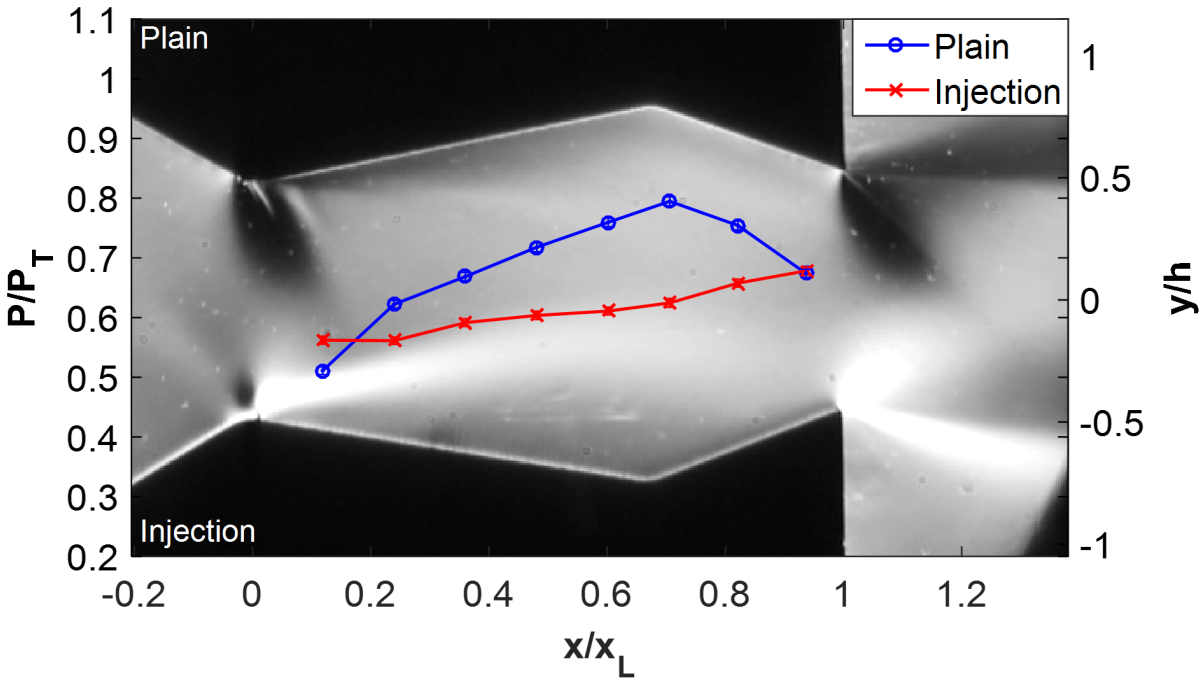

Figure 3.70: Case 3.I.4

It can be seen that flow characteristics of the 3.*.4 case match 1.*.4 and 2.*.4 much more closely than the 3.*.2 cases compared against 1.*.2 and 2.*.2. This is due to the decreased effect the injection holes have at a NPR of 4. This identifies viscous effects as likely being the reason for the behavior seen in 3.*.2. Overall, pressure profile trends are seen to be similar to the other two cases with a very predictable decreasing progression of the wall pressure with increasing injection percentage. Figures 3.71 (a) and (b) show the progression of wall pressure profiles.

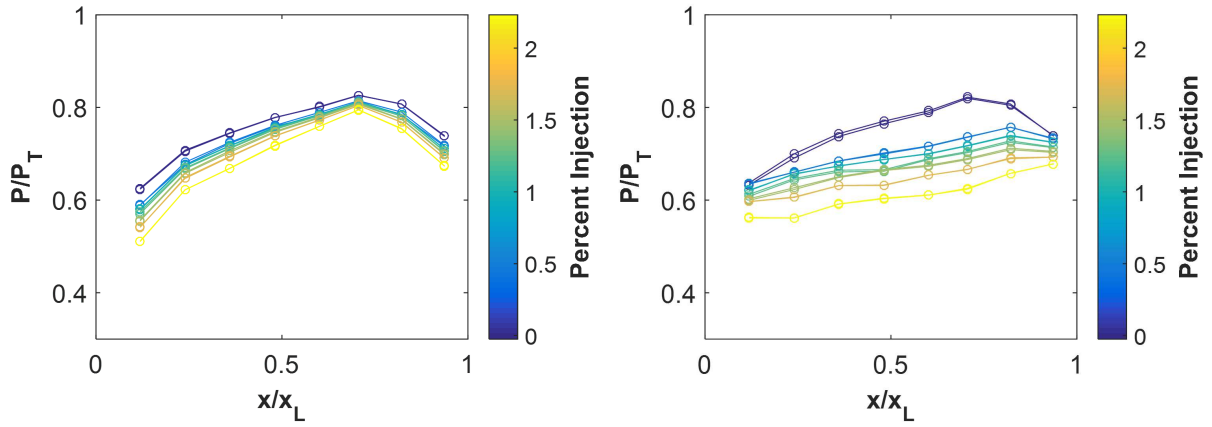

(a) Upper Wall Pressure Profile Progression

(b) Lower Wall Pressure Profile Progression

Figure 3.71: Case 3.*.4 wall pressure profile progression as a function of injection percentage.

3.5 Vector Angle Performance

The most important performance indicator for the test cases was the thrust-vector angle induced by secondary injection. Thrust-vector angle was determined using the schlieren images for each test and averaged for the tests conducted at the same conditions. Figure 3.72 shows the thrust-vector angle for each case at a NPR of 2.

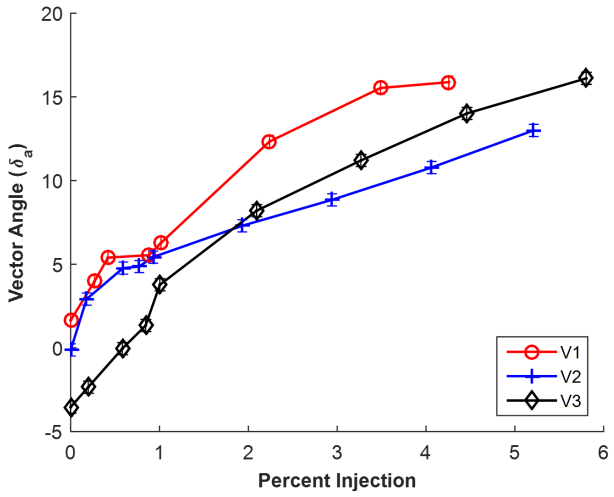

Figure 3.72: Vector performance for each case at NPR = 2.

For each test case, there is a clear trend showing increased thrust-vector angle with an increase in percent injection. However, the rate and initial condition for each case varies significantly. The V1 test geometry was found to generate similar thrust-vector angles as V2 from 0% to approximately 1% secondary injection. However, after 1%, the performance of V1 increases drastically above both of the other injection geometries. Test geometry V3 was unique in that the holes injection geometry seemed to induce reattachment of the flow along the lower injection wall at small injection percentages. This effect can be seen with the negative thrust-vector angle from zero to about 0.75% secondary injection. However, after sufficient secondary injection in achieved, the thrust-vector angle eventually surpasses the angle generated by case V2. Indicated by the difference in vector angle between cases V1 and V2, the injection slot thickness is seen to have a significant inverse relationship with thrust-vector performance where a decrease in thickness results in an increase in performance. Additionally, case V3 performed better than case V2 above injection percentages of two percent, but performed worse consistently compared to case V1. Vector efficiency, which is the angle per percent injection, was another parameter investigated. This relationship is shown in Figure 3.73.

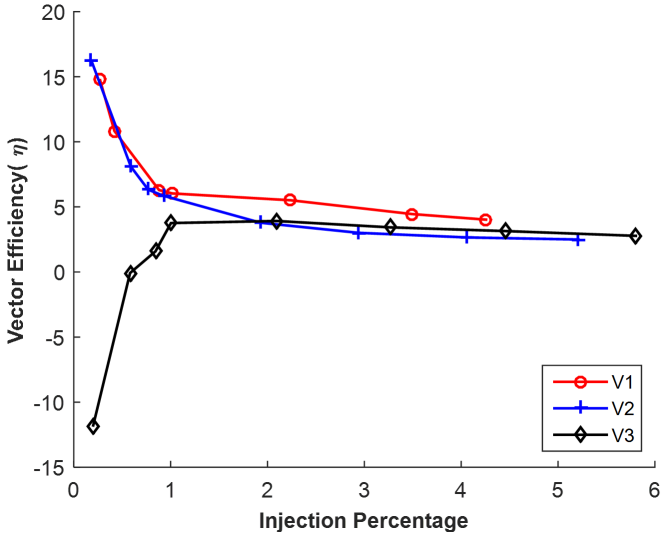

Figure 3.73: Vector efficiency for each case at NPR = 2.

What was most notable is that at injection percentages less than one percent, the magnitude of vector efficiency is extremely high. However, as injection percentage is further increased, there is a diminishing increase in additional vector angle. Additionally, for cases like V3 in which the vector angle is initially negative, there is a significant injection requirement before the efficiency becomes positive.

At a NPR of 4, similar results were found. Figure 3.74 shows the vector angle for each case as a function of injection percentage.

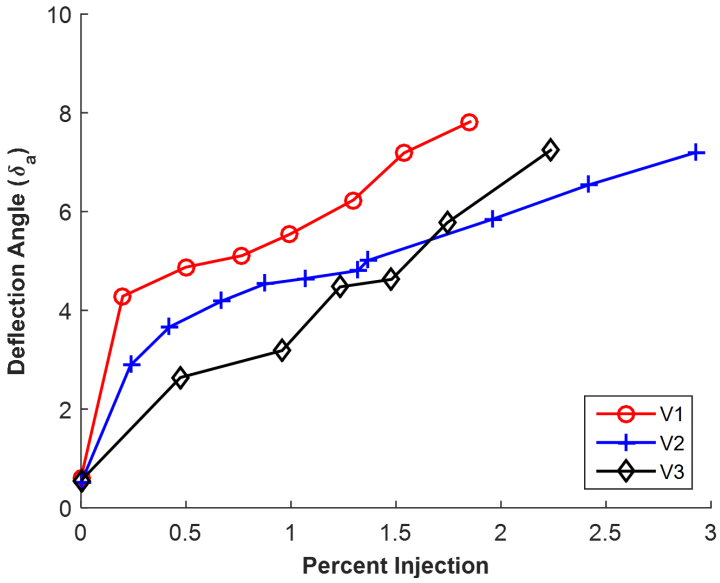

Figure 3.74: Vector performance for each case at NPR = 4.

Compared to the NPR of 2 cases, the comparable performance of each nozzle case is similar with V1 outperforming each other case and V3 surpassing V2 at injection percentages above 1.75%. However, unlike the NPR of 2 cases, there is no bias for any of the cases at 0% injection. This results in positive thrust-vector efficiency for all cases over the entire range of injection percentages. The thrust-vector efficiency can be seen in Figure 3.75.

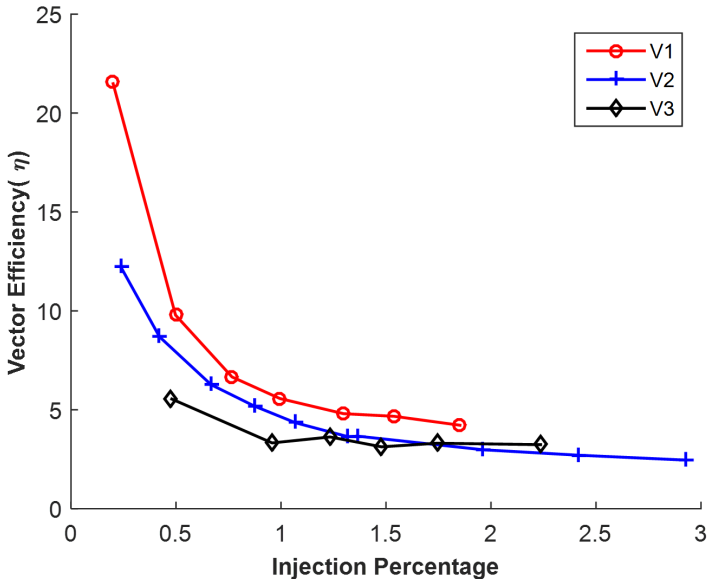

Figure 3.75: Vector efficiency for each case at NPR = 4.

3.6 Thrust-Vector Angle Prediction

Collection and analysis of the pressure profile data showed a clear trend between wall pressure profile and injection percentage. Once this trend was noted, a method was investigated for predicting thrust-vector angle based on the lower and upper wall pressure profile. The method employed used a force balance by integrating the wall pressure profiles to determine the net force in the y direction. The net total force was then calculated using the standard thrust equation. By calculating the angle between the net total force and the y component of the force, an estimate of the thrust-vector angle was derived. The process is described by Equations 2.11 through 2.13. Using the pressure profiles for each case 1.*.2, Figure 3.76 shows the thrust-vector angle measured from the schlieren photographs compared to that calculated using the pressure profile.

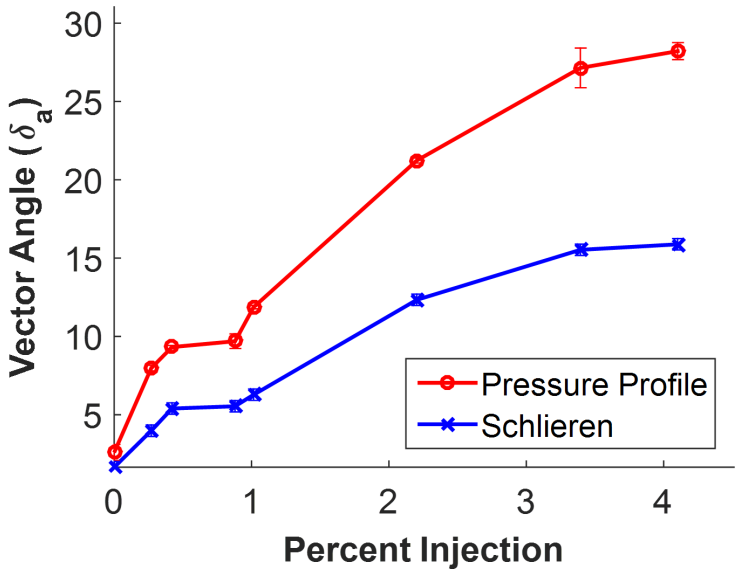

Figure 3.76: Vector angle prediction for Case 1.*.2.

It is clear that there is very poor agreement between the angles derived from the two different methods. However, the trends are very similar which suggested that the methodology was correct. What was discovered was that while the locations of the pressure taps sampled a majority of the nozzle well, the large pressure gradients at both throats were not being accurately captured. This is shown in Figure 3.77 which shows a comparison between sampled and unsampled CFD profiles at the experimental pressure tap locations.

Only using the pressure sampled at the pressure tap locations and integrating using a trapezoidal method meant that the net force in the y direction was being overestimated, hence the higher predicted angle. To compensate for this missing information, the ratio between the net y force calculated using the pressure sampled at the pressure taps and the net y force calculated using the entire pressure profile was compared for both nozzle injection geometries and at varying injection percentages from the CFD data. The result was a very consistent ratio regardless of secondary injection geometry and secondary injection percentage. Figure 3.78 shows the relationship for both V1 and V2 CFD cases.

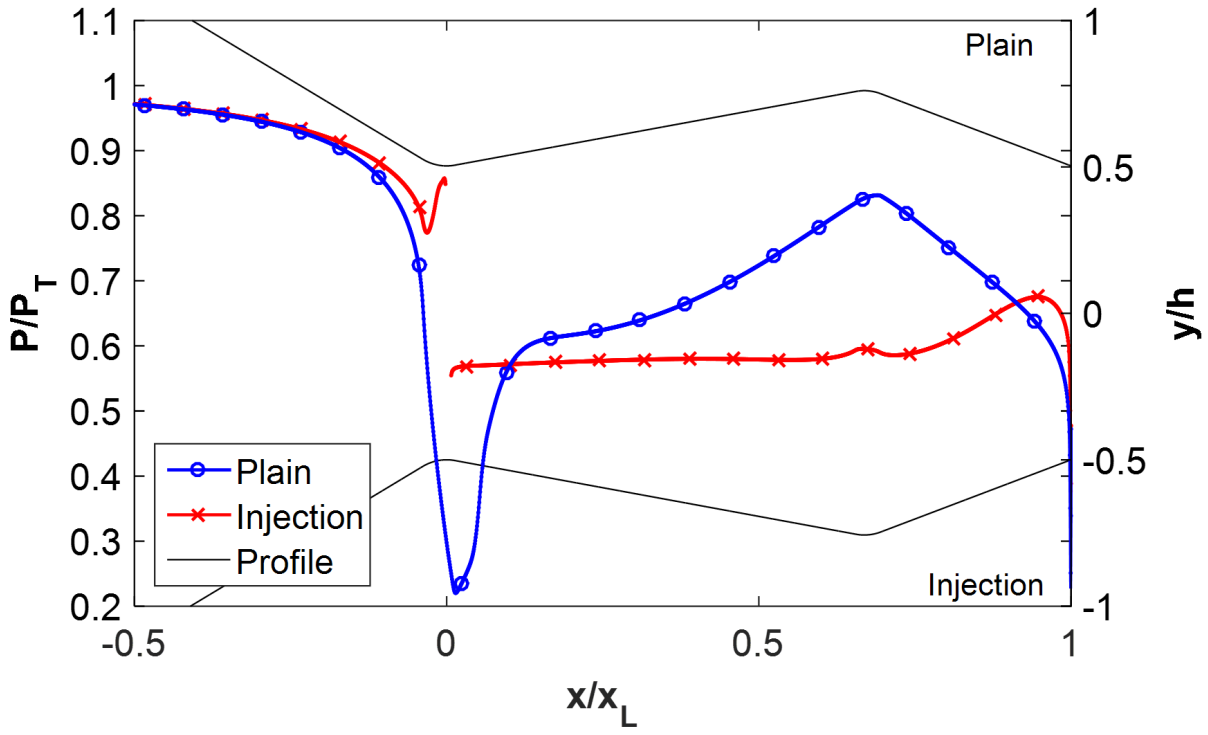

(a) Full CFD Wall Pressure Profile

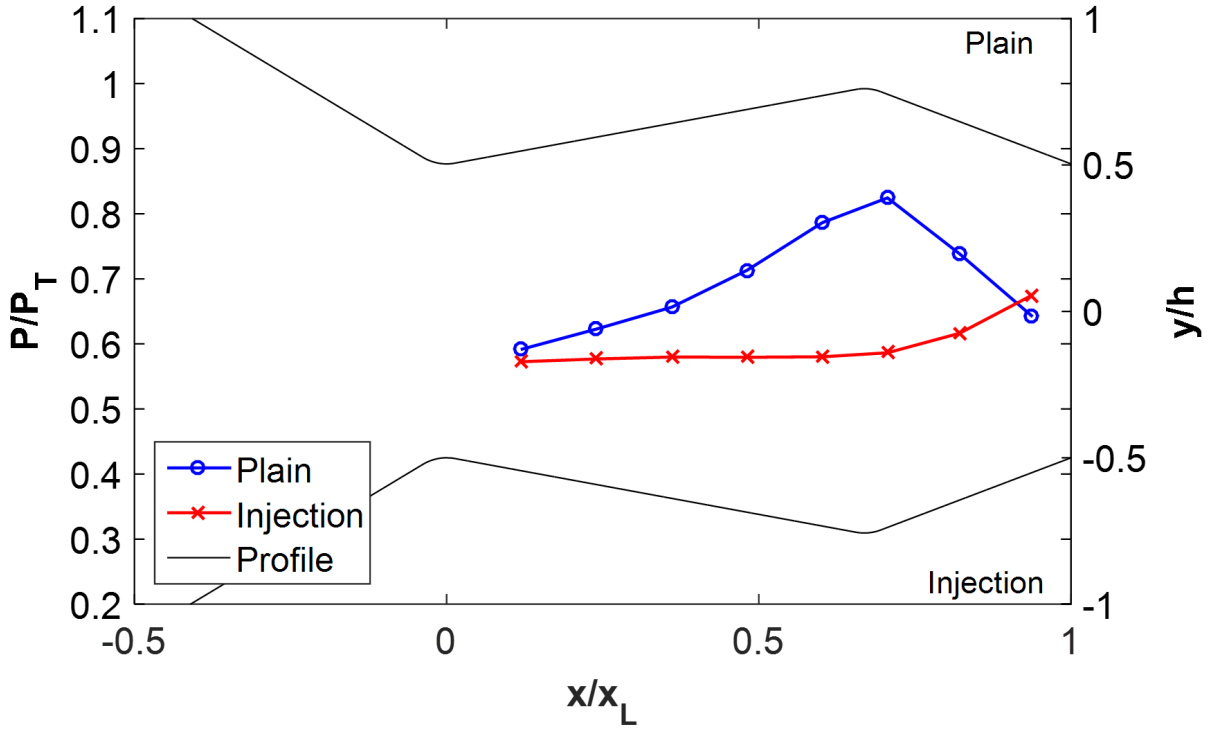

(b) Sampled CFD Wall Pressure Profile

Figure 3.77: Full versus sampled CFD wall pressure profile.

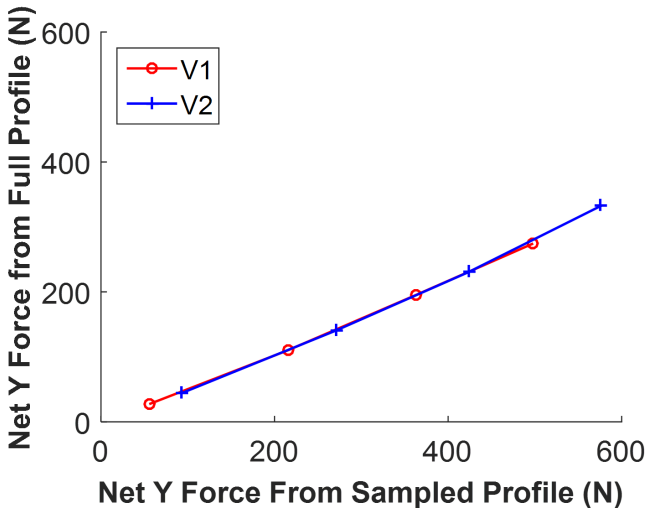

Figure 3.78: Relationship between force from full and sampled pressure profile for NPR = 2.

Using an average slope for both of these cases of 0.58, the net y force derived from the experimental results was corrected by this factor to account for the pressure gradients not measured around the upstream and downstream throats. With this factor applied, the agreement between the schlieren thrust-vector angle and the pressure profile derived thrust-vector angle improved drastically. Figure 3.79 shows the corrected data for case 1.*.2. This same factor was applied to the 2.*.2 and 3.*.2 data as well with similar results shown in Figure 3.80.

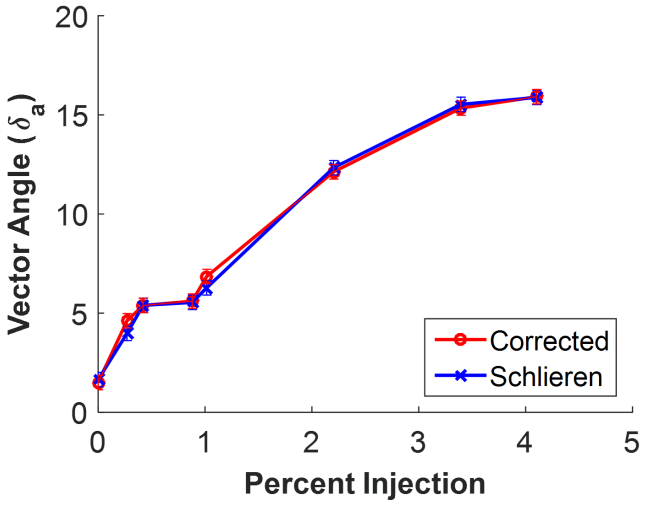

Figure 3.79: Case 1.*.2 predicted and schlieren vector angle.

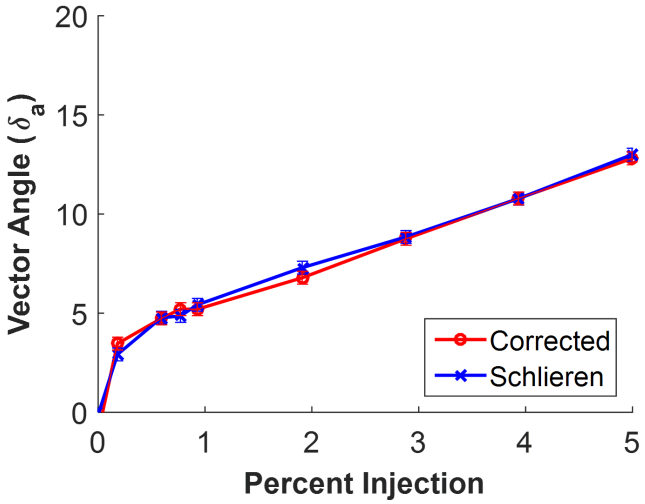

(a) Case 2.*.2

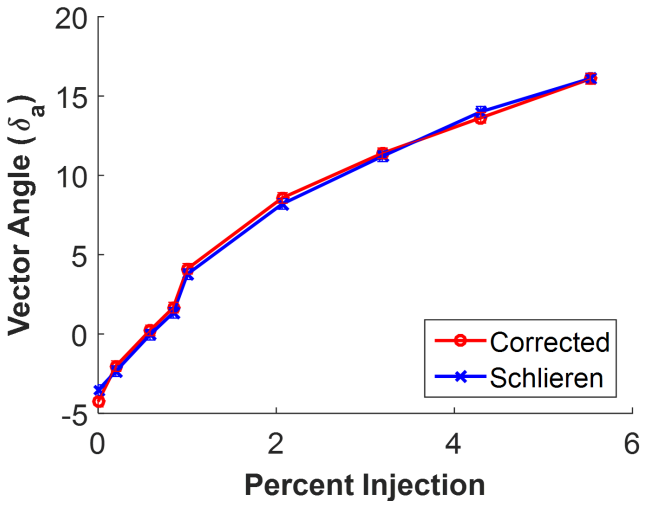

(b) Case 3.*.2

Figure 3.80: Cases 2.*.2 and 3.*.2 predicted and schlieren vector angle.

The agreement for all three cases at a NPR of 2 were found to be within the measurement error for almost all injection percentages. This same method was employed on the data gathered at a NPR of 4. Since enough CFD data was not generated at a NPR of 4, the ratio employed for the NPR of 2 case was used. This gave similar results but, with slightly worse agreement. Figure 3.81 through 3.83 show the thrust-vector angle from schlieren and predicted from the wall pressure profiles for the NPR of 4 case.

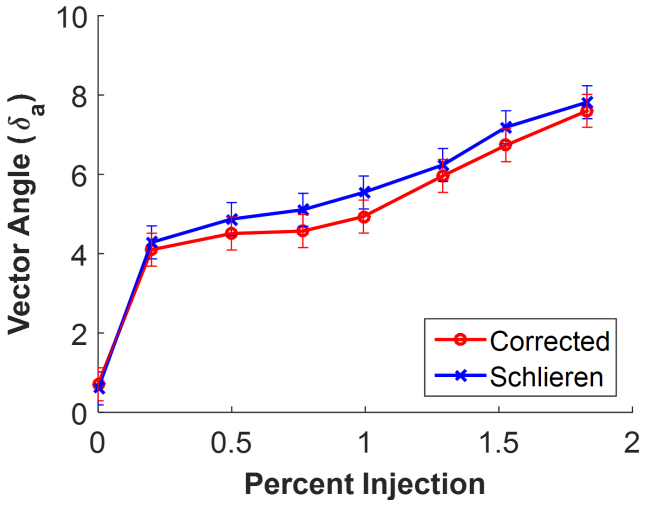

Figure 3.81: Case 1.*.4 predicted and schlieren vector angle.

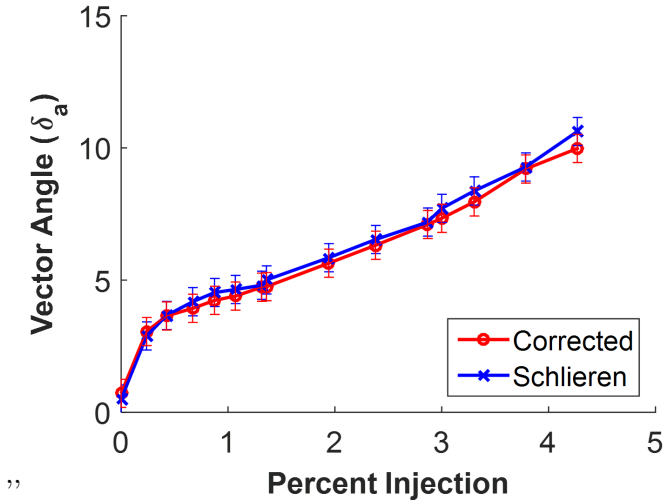

,,

Figure 3.82: Case 2.*.4 predicted and schlieren vector angle.

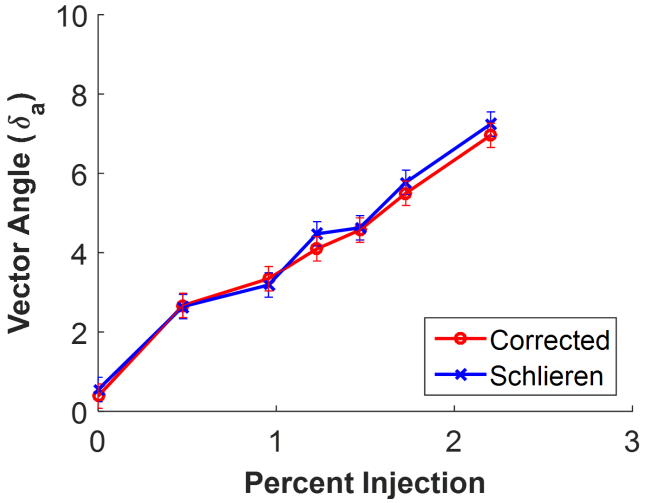

Figure 3.83: Case 3.*.4 predicted and schlieren vector angle.

Even using the CFD generated from a NPR of 2, the agreement between the thrust-vector angle determined from the schlieren and that predicted from the pressure profiles is very good for all NPR of 4 cases. However, even better agreement would be expected if CFD data at the correct conditions was used to develop the correction factor.

3.6.0.1 Comparison of Results

Injection geometries in this study were chosen largely based on the geometries used by Flamm et al.[10] and a comparison between the published vector performance and the results from this study show similar trends. In the results from Flamm et al.[10] shown in Figure 3.84, the vector performance of the slot type injection geometry is seen to outperform the vector performance of both hole injection types up to about 4% injection.

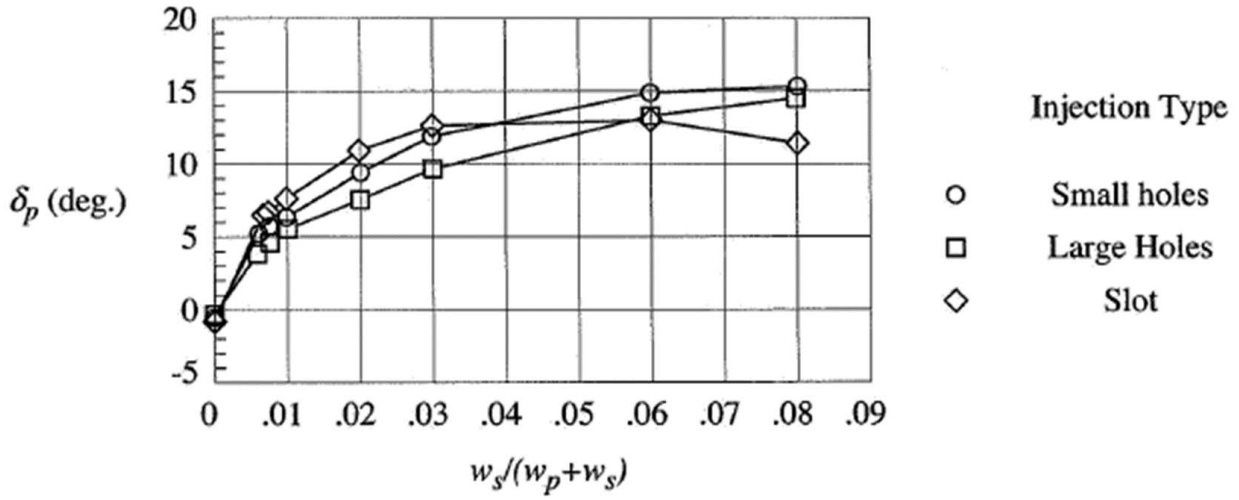

Figure 3.84: Thrust-vectoring angle as a function of injection percentage $\frac{w_s}{w_p+w_s}$, and the injection shape [10]

This is similar to the results seen in Figure 3.85 from the current study which show improved performance of the slot injection type over the hole injection over the entire range of injection percentages investigated.

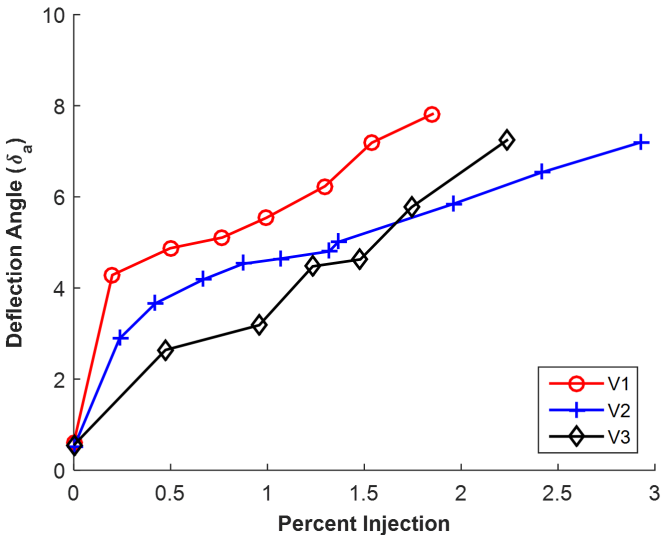

Figure 3.85: Vector performance for each case at NPR = 4.

However, similar to the results in Flamm et al.[10], the vector performance for the hole injection type (V3) trends higher compared to the slot injection surpassing the larger slot (V2), but not the smaller slot (V1). Increasing the injection percentage further would be expected to result in the hole injection (V3) vector angle surpassing the smaller slot (V1) vector angle.

Chapter 4

Conclusion

A dual-throat fluidic thrust-vectoring nozzle was investigated in order to better characterize its thrust-vector performance over a range of flow conditions and secondary injection geometries. The nozzle was modeled based on a similar nozzle developed and tested at NASA Langley by Flamm et al.[10] in order to contribute to existing data sets. A facility purpose-built for this study was used for experimental testing of the nozzle designs from which pressure profiles and schlieren images were obtained. A less extensive computational study was also conducted in order to better understand the flow field in locations where experimental data could not be gathered. In total, three different nozzle geometries were investigated while only varying the secondary injection geometry. The three secondary injection geometries explored were two cases (V1, V2) with spanwise oriented rectangular slots of different thicknesses as well as a spanwise array of of nine individual holes (V3). The comparison between hole and slot secondary injection geometry had been performed in the previous work by Flamm et al.[10], but varying secondary injection slot thickness had not been done, to date. Initial baseline testing at a NPR of 2 for each injection type showed a significant impact on primary flow thrust-vector angle even without injection. The thinnest secondary injection slot, configuration V1, induced a thrust-vector angle of about 2° due to separation induced by the injection geometry. The larger slot geometry V2 showed less separation while V3, which employed the series of injection holes, generated a -4° thrust-vector angle with no secondary mass injection. This negative vector angle was attributed to three-dimensional flow patterns that are expected to exist between the holes. Increasing NPR to 4, however, largely removed this bias with all three

configurations generating an initial thrust-vector angle of about 0.5° in this zero-injection state.

With the introduction of secondary injection, vector efficiency was found to be the highest between 0 and 1%. Geometry V3 was unique in that at a NPR of 2 it generated negative vector angles until about 0.75% injection. Overall, geometry V1 generated the largest vector angles over the full range of secondary injection percentages and NPRs evaluated. When NPR was increased to 4, the vector angles for a given injection percentage decreased, but the same trends between geometries remained.

Data gathered from the computational and experimental results were also used to develop a method to predict the flow thrust-vector angle within measurement error. The angle was predicted using the pressure profiles on the upper and lower nozzle walls, an estimate for the total thrust generated, and a correction factor derived from the CFD. The correction factor was calculated by comparing the integration of the complete CFD nozzle wall pressure profile to a CFD nozzle wall pressure profile sampled at the experimental pressure tap locations. A relationship between these two integrated values was found to be constant for the entire range of secondary injection percentages and secondary injection geometries evaluated. The resulting prediction of the thrust-vector angle matched the angle measured in the schlieren photographs within experimental measurement accuracy.

4.1 Future Work

The experimental and computational results obtained from this study cover only a small section of the total parameter space of the dual throat fluidic thrust vectoring nozzle. This leaves a large range of potential future works to examine the effects of these additional parameters.

All of the currently published studies conducted on the dual throat nozzle have used a configuration in which injection is only supplied on one side of the upstream throat. However, there is a significant potential for using this configuration to throttle the size of the aerodynamic throat by injecting a secondary flow on opposing sides of the nozzle. This throttling would allow the system to be better optimized based on engine and atmospheric conditions. However, since core

flow would no longer be contacting the upstream throat, the separation characteristics that were seen to have a significant impact on thrust-vector efficiency would be significantly different. Using similar computational resources as well as minor modifications to the current infrastructure could allow for an investigation into this concept.

Another unique concept that should be explored is the combined use of secondary and tertiary injection as opposed to a single point of secondary injection. Studies such as Domel et al. [16] have shown an improvement in flow penetration when a secondary and tertiary injection of the same total mass flow rate is used instead of a single secondary injection. By splitting the secondary flow into these secondary and tertiary streams, an increase in vector performance could be realizable. Minor modifications to the existing hardware would be required to explore this concept.

A final improvement that would provide additional insight into the experimental flow characteristics is the addition of a particle image velocimetry (PIV) system. Schlieren photography provides some insight into the flow structure within the nozzle, but is not able to accurately visualize separation or circulation. The addition of a PIV system would allow for these more complex flow structures to be identified and quantified. This would require modification of the current test system to include flow seeding within the high pressure flow as well as a clear path for illumination of the flowfield through a planar laser sheet orthogonal to the camera viewing position.

Bibliography

[1] Thomson, R. J. and Phen, R. L., "Study of Selected Thrust Vector Control Systems for Solid Propellant Motors," Tech. rep., 1965.

[2] Deere, K. A., "Summary of Fluidic Thrust Vectoring Research Conducted at NASA Langley Research Center," 2003, pp. 1–18.

[3] Collins, E. G., Zhao, Y., Alvi, F., Alidu, M. I., and Strykowski, P. J., "Feedback control for counterflow thrust vectoring," Proceedings of the American Control Conference, Vol. 4, 2004, pp. 3654–3659.

[4] Flamm, J. D., "Experimental Study of a Nozzle Using Fluidic Counterflow for Thrust Vectoring," Control, 1998.

[5] Schmid, G. F., Strykowski, P. J., Madruga, M., Das, D., and Krothapalli, A., "Jet Attachment Behavior using Counterflow Thrust Vectoring," 2000, pp. 10–12.

[6] Dores, D. and Madruga, S. M., "Characterization of a Counterflow Thrust Vectoring Scheme on a Gas Turbine Engine Exhaust Jet," , No. June, 2006, pp. 1–12.

[7] Wing, D. J., "Static Investigation of Two Fluidic Thrust-Vectoring Concepts on a Two-Dimensionl Convergent-Divergent Nozzle," Tech. Rep. December 1994, 1994.

[8] Deere, K. a., Berrier, B. L., and Flamm, J. D., "A Computational Study of a New Dual Throat Fluidic Thrust Vectoring Nozzle Concept," , No. July, 2005, pp. 1–16.

[9] Flamm, J., Deere, K., Berrier, B., Johnson, S., and Mason, M., "Experimental Study of a Dual-Throat Fluidic Thrust Vectoring Nozzle Concept," 41 st AIAA/ASME/SAE/ASEE Joint Propulsion Conference & Exhibit, No. July, 2005, pp. 1–19.

[10] Flamm, J. D., Deeret, K. A., Mason, M. L., Berrier, B. L., and Johnson, S. K., "Design Enhancements of the Two-Dimensional , Dual Throat Fluidic Thrust Vectoring Nozzle Concept," 3rd AIAA Flow Control Conference, No. June, 2006, pp. 1–27.

[11] Flamm, J., Deere, K., Mason, M., Berrier, B., and Johnson, S., "Experimental Study of an Axisymmetric Dual Throat Fluidic Thrust Vectoring Nozzle for Supersonic Aircraft Application," 43rd AIAA/ASME/SAE/ASEE Joint Propulsion Conference & Exhibit, 2007, pp. 1–28.

[12] Bellandi, E. G. and Slippey, A. J., "Preliminary Analysis and Design Enhancements of a Dual-Throat FTV Nozzle Concept," Fluid Dynamics, , No. June, 2009, pp. 1–12.

[13] Gu, R. and Xu, J., "Effects of Cavity on the Performance of Dual Throat Nozzle During the Thrust-Vectoring Starting Transient Process," Journal of Engineering for Gas Turbines and Power, Vol. 136, No. 1, 2013, pp. 014502.

[14] Pope, A. and Goin, K. L., High-speed Wind Tunnel Testing, New York: Wiley, 1965.

[15] Rennels, D. C. and Hudson, H. M., Pipe Flow: A Practical and Comprehensive Guide, 2012.

[16] Neal D. Domel, Baruzzini, D., and Miller, D. N., "Pulsed Injection Flow Control for Throttling in Supersonic Nozzles-A Computational Fluid Dynamics Design Study," Fluid Dynamics, Vol. 16, No. 0704, 2007.

[17] Bharath, B. K., "Design and Fabrication of a Supersonic Wind Tunnel," International Journal of Engineering and Applied Sciences, Vol. 2, No. 5, 2015, pp. 103–107.

[18] Deere, K. A., "Computational Investigation of the Aerodynamic Effects on Fluidic Thrust Vectoring," 36th AIAA/ASME/SAE/ASEE Joint Propulsion Conference & Exhibit, Vol. 2000, No. 3598, 2000.

[19] Deere, K. A., Berrier, B. L., Flamm, J. D., and Johnson, S. K., "Computational Study of Fluidic Thrust Vectoring using Shock Vector and Separation Control," .

[20] Deeret, K. A., Flamm, J. D., Berrier, B. L., and Johnson, S. K., "Computational Study of an Axisymmetric Dual Throat Fluidic Thrust Vectoring Nozzle for a Supersonic Aircraft Application," .

[21] Gu, D.-W., Natesan, K., and Postlethwaite, I., "Modelling and robust control of fluidic thrust vectoring and circulation control for unmanned air vehicles." IMechE - Systems and Control Engineering, Vol. 222, 2009, pp. 333–345.

[22] Heo, J.-Y., Yoo, K.-H., Lee, Y., Sung, H.-G., Cho, S.-H., and Jeon, Y.-J., "Fluidic Thrust Vector Control of Supersonic Jet Using Co-flow Injection," 45th AIAA/ASME/SAE/ASEE Joint Propulsion Conference & Exhibit, No. August, 2009, pp. 1–12.

[23] Mason, M. and Crowther, W., "Fluidic Thrust Vectoring of Low Observalbe Aircraft," CEAS Aerospace Aerodynamic Research ..., , No. June, 2002, pp. 10–12.

[24] Saito, T. and Fujimoto, T., "Numerical Studies of Shock Vector Control for Deflecting Nozzle Exhaust Flows," .

[25] Santos, M., Experimental Study on Counter Flow Thrust Vectoring of a Gas Turbine Engine, Ph.D. thesis, 2005.

[26] Settles, G., Schlieren and Shadowgraph Techniques, 2001.

[27] Shin, C. S., Kim, H. D., Setoguchi, T., and Matsuo, S., "A Computational Study of Thrust Vectoring Control Using Dual Throat Nozzle," Journal of Thermal Science, Vol. 19, No. 6, 2010, pp. 486–490.

[28] Zou, X. H. and Wang, Q., "The Comparative Analysis of Two Typical Fluidic Thrust Vectoring Exhaust Nozzles on Aerodynamic Characteristics," 2011, pp. 610–617.

Appendix A

View of Experimental Setup

Figure A.1: View of test setup including diffuser, test section, and schlieren system.